On the instability of water waves with surface tension.

Olga Trichtchenko

A dissertation
submitted in partial fulfillment of the
requirements for the degree of

Doctor of Philosophy

University of Washington

2014

Reading Committee:

Bernard Deconinck, Chair

Randy LeVeque

Robert O'Malley

Program Authorized to Offer Degree:
Applied Mathematics

University of Washington

Abstract

On the instability of water waves with surface tension.

Olga Trichtchenko

Chair of the Supervisory Committee:
Professor Bernard Deconinck
Department of Applied Mathematics

We analyze the stability of solutions to Euler's equations in the presence of surface tension. First we compute stationary solutions to periodic Euler's equations in a travelling frame of reference and then we analyze their spectral stability. Depending on the coefficient of surface tension, we see resonant effects in the solutions. This results in a myriad of instabilities for gravity-capillary waves. Since the theory for analyzing the stability of water waves is general to all Hamiltonian systems, we extend the results to other equations, mainly ones that are used to model water waves in different asymptotic regimes. We compare the stability results for the model equations to those we obtain for the full water wave system and comment on the applicability of these models.

TABLE OF CONTENTS

LIST OF FIGURES

LIST OF TABLES

ACKNOWLEDGMENTS

There are too many people to acknowledge, where do I start? First of all, I would like to acknowledge my thesis committee for their help in making this possible, my collaborator Jon Wilkening for providing his code and the soon to be collaborator Ben Akers, for letting the right people know I am looking for postdocs.

The people who have had the most direct contribution to this work have been the ones in my research group (past and current members). If it was not for my advisor Bernard Deconinck, our group would not be all that we are. Not only did he teach me some of the most relevant and interesting classes as a professor and cared about my well being in graduate school in his graduate program coordinator position, but he also contributed guidance and collaboration as a researcher. He has given me countless late nights (mostly due to my own last minute nature), many hours of emotional support, an even larger number of desserts and hikes. I am very grateful to the unique experience I had being part of this research group. It has been amazing to have Katie Oliveras as my informal mentor, talking about her experiences in graduate school and as a young researcher, as well as giving me the secrets behind all her code and always being available to help. There was also a lot of guidance from the older academic brothers Vishal Vasan and Tom Trogdon. Natalie Sheils has been an amazing academic sister and officemate. She is one of the most reliable and easy-going people who is always willing to help and always ready to take on anything presented in front of her. I don't know that I will ever have such a great office situation as I have had here in Lewis. I would like to acknowledge Chris Swierczewski for being there since day 1 with TAing in math and those early linear analysis mornings, they will not be missed. I would also like to thank my younger academic brothers Ben Segal, co-TA and stability in fluids classmate as well as Jeremy Upsal for being good work support during this last month of thesis writing. Outside of this immediate group, between academic uncles like

John Carter and academic grandfathers, aunts and other extended family, this has been a really great area to work in with very supportive and incredibly brilliant people.

I'd also like to mention my classmates Alex Cayco Gajic, Mikala Johnson, Pedro Maia and Susan Massey who have been there since my first year at University of Washington without whom those homeworks would not have been done and who have been there to commiserate at every step of the way. Alex and Susan in particular, you know what you did. I'd also like to mention Kit Curtius, Ben Lansdell, Mauricio Del Razo and Daniel Shapero. I'm glad you were all around to make grad school more interesting.

Now, for those people from my McGill days. I would like to acknowledge Nilima Nigam for introducing me to applied mathematics when all this began. My older brothers David Cottrell and Marc Ryser, you made the applied math doctorate degree look cool. Charles-Francois de Lannoy, Patrick Lazarus and Bobak Shahriari for the laughs dating back to our undergrad physics days. I'd also like to acknowledge Naomi Klinghoffer and Brian Hamilton. Even though we are in such different places and fields, our experiences are so similar and I'm glad you are out there to share them with me.

I would also like to thank my Seattle family. Petey and Jeanne. It has been a pleasure living with you all these years. You have made it easy, comfortable and fun. Nick Cain (and Claire), I am also grateful for you letting me move into that house on cap hill. Dominique Perrault-Joncas and Nevena Lalic (Leonie and Otto), I am glad I knew you well enough to marry you.

There are many others I did not name specifically. All the students and professors at University of Washington and those friends in Seattle, thank you for being there. I am very lucky to have spent so many great years in your company. And what is a thesis acknowledgement without a thank you to my lifelong best friend Ivana Arambasic. I'm so glad I can always count on you.

DEDICATION

To Dr. Mom and Dr. Dad

Chapter 1

INTRODUCTION

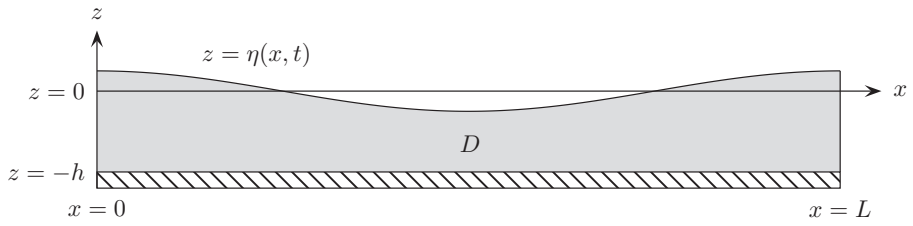

Figure 1.1: The domain on which we solve Euler's equations.

The goal of this thesis work is to investigate what effect the addition of surface tension has on modelling water waves. The classical water wave problem is the problem of determining the shape and dynamics of the free surface on an incompressible, inviscid fluid. Since the fluid is irrotational, a velocity potential is introduced. For one dimensional surface waves, the problem is described by the classical equations [86]

$$\begin{cases} \phi_{xx} + \phi_{zz} = 0, & (x,z) \in D, \\ \phi_z = 0, & z = -h,\ x \in (0,L), \\ \eta_t + \eta_x \phi_x = \phi_z, & z = \eta(x,t),\ x \in (0,L), \\ \phi_t + \frac{1}{2}\left(\phi_x^2 + \phi_y^2\right) + g\eta = \sigma \dfrac{\eta_{xx}}{(1+\eta_x^2)^{3/2}}, & z = \eta(x,t),\ x \in (0,L), \end{cases} \tag{1.1}$$

where h is the height of the fluid, g is the acceleration due to gravity and σ is the coefficient of surface tension. Further, $\eta(x,t)$ is the elevation of the fluid surface, and $\phi(x,z,t)$ is its velocity potential. In this paper, we focus on solutions on a periodic domain $D = \{(x,z) \mid 0 \leq x < L, -h < z < \eta(x,t)\}$, see Fig. 1.1. By varying the depth of the water, the coefficient of surface tension can take any positive value [1] and therefore all such values should be considered.

An important property of these equations, is the existence of a singular limit otherwise known as the resonance condition. It can be understood by considering a Stokes expansion [82] for the surface of the wave. Using regular perturbation theory, we expand the surface

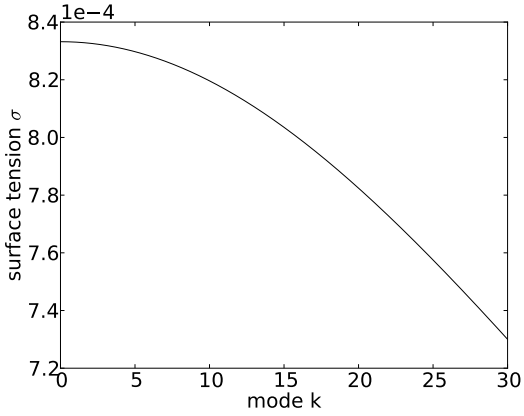

Figure 1.2: Plot of (3.14) that shows the relationship between surface tension σ and resonant modes k.

in terms of a small parameter ϵ representing the amplitude of the wave

$$\eta(x) = \sum_{n=1}^{\infty} \epsilon^n \eta_n. \tag{1.2}$$

From the work by Stokes [82] and convergence results by Levi-Civita [57] and Struik [83], we know we can also expand the wave profile in terms of a cosine series

$$\eta_n(x) = \sum_{m=1}^{n} \hat{\eta}_{nm} \cos(mx). \tag{1.3}$$

From this, we obtain a solvability condition for η_n with $m \in \mathbb{Z}$. If

$$(g+\sigma)\tanh(h) - \left(g + m^2\sigma\right)\frac{\tanh(mh)}{m} = 0 \tag{1.4}$$

does not hold, then we can solve for η_m. We call (1.4) the resonance condition. The coefficient of surface tension σ determines the resonant harmonic $m \in \mathbb{Z}$ and was first noticed by Wilton [92]. Numerically, it is interesting to vary σ depending on which resonant mode we wish to capture. The relation between surface tension and resonant modes is shown in Figure 1.2. In this thesis, we examine what happens in the cases where we are near-resonance $m \neq \mathbb{Z}$ and in those where we are at resonance. However, this resonance condition is a weakly nonlinear theory result. This implies it is valid for small amplitude

solutions. In our work, we are interested in solutions of the fully nonlinear problem and thus, arbitrary amplitude waves.

The work presented here follows that of Oliveras in her thesis [72] as well as Deconinck and Oliveras [25]. They presented a thorough numerical overview of the spectral instabilities of periodic traveling one-dimensional gravity (*i.e.*, $\sigma = 0$) water waves. An emphasis of that work is the presence of oscillatory instabilities even for waves in shallow water ($kh < 1.363$, see [6, 87], here $k = 2\pi/L$). Since the underlying waves are periodic, their stability analysis uses Hill's method, see [23], which incorporates the conclusions from Floquet's Theorem with Fourier analysis. This associates with each wave a range of Floquet exponents μ which may be taken as $(-\pi/L, \pi/L]$. In this thesis, we extend the analysis to water waves in the presence of surface tension. Mainly, we explore how the oscillatory instabilities change when the capillarity effect is included, paying careful attention to the resonance phenomena of Wilton ripples.

The thesis is laid out in the following way. In Chapter 1, we provide an overview of the literature on this classical problem. Since the field is over 300 years old, we focus mainly on literature relevant to the work presented here. That is, we present results about periodic travelling wave solutions of Euler's equations as well as their stability. The next chapter discusses results in [26]. These are the stability results for gravity waves in the presence of surface tension. Chapter 3 describes what happens to stability as we increase the strength of surface tension, leading to analysis of gravity-capillary waves. Chapter 4 then discusses the resonant solutions in the presence of Wilton ripples. In Chapter 5, we extend the general theory of stability for solutions of small amplitude, to include other examples. We finish the thesis by summarizing and concluding the results shown in this work.

Chapter 2

BACKGROUND AND LITERATURE REVIEW

2.1 Introduction

The study of water waves goes back as far as Newton (1687), Euler (1761) and Bernouilli (1738) [18], more than 300 years ago. The field benefits from theoretical contributions in addition to experimental ones. This chapter attempts to cover the literature that is most relevant to the current work. It is by no means comprehensive. In this work, we are interested in solving the set of Euler's equations describing an inviscid, irrotational fluid on a periodic domain. This is done in two steps. First, solutions are constructed and second, their stability is investigated. The main emphasis of the thesis is on the analysis of solutions involving the effects of surface tension. Traditionally, it has been thought that the effects of surface tension are stabilizing [56]. Mathematically, the addition of surface tension as a nonlinear effect in the set of governing equations, requires more careful consideration.

Instead of solving the full system, asymptotic analysis can be used to simplify the problem. Many approximations to Euler's equations are relevant in different regimes. For shallow water waves for instance, there are the one-dimensional Korteweg-deVries [2] and the two-dimensional Kadomtsev-Petviashvili equation [2]. For deep water waves, the nonlinear Schrödinger equation is a relevant model. There are also models that incorporate a term representing surface tension effects, such as the one seen in the Kawahara equation. There has also been a lot of focus on water waves on the whole line. We focus mainly on the literature that presents the solutions to the full Euler's equations for the periodic system. We restrict our attention to the results for water waves with a one-dimensional surface. This work can be extended to fully three-dimensional surface as was done in [72] for gravity waves, but we have not pursued this yet.

This chapter is structured the following way. First, a discussion of the history of the computation of traveling wave solutions is presented. Next, we review the literature on the investigation of their stability properties. Since the focus of this work is the effect of surface tension, special attention is given to its contribution. We finish this chapter with results that are specific to waves with surface tension, i.e., gravity-capillary waves.

2.2 Background

Stokes was the first to construct periodic solutions to the nonlinear Euler's equations in 1847. He introduced a form for a graph of a travelling wave on a periodic domain [81]. This was done perturbatively by adding successive harmonics of a cosine profile. In 1880, he found there is a gravity wave of maximum height that is achieved when the distance from crest to trough is 0.142 wavelengths [18]. The first paper to show that such a series expansion in powers of the wave amplitude (or Stokes' expansion) converges was by Nekrasov (1921) [71] and Levi-Civita (1925) [57]. They showed that the Stokes series converges when the ratio of amplitude to wavelength is sufficiently small and the waves are in infinitely deep water. Struik (1926) [83] extended this analysis for water of finite depth.

Examining periodic surface gravity-capillary waves using an expansion like the one used by Stokes, Wilton (1915) [92] computed successive coefficients, including the effects of surface tension. He showed that if the coefficient of surface tension in infinitely deep water is proportional to $1/n$, where n is an integer, the denominator of the expansion coefficients approaches zero. Since the terms of the series are computed only up to a scaling, he postulated that if you equate the constant in front of the n-th harmonic to be proportional to the vanishing denominator, convergence of the series may once again be achieved, thus reordering the series. These solutions are referred to as Wilton ripples and have been observed in experiments such as the one by Henderson and Hammack [40].

Following Stokes's discovery of a wave of greatest height for gravity waves [81], Crapper investigated the possibility of a wave of maximum height for purely capillary waves. Using a series expansion similar to Stokes (1957), he wrote down an exact solution for capillary waves of arbitrary amplitude on an infinitely deep fluid, and he concluded a similar result was possible for finite depth. He found that for infinite depth, the wave of greatest height occurs when the distance from crest to trough is 0.73 wavelengths.

2.3 Solutions

Euler's equations are hard to solve as written. Many different ways of reformulating Euler's equations exist, mainly aimed at avoiding having to solve Laplace's equation on an unknown

domain. A lot of these reformulations rewrite the system only in terms of the surface variables, first introduced by Zakharov [94]. We mention some such methods, but for a more comprehensive comparison, see [90]. One method is using conformal mapping (CM) [29] to solve the one-dimensional water wave problem. This leads to equations such as the ones used by Longuet-Higgins and Cokelet (1976) [60] or even to the boundary integral methods used by Vanden-Broeck et al. [86]. However, the CM approach does not easily extend to the three-dimensional equations. Another approach defines a Dirichlet-to-Neumann operator (DNO), see Craig and Sulem (1993) [17]. A transformed field expansion method (TFE) developed by Bruno and Reitich [13], is currently used on the water wave problem by Akers and Nicholls where they include the effects of surface tension [3]. The last method to consider, different from the one in this thesis, is the boundary integral method (BIM) used by Wilkening [90]. It does extend to three-dimension, but computationally, it is hard to set up.

We are building on the work of Deconinck and Oliveras (2011) [25]. That means the method most relevant to us is the reformulation due to Ablowitz, Fokas and Musslimani (2006) [1]. In this thesis, we rewrite the water wave problem as two coupled equations, one local and one nonlocal. This method is discussed in more detail in later sections.

Using the different reformulations, many have computed solutions to Euler's equations. It is important to mention some major results by some key contributors. There are two main cases to consider, solutions to water wave equations on the whole line leading to solitary waves, or solutions on a periodic domain. Within these, people often examine different limits such as shallow and deep water waves. For each of these, we can examine waves where the only force acting on the motion is gravity (gravity waves) or surface tension (capillary waves) as well as waves with both forces having a contribution (gravity-capillary waves). Another important classification of solutions is by the dimension of the surface, one or two-dimensional (a two-dimensional surface leads to a fully three-dimensional problem). For waves on the whole line, solutions are divided into waves of depression or elevation. One can also examine wave packets, interaction of several different waves and many more complicated scenarios, but since we focus on periodic waves in this thesis, we will not mention the more complicated full line situations any further. However, solitary waves as

well as their stability have been examined in [59], [14], [74], [52], [70] as well as many other papers.

One of the most prolific contributors to the field has been J.-M. Vanden-Broeck. In his book [86], he collects some of the results from his numerous papers (such as [78] and [42] for the case of periodic gravity-capillary waves) and discusses the intricacies involved when the effects of surface tension are included in the computation of solutions to Euler's equations. He outlines the boundary integral method as well as other numerical schemes. He explicitly shows how Wilton ripples arise and how this effects the ordering of the series for the solution. His book includes many forms of the solution for the periodic as well as the whole line problem. He includes bifurcation diagrams of the different types of solutions and how these curves are interrelated. However, he does not focus on the stability of those waves.

2.4 Stability of Solutions

With solutions to Euler's equations on the periodic domain in hand, it is important to address their stability. Phillips (1960) [37] examined the dynamics of gravity waves on the surface of deep water and realized that when certain conditions are met, the waves behave as forced, resonant oscillators which cause energy transfer between the constituting wave trains. This work was supported by many experimental and numerical results such as the ones by Longuet-Higgins [60], McGoldrick [63] and others that are discussed in the next section. Phillips focussed on a perturbation series expansion and the conditions necessary for the higher-order terms to satisfy the linear dispersion relation. He showed that resonant triads are not possible for gravity waves in deep water. McGoldrick also showed such triads are possible when surface tension is incorporated [37].

Benjamin and Feir [7], Benjamin [6] as well as Whitham [87] derived the criterion that Stokes waves on sufficiently deep water, i.e., when the product of the wavenumber k and the fluid depth h is larger than 1.363, are modulationally unstable. For $kh < 1.363$, this instability is not present. Benjamin and Feir (1967) also showed this experimentally [7]. Benjamin acknowledged the work of Phillips, but derived the nonlinear interactions by his own methods which involved the interactions of waves of different frequencies.

Using a different approach, Zakharov (1968) wrote the seminal paper [94] about the stability of surface waves on a deep fluid. Starting from Euler's equations, he showed that the system is Hamiltonian. He derived a form for the energy in terms of the canonical variables, the wave profile and velocity potential of the wave evaluated at the surface. The resulting equation which is accurate to fourth order, is now known as the Zakharov equation. He concluded that in an appropriate set of normal variables the cubic interaction terms cancel.

By linearizing around the steady state solutions, a stability eigenvalue problem can be obtained for the water wave equations. By examining the equality of the eigenvalues (*i.e.*, locally the eigenvalue problem looks like a forced harmonic oscillator), McLean (1982) [68], [67] found there are two classes of instabilities that should be considered. He stated that these two classes encompass both the Benjamin-Feir instability as well as the resonance curves found by Phillips. In addition, other previously unclassified instabilities were found. McLean also obtained maximal growth rates for instabilities as a function of wave steepness.

Another way to investigate the spectral problem is to use the Hamiltonian nature of the problem. In this framework, the sign of the quadratic term derived from the Hamiltonian gives an indication to when the collision of eigenvalues on the imaginary axis results in instablities. MacKay and Saffman (1986) [62] showed how the Hamiltonian for the water wave problem determined the behaviour of eigenvalues as a parameter is increased. In a more general context, this is part of the general theory of Krein signatures.

The stability of water waves on the whole line has been extensively analyzed ever since the observations by Scott Russell of solitary waves [75]. The literature on solitary waves is considerable. We focus mostly on the more recent and more relevant results, in particular on the work involving surface tension. Longuet-Higgins (1988) demonstrated numerically that, the limiting capillary-gravity waves exist in deep water [59]. It was found that solitary waves of depression are stable and solitary waves of elevation are unstable for infinitesimally small amplitude waves. The solutions become stable at finite steepness, see Calvo and Akylas (2001) [14]. The computation of solutions for gravity-capillary solitary waves was extended to three dimensions by Parau *et al.* (2004) [74] in infinite depth. It was found that these waves are unstable to perturbations transverse to the direction of propagation, but that they

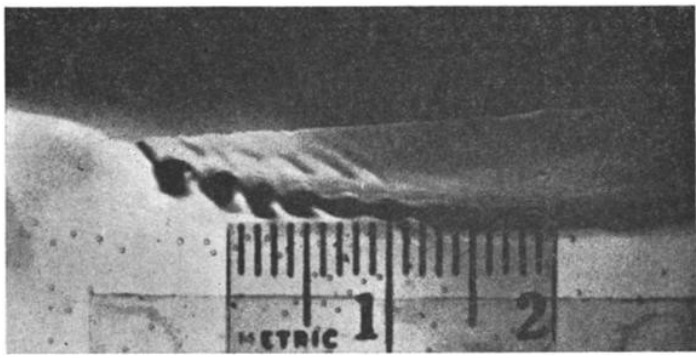

Figure 2.1: An image observed by Schooley [77] which shows a longer gravity wave with ripples due to capillary effects.

are stable to perturbations along the direction of propagation by Kim and Akylas (2007) [52]. Milewski *et al.* (2010) [70] analyzed the dynamics of interacting solitary waves.

2.5 Waves with surface tension

Why study the effects of surface tension? One reason to study surface tension, is to see what happens to the small high frequency instabilities found in [25]. Since surface tension resists external forces on a liquid, it is thought to be a stabilizing force [56]. After the instabilities were seen for gravity waves, it was thought that including even a small coefficient of surface tension in the model might act to eliminate those instabilities.

Another reason the effects of surface tension are important is that it has been seen to play a role in waves that are physically observed. It is thought that higher frequency waves generated on the surface of the ocean are mainly waves where the dominant force is surface tension [93]. These waves are often the prominent feature in field experiments and they are the dominant waves in satellite imagery. Capillary waves riding on top of gravity waves have been observed by Schooley [77], see Figure 2.1. The interesting question to ask is how stable these types of waves are and how likely they are to persist in water once they are generated. It is also thought that these capillary waves are the waves generated just before a wave breaks as seen by Duncan *et al.* [58] and seen here in Figure 2.2.

Experimentally, one can observe the effect surface tension plays on the type of waves

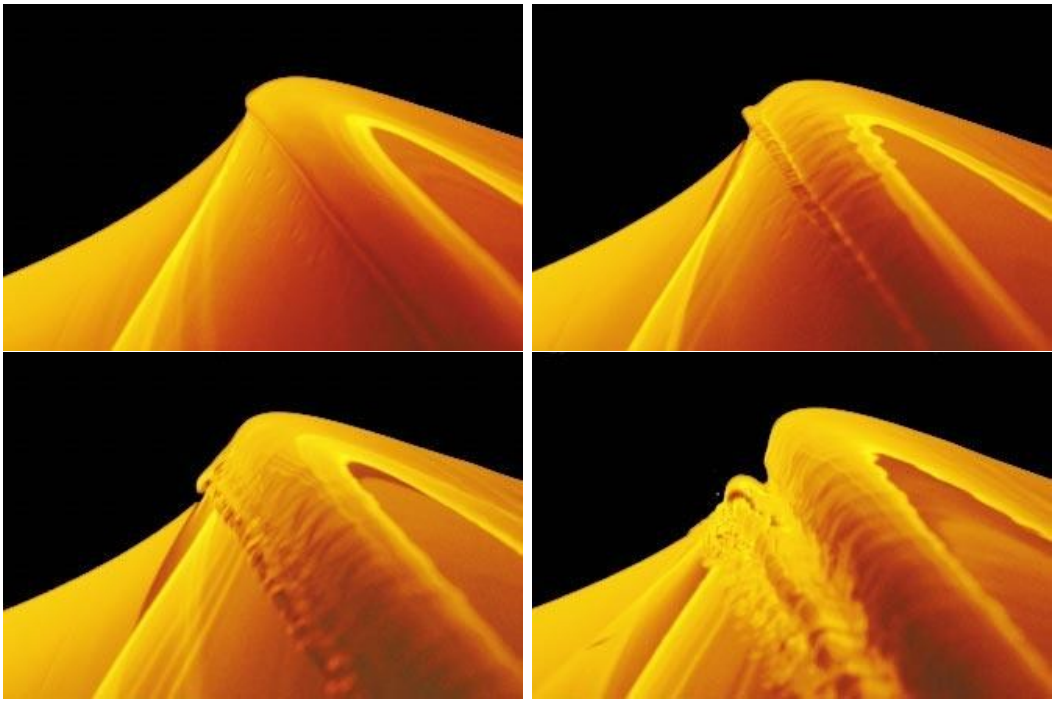

Figure 2.2: An experiment done by Duncan *et at.* [58] where wave breaking is observed through a sequence of images. It is important to note that the lead-up to wave breaking initiates capillary waves.

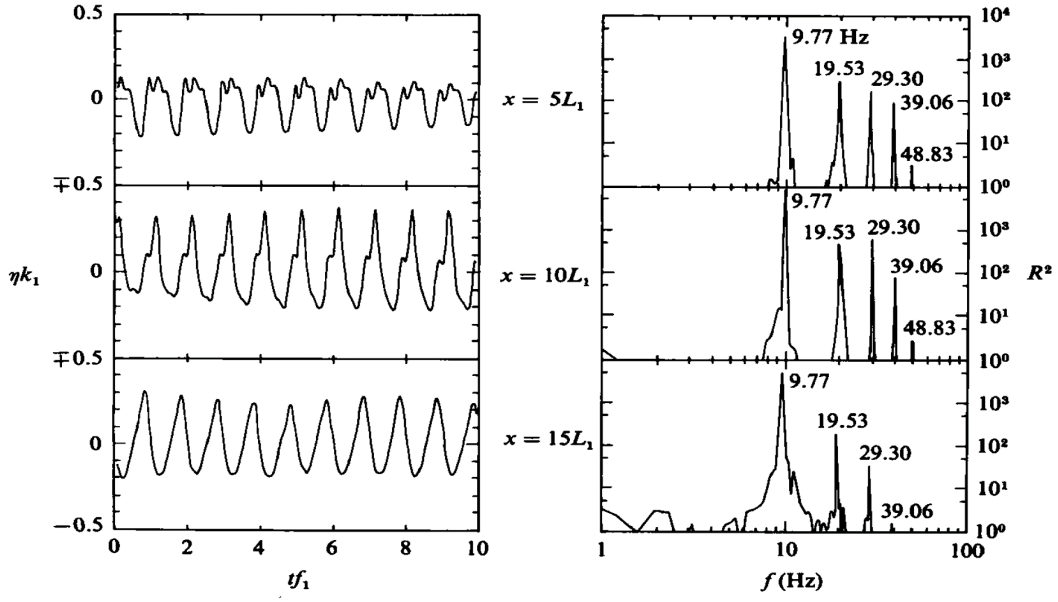

Figure 2.3: Observed waveforms (left) and frequencies (right) in a wave tank as they propagate down the tank [40]. The topmost plot is closest to wavemaker and the lowest is furthest down the tank. The waves sent into the tank were almost 20 Hz and it was shown that a wave of 10 Hz (a Wilton ripple) formed and grew in amplitude until it was dominant, illustrating the second harmonic Wilton ripple.

generated, as was done by Henderson and Hammack [40]. Waves on the surface of a tank were generated and observed as they propagated. In the experiment, several sensors were placed at different points along the tank measuring the profile and the frequencies that made up the wave as it travelled down the tank. It was found that even though waves of roughly 20 Hz were generated by the paddles at one end of the tank, frequencies that were about 10 Hz were observed as seen in Figure 2.3. This was a manifestation of Wilton ripples, an effect due to surface tension. One can ask how far down the tank can these waves propagate without being destroyed.

Perhaps one of the biggest contributions to understanding gravity-capillary waves and how they relate to resonant interactions is through several works by McGoldrick through experiment and theory. McGoldrick showed through experiments how gravity-capillary waves lose their original profile as they propagate [63]. He also examined gravity-capillary

waves using weakly nonlinear theory [64] and the method of multiple scales [65] showing how these gravity-capillary waves exist. Resonant phenomena such as Wilton ripples in the case of water waves have been studied in model equations [39] by adding resonant harmonics into the series expansion. Akers and Gao derive an explicit series solution for Wilton ripples.

Having a more complete picture of stability results for gravity-capillary waves fits into the existing literature. We know from work by Choi and Tiron [84] that Crapper's solutions [19] are unstable to subharmonic (long wave) perturbations. We know from work by Deconinck and Oliveras [25] that gravity waves are also unstable to subharmonic perturbations. Where do gravity-capillary waves fit in? Instabilities has been shown to exist by Jones in [49] [50], where the author analyzed a system of coupled differential equations approximating the interaction as a resonant phenomena. In the more recent paper [50], Jones looked at the second harmonic Wilton ripples and solved the asymptotic expansion to third order of the system. He examined the evolution of those solutions and showed that these are unstable to long wave perturbations.

2.6 Summary

There is a myriad of ways that Euler's equations can be solved. The method we choose to use is the one due to Ablowitz, Fokas and Musslimani [1]. We use the Fourier-Floquet-Hill method to analyze the spectral stability of fully nonlinear solutions [23]. The focus in this thesis, is on solutions that incorporate the effect of surface tension. We analyze the stability of these so-called gravity-capillary waves. This has not been done in great detail in the existing literature and the work done fills in the existing gap of what we know about the effects of surface tension on water waves.

Chapter 3

GRAVITY WAVES WITH SURFACE TENSION

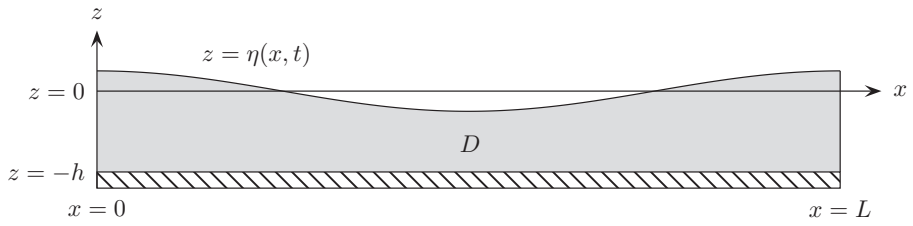

Figure 3.1: The domain on which we solve Euler's equations.

3.1 Introduction

In this chapter, we present the results from the paper "Stability of periodic gravity waves in the presence of surface tension" by Deconinck & Trichtchenko [26]. Recall that we are interested in solving the following problem

$$\begin{cases} \phi_{xx} + \phi_{zz} = 0, & (x,z) \in D, \\ \phi_z = 0, & z = -h,\ x \in (0,L), \\ \eta_t + \eta_x \phi_x = \phi_z, & z = \eta(x,t),\ x \in (0,L), \\ \phi_t + \dfrac{1}{2}\left(\phi_x^2 + \phi_y^2\right) + g\eta = \sigma \dfrac{\eta_{xx}}{(1+\eta_x^2)^{3/2}}, & z = \eta(x,t),\ x \in (0,L), \end{cases} \tag{3.1}$$

where h is the height of the fluid, g is the acceleration due to gravity and $\sigma > 0$ is the coefficient of surface tension[1]. Further, $\eta(x,t)$ is the elevation of the fluid surface, and $\phi(x,z,t)$ is its velocity potential. In this chapter, we focus on solutions on a periodic domain $D = \{(x,z) \mid 0 \le x < L, -h < z < \eta(x,t)\}$, see Fig. 3.1.

The work presented in this chapter follows that of Deconinck & Oliveras [25]. They presented a thorough numerical overview of the spectral instabilities of periodic traveling one-dimensional gravity (*i.e.*, $\sigma = 0$) water waves. An emphasis of that work is the presence of oscillatory instabilities even for waves in shallow water ($kh < 1.363$, see [6, 87], here $k = 2\pi/L$). Since the underlying waves are periodic, their stability analysis uses Hill's method, see [23], which incorporates the conclusions from Floquet's Theorem with Fourier

[1] As noted in [5], $\sigma > 0$ for liquid-gas interfaces.

analysis. This associates with each wave a range of Floquet exponents μ which may be taken as $(-\pi/L, \pi/L]$. The growth rates of the oscillatory instabilities is small, even for waves of moderate amplitude, and the range of Floquet exponents with which they are associated is narrow (on the order of 10^{-4} for $L = 2\pi$). A naive uniform distribution on $(-\pi/L, \pi/L]$ of Floquet exponents is bound to miss the presence of these instabilities, unless an exorbitantly large number of μ values are considered. Numerically, this is prohibitively expensive (often, no more than 100 μ-values are chosen), and an adaptive approach is used in [25], with more values of μ considered near those values of the Floquet exponents where instabilities may arise, as predicted by MacKay & Saffman [62].

Our goal is to investigate the effect of the inclusion of surface tension on the oscillatory instabilities. It is well known that the incorporation of capillary effects leads to the presence of resonances in the Fourier representation of the periodic traveling water waves. If the resonance condition $R(\sigma, g, h, L) = 0$ is satisfied, so-called Wilton ripples are found [86, 92]. Even when $R(\sigma, g, h, L) \neq 0$, its value can be made arbitrarily small by the consideration of Fourier modes with sufficiently high wave number. This results in the presence of small denominators in the Stokes expansion of the wave profile. This is especially problematic for waves of moderate or high amplitude, whose accurate Fourier representation requires more modes. This is discussed in more detail in Sections 3.3 and 3.4. Because of this, we limit our investigations to the instabilities of waves of small amplitude, so that (near-) resonance is avoided. Waves in both shallow and deep water are considered.

The layout of this chapter is the following. Section 3.2 discusses the reformulation of the water wave problem we use, both for the computation of the traveling wave solutions, and for the analysis of their stability. After that, different sections are devoted to the computation of the solutions and to the numerical investigation of their spectral stability. In addition, we revisit the work of MacKay & Saffman [62], which allows for an analytical prediction of which modes may lead to instabilities. We finish with conclusions.

3.2 Reformulation

The reformulation of (3.1) of Ablowitz, Fokas and Musslimani [1] follows the work of Zakharov [94] by writing the water wave problem in terms of just the surface variables $\eta(x, t)$

and $q(x,t) = \phi(x, \eta(x,t), t)$, the velocity potential evaluated at the surface. Ablowitz, Fokas and Musslimani [1] show that the two functions $\eta(x,t)$ and $q(x,t)$ satisfy the system

$$q_t + \frac{1}{2}q_x^2 + g\eta - \frac{1}{2}\frac{(\eta_t + \eta_x q_x)^2}{1+\eta_x^2} = \sigma \frac{\eta_{xx}}{(1+\eta_x^2)^{3/2}}, \tag{3.2}$$

$$\int_0^L e^{ikx}\left[i\eta_t \cosh(k(\eta+h)) + q_x \sinh(k(\eta+h))\right] dx = 0, \quad \forall k \in \Lambda, \tag{3.3}$$

where $\Lambda = \{2\pi n/L \mid n \in \mathbb{Z},\ n \neq 0,\}$. In [1], only the whole line case is treated. The extension to the periodic case is straightforward [25]. As stated, equations (3.2) and (3.3) contain dimensional quantities. We use the same nondimensionalization as in [1], using the period as the characteristic length scale. In effect, this allows us to equate $g = 1$, $L = 2\pi$ and treat all quantities in (3.2) and (3.3) as nondimensional.

Following the derivation of Deconinck and Oliveras [25], we transform to a traveling frame of reference, moving with speed c. Thus implies the substitution $x \to x - ct$, $\eta_t \to \eta_t - c\eta_x$ and $q_t \to q_t - cq_x$. The local and nonlocal equations (3.2) and (3.3) become

$$q_t - cq_x + \frac{1}{2}q_x^2 + g\eta - \frac{1}{2}\frac{(\eta_t - c\eta_x + \eta_x q_x)^2}{1+\eta_x^2} = \sigma \frac{\eta_{xx}}{(1+\eta_x^2)^{3/2}}, \tag{3.4}$$

$$\int_0^L e^{ikx}\left(i(\eta_t - c\eta_x)\cosh(k(\eta+h)) + q_x \sinh(k(\eta+h))\right) dx = 0, \quad k \in \Lambda. \tag{3.5}$$

Traveling wave solutions are stationary in this frame of reference, thus $q_t = 0 = \eta_t$. We solve for q_x using the local equation:

$$q_x = c - \sqrt{(1+\eta_x^2)\left(c^2 - 2g\eta + 2\sigma\frac{\eta_{xx}}{(1+\eta_x^2)^{3/2}}\right)}, \tag{3.6}$$

where we have chosen the negative sign in front of the square root [16]. Substituting in the nonlocal equation (3.5), integrating by parts and simplifying, we are left with

$$\int_0^L e^{ikx}\sqrt{(1+\eta_x^2)\left(c^2 - 2g\eta + 2\sigma\frac{\eta_{xx}}{(1+\eta_x^2)^{3/2}}\right)}\sinh(k(\eta+h))dx = 0, \quad k \in \Lambda. \tag{3.7}$$

Alternatively,

$$\int_0^L e^{ikx}\sqrt{(1+\eta_x^2)\left(c^2 - 2g\eta + 2\sigma\frac{\eta_{xx}}{(1+\eta_x^2)^{3/2}}\right)}\left(\sinh(k\eta) + \cosh(k\eta)\tanh(kh)\right) dx = 0, \quad k \in \Lambda, \tag{3.8}$$

where we have separated the explicit dependence on the depth h. This is useful for numerical purposes, and it allows for an easy limit when considering the case of water of infinite depth. Indeed, in the limit $h \to \infty$, (3.8) gives

$$\int_0^L e^{ikx} \sqrt{(1+\eta_x^2)\left(c^2 - 2g\eta + 2\sigma \frac{\eta_{xx}}{(1+\eta_x^2)^{3/2}}\right)} e^{|k|\eta} dx = 0, \quad k \in \Lambda. \tag{3.9}$$

In what follows, we equate the solution period L to 2π. Thus $\Lambda = \{n \mid n \in \mathbb{Z},\ n \neq 0, \}$.

3.3 Constructing traveling-wave solutions

We construct solutions to (3.8) (or (3.9)) using numerical continuation. AUTO [28] and MatCont [36] are often used for this purpose. For our equations these software packages are difficult to use because of the nonlocality present. Instead, we wrote our own continuation program. The trivial solution $\eta = 0$ satisfies (3.8) for all values of c. At particular values of the wave speed c the equation admits nontrivial solutions as well, and bifurcation branches emanate. To determine these values of c, we linearize (3.8):

$$\int_0^{2\pi} e^{ikx} \left[c^2\eta + (-g\eta + \sigma\eta_{xx}) \frac{\tanh(kh)}{k}\right] dx = 0, \quad k \in \Lambda. \tag{3.10}$$

With[2]

$$\eta = \sum_{n=1}^{\infty} a_n \cos(nx),$$

the linearized equation becomes

$$\left[c^2 - \left(g + k^2\sigma\right) \frac{\tanh(kh)}{k}\right] a_k = 0, \quad k \in \Lambda. \tag{3.11}$$

We impose that for $k = 1$, the factor in brackets is zero, so that

$$c = \sqrt{(g+\sigma)\tanh(h)}, \tag{3.12}$$

[2]This form of η equates the average of the free surface to zero, without loss of generality.

and a_1 is not forced to be zero. Then, for almost all values of σ,

$$\eta = a_1 \cos(x), \tag{3.13}$$

where a_1 is an arbitrary constant. Near $c = \sqrt{(g+\sigma)\tanh(h)}$, (3.8) with a_1 sufficiently small, is an accurate representation of the solution. To compute $\eta(x)$ as we continue up the branch, we use Newton's method in Fourier space as described below. This results in a finite-term Fourier representation of the solution, which is truncated at whatever order guarantees the numerical accuracy desired.

There are particular values of σ for which the factor in parentheses in (3.11) is zero for a second value of $k \neq 1$, once c has been chosen as in (3.12). In this case, the linear solution consists of two terms, leading to resonant solutions or Wilton ripples [86]. Since the goal of our work is to examine the effect of small surface tension on gravity waves, we wish to stay away from the resonance phenomenon. The factor seen in (3.11) appears at all orders. More explicitly, the resonance condition is given by

$$(g+\sigma)\tanh(h) - \left(g + k^2\sigma\right)\frac{\tanh(kh)}{k} = 0. \tag{3.14}$$

This equation can be solved (numerically) for k, as a function of g, h, and σ. For most parameter values, the solution k is not an integer, implying that resonance does not occur. However, for computational purposes we need to avoid near resonances as well. Near resonances occur for integer values of k near the solution of (3.14). This leads to small denominators in terms with these wave numbers in the Fourier series of the solution, which presents numerical difficulties, unless their numerators are even smaller[3]. Thus, in order to have a well-resolved solution, we need to stay away from Fourier modes that satisfy (3.14) or for which the residual of this equation is small.

For fixed g and two different values of h ($h = 0.5$, shallow water, dashed line, and $h = 1.5$, deep water, solid line), Figure 3.2 displays the solution of (3.14) in the (k, σ) plane. For

[3]This happens if the near-resonance occur for sufficiently high wave number terms, which are not necessary for the accurate numerical evaluation of the series.

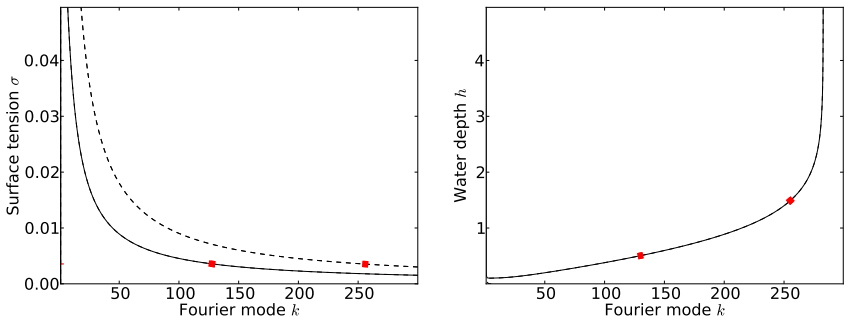

(a) (b)

Figure 3.2: Figure (a) displays the solution set of the resonance condition for different Fourier modes k and different values of the coefficient of surface tension, for both deep (solid curve) and shallow water (dashed curve). The red dots indicate the resonant k values for $\sigma = 1/(90\pi)$. Figure (b) displays the solution set as a function of depth h and wave number k, for $\sigma = 1/(90\pi)$ and the red dots correspond to the values of the depth we use, $h = 0.5$ (shallow water) and $h = 1.5$ (deep water).

instance, the figure shows that for $\sigma = 1/(90\pi)$, near resonance and the small-denominator problem in the Fourier series occur near the 125th and the 260th mode for deep and shallow water respectively. Provided that the desired accuracy of the solution under consideration is achieved with far fewer terms, near resonance is not a problem. For our purposes, we let $\sigma = 1/(90\pi)$, and we consider solutions that require never more than 100 terms in their Fourier expansion to achieve the numerical accuracy desired. This imposes a *de facto* restriction on the amplitude of the solution we consider, while allowing for solutions that, although not of maximal amplitude, are decidedly in the nonlinear regime. Our solutions never exceed 50% of the maximal wave height. It should be noted that for $\sigma = 0$, resonance is not possible. Also, in the limit of water of infinite depth, resonance occurs for $k = g/\sigma$.

3.3.1 Numerical Implementation

In order to construct the solutions numerically, using a continuation method, we truncate the number of Fourier modes of the solution to a finite integer N. Let

$$\eta_N(x) = \sum_{j=1}^{N} a_j \cos(jx). \tag{3.15}$$

Recall that the nonlocal equation (3.8) is valid for every integer $k \neq 0$. We truncate the number of equations to N so that $k = 1, \ldots, N$. However the speed c at which the wave moves is an additional unknown. Thus an extra equation is required. Different options are possible and their convenience is dictated by how we parameterize the solution bifurcation branch. If we parametrize using a_1, then we can either prescribe a_1 as a variable or we can add the equation

$$a_1 - \tilde{a}_1 = 0,$$

where $\tilde{a}_1$ is a prescribed value, determining the next solution on the bifurcation branch. Parameterizing using a_1 is a convenient and justifiable choice for solutions of small amplitude. As the amplitude is increased, this may cease to be the case, but since we are limiting ourselves to solutions of small and moderate amplitude, this is not an issue for us. Alternatively, one could prescribe the L^2 or L^∞ norm of the solution, as was done in [25]. In any case, we end with $N + 1$ equations determining $N + 1$ unknowns.

Remark. We may overdetermine the number of equations so as to solve a least-squares problem. However, this requires the use of additional values of $k > N$. Since for large values of k, the cosh and sinh contributions in the nonlocal equation become large exponentially fast, this must be done with care to control numerical error.

Denote the vector of unknowns as

$$z = [c, a_1, a_2, a_3, \ldots, a_N]^T.$$

Equating

$$F^{(N)}(z) = [a_1 - \tilde{a}_1, F_1(z), F_2(z), \ldots, F_N(z)]^T,$$

where $\tilde{a}_1$ is given as a small increment of the value at the previous solution, and

$$F_j^{(N)}(z) = \int_0^{2\pi} e^{ijx} \sqrt{\left(1+\eta_{N,x}^2\right)\left(c^2 - 2g\eta_N + 2\sigma \frac{\eta_{N,xx}}{(1+\eta_{N,x}^2)^{3/2}}\right)} \cdot (\sinh(k\eta_N) + \cosh(k\eta_N)\tanh(kh))dx$$
$$= \int_0^{2\pi} f_j(k, c, \eta_N, \eta_{N,x}, \eta_{N,xx})dx,$$

which defines $f_j(k, c, \eta_n, \eta_{N,x}, \eta_{N,xx})$. We wish to solve $F^{(N)}(z) = 0$ for the unknown vector z. Using Newton's Method, the n-th iteration is given by

$$z^{n+1} = z^n - J^{-1}(z^n)F(z^n),$$

where J is the Jacobian with entries

$$(J)_{jl} = \frac{\delta F_j}{\delta z_l} = \int_0^{2\pi} \left(\frac{\partial f_j}{\partial z_l} + \frac{\partial f_j}{\partial \eta_N}\frac{\partial \eta_N}{\partial z_l} + \frac{\partial f_j}{\partial \eta_{N,x}}\frac{\partial \eta_{N,x}}{\partial z_l} + \frac{\partial f_j}{\partial \eta_{N,xx}}\frac{\partial \eta_{N,xx}}{\partial z_l}\right) dx,$$

which is readily computable. Using the form (3.15), all spatial derivatives are computed analytically. This is in contrast to [25] where spatial collocation was used. Integration is performed using the trapezoidal rule.

Our continuation method starts from flat water, after which we proceed to follow the bifurcation branch with initial guess

$$[\sqrt{(g+\sigma)\tanh(h)}, \tilde{a}_1, 0, 0, 0, \ldots, 0]^T.$$

This initial guess is modified as we proceed up the branch. Python and Matlab both are used to implement the numerical scheme. To check the convergence of the algorithm, we check the residual error as well as the decay in the Fourier modes of the solution. Results are given below. The continuation is started using N=20 Fourier modes only, due to the small amplitude of the solution. Only a few of the 20 modes are distinguishable from 0 initially. As the bifurcation parameter is increased, more than 20 modes are needed to accurately represent the solution. The value of N is increased acoordingly, *i.e.*, more

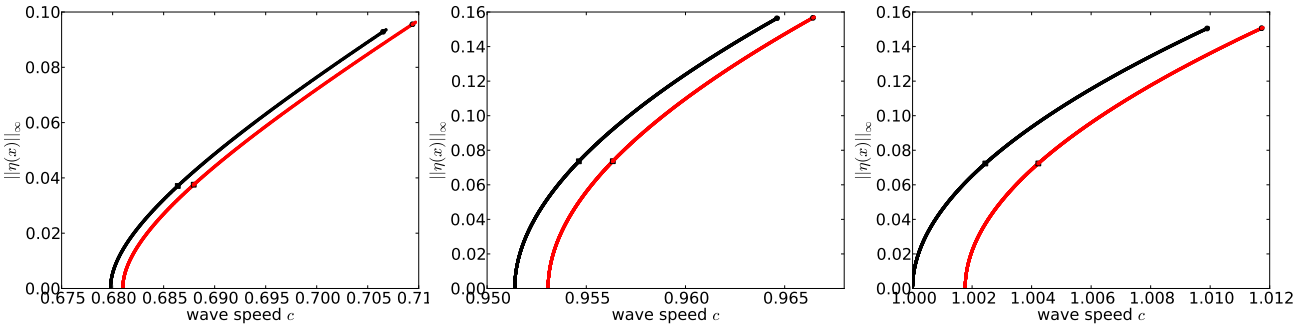

(a) (b) (c)

Figure 3.3: The solution bifurcation branches for pure gravity waves ($\sigma = 0$, black) and gravity-capillary waves ($\sigma = 1/(90\pi)$, red) for (a) shallow water, $h = 0.5$, (b) deep water, $h = 1.5$ and (c) water of infinite depth.

equations are used, depending on more unknowns. This is limited by the presence of the exponentially growing functions, which is why we work with solutions that are accurately represented using no more than 100 Fourier modes. Throughout the exponential decay of the Fourier amplitudes that is expected of an analytic solution profile is checked, ensuring that the computed modes with highest wave number have neglible (less than 10^{-14}) Fourier amplitude.

3.3.2 Numerical Results

We compare the computed traveling wave profiles for particular values of the depth h, with and without surface tension. The value $\sigma = 1/(90\pi)$ is used throughout. The solution bifurcation branches are shown in Figure 3.3. The case of no surface tension is shown in black, while $\sigma = 1/(90\pi)$ is red. This convention is used throughout the thesis. The top row of Figure 3.4 displays the actual solution profile, divided by $\eta(0)$, to allow for the comparison of profiles of different amplitudes. Different columns show the results for different depth h, with $h = 0.5$, $h = 1.5$, and $h = \infty$ in order. The bottom row of Figure 3.4 shows the exponential decay of the Fourier coefficients of the computed solutions. It is clear that the effect of small surface tension on the solution profile is perturbative only: no qualitative

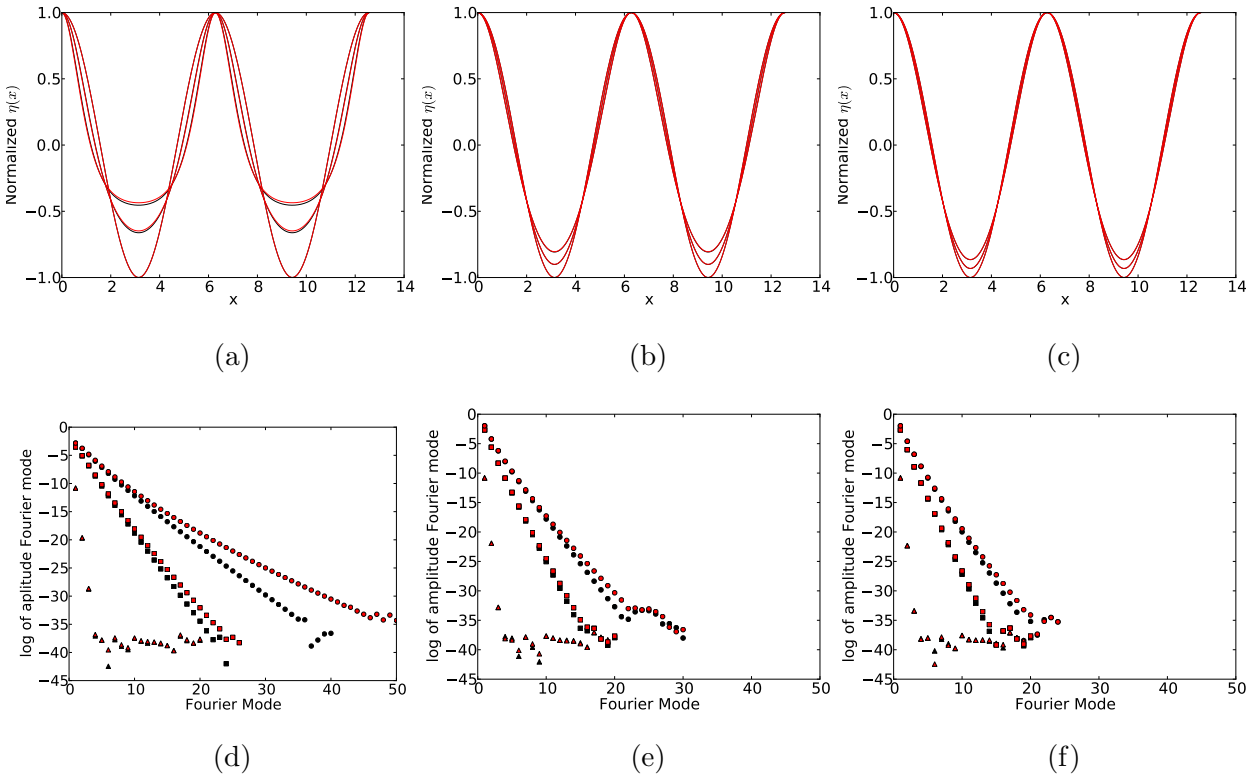

Figure 3.4: Solution profiles $\eta(x)/\eta(0)$ for (a) shallow water, $h = 0.5$, (b) for deep water, $h = 1.5$, and (c) for water of infinite depth, $h = \infty$. Note that in deep water, the profiles of pure gravity waves (black) and gravity-capillary waves (red) with $\sigma = 1/(90\pi)$ are almost indistinguishable. The exponential decay of the Fourier modes for the corresponding solutions is shown in the bottom row.

changes are discernible and quantitative changes are small.

In the top row of Figure 3.4, normalized wave profiles with higher troughs correspond to solutions higher on the bifurcation branches of Figure 3.4. Those solutions are also the profiles for which the decay of the Fourier amplitudes is the slowest. Accordingly, the Fourier representation of the profile requires more terms for comparable numerical accuracy. It appears that the inclusion of surface tension requires more Fourier modes for the accurate representation of the solution.

3.4 Stability

Next, we consider the spectral stability of these solutions. Our main interest is in comparing these results with those of Deconinck and Oliveras [25], where $\sigma = 0$. Since our traveling wave solutions are periodic, we use the Fourier-Floquet-Hill method [23] and follow the setup of [25]. Spectral stability of a solution is defined as

Definition 1. *(**Spectral Stability**). The equilibrium solution $u_0(x)$ of a dynamical system $u_t = \mathcal{N}(x, u, u_x, \ldots)$ is spectrally stable if the spectrum of the linear operator obtained by linearizing $\mathcal{N}$ around $u_0(x)$ has no strictly positive real part.*

This implies that perturbations of this solution do not exhibit exponential growth. Assume we have a linear operator $\mathcal{L}$ with elements λ of its spectrum such that

$$\mathcal{L}v = \lambda v.$$

The spectrum of a linear operator is defined in the standard way [41]:

Definition 2. *(**Spectrum of a Linear Operator**). The spectrum of the linearized operator $\mathcal{L}$ is given by*

$$\sigma(\mathcal{L}) = \{\lambda \in \mathbb{C} : \mathcal{L}v = \lambda v \text{ and } ||v(x)||_\infty < \infty\}. \tag{3.16}$$

For our purposes, the norm $||\cdot||_\infty$ denotes the infinity norm. Let the form of the solution to the equations (3.4) and (3.5) in the traveling frame of reference be

$$q(x,t) = q_0(x) + \epsilon q_1(x) e^{\lambda t} + O(\epsilon^2), \tag{3.17}$$

$$\eta(x,t) = \eta_0(x) + \epsilon \eta_1(x) e^{\lambda t} + O(\epsilon^2), \tag{3.18}$$

where η_0 is obtained from the numerical scheme described in the previous section and q_0 follows from (3.6). Since the water wave problem is Hamiltonian [94] the spectrum (3.16) of any traveling wave solution is symmetric with respect to both the real and imaginary axes.

Thus, in order for the solution to be spectrally stable, it is necessary for the spectrum to be on the imaginary axis, *i.e.*, $Re\{\lambda\} = 0$, for all λ in $\sigma(\mathcal{L})$.

We do not restrict the period of the perturbations q_1 and η_1, which is possible by using Floquet's Theorem [44, 23]. For our problem, this implies that perturbations may be decomposed as

$$q_1(x) = e^{i\mu x}\tilde{q}_1, \quad \eta_1(x) = e^{i\mu x}\tilde{\eta}_1, \tag{3.19}$$

where $\mu \in [-1/2, 1/2)$ is the Floquet exponent and $\tilde{q}_1$, $\tilde{\eta}_1$ are periodic with period 2π. It is straightforward to apply the Floquet Theorem to the local equation, but the nonlocal case requires modification: before perturbing (3.5) using perturbations of the form (3.19) with arbitrary period, we replace the integral over one period by the average over the whole line [25]:

$$\langle f(x)\rangle = \lim_{M\to\infty} \frac{1}{M}\int_{-M/2}^{M/2} f(x)dx, \tag{3.20}$$

which is defined for almost periodic $f(x)$, which includes (quasi-) periodic $f(x)$ as in (3.19) [8]. The generalized local equation is identical to the previous one if the integrand is periodic.

3.4.1 The Generalized Eigenvalue Problem

We linearize the following system of equations about a traveling wave solution:

$$q_t - cq_x + \frac{1}{2}q_x^2 + g\eta - \frac{1}{2}\frac{(\eta_t - c\eta_x + q_x\eta_x)^2}{1+\eta_x^2} = \sigma\frac{\eta_{xx}}{(1+\eta_x^2)^{3/2}}, \tag{3.21}$$

$$\lim_{M\to\infty}\frac{1}{M}\int_{-M/2}^{M/2} e^{ikx}\left[i(\eta_t - c\eta_x)\cosh(k(\eta+h)) + q_x\sinh(k(\eta+h))\right]dx = 0, \quad k\in\Lambda. \tag{3.22}$$

Using (3.17-3.18), ignoring terms of $O(\epsilon^2)$ and higher, and dropping the tildes, we obtain

$$\lambda\left(f\eta_1 - q_1\right) = (q_{0,x} - c)\mathcal{D}_x q_1 + g\eta_1 - f\left[(q_{0,x} - c)\mathcal{D}_x\eta_1 + \eta_{0,x}\mathcal{D}_x q_1\right] + f^2\eta_{0,x}\mathcal{D}_x\eta_1 - \sigma\frac{\mathcal{D}_x^2\eta_1}{1+\eta_{0,x}^{3/2}} + \sigma\frac{3\eta_{0,xx}\eta_{0,x}\mathcal{D}_x\eta_1}{(1+\eta_{0,x}^2)^{5/2}}, \tag{3.23}$$

$$\lambda\left\langle e^{ikx}\left[-i\mathcal{C}_k\eta_1\right]\right\rangle = \left\langle e^{ikx}\left[-i\mathcal{C}_k c\mathcal{D}_x\eta_1 + \mathcal{S}_k\mathcal{D}_x q_1 + \left(-i\eta_{0,x}c\mathcal{S}_k + q_{0,x}\mathcal{C}_k\right)k\eta_1\right]\right\rangle, \tag{3.24}$$

where

$$f(\eta_0, q_0) = \frac{\eta_{0,x}(q_{0,x} - c)}{1+\eta_{0,x}^2}, \qquad \mathcal{D}_x = i\mu + \partial_x,$$

$$\mathcal{S}_k = \sinh(k(\eta_0 + h)), \qquad \mathcal{C}_k = \cosh(k(\eta_0 + h)), \qquad \mathcal{T}_k = \tanh(k(\eta_0 + h)).$$

Since q_1 and η_1 are periodic with period 2π,

$$q_1 = \sum_{m=-\infty}^{\infty} Q_m e^{imx}, \quad \eta_1 = \sum_{m=-\infty}^{\infty} N_m e^{imx}, \tag{3.25}$$

with

$$Q_n = \frac{1}{2\pi}\int_0^{2\pi} e^{-inx} q_1(x)dx, \qquad N_n = \frac{1}{2\pi}\int_0^{2\pi} e^{-inx}\eta_1(x)dx. \tag{3.26}$$

Truncating to the $2N+1$ Fourier modes from $-N$ to N, we define

$$U(x) = \left[N_{-N}(x), \ldots, N_0(x), \ldots, N_N(x), Q_{-N}(x), \ldots Q_0(x), \ldots, Q_N(x)\right]^T. \tag{3.27}$$

This leads to the finite-dimensional generalized eigenvalue problem

$$\lambda\mathcal{L}_1 U(x) = \mathcal{L}_2 U(x). \tag{3.28}$$

where

$$\mathcal{L}_1 = \begin{bmatrix} A & -I \\ C & 0 \end{bmatrix}, \quad \mathcal{L}_2 = \begin{bmatrix} S & T \\ U & V \end{bmatrix} \tag{3.29}$$

with I and 0 the $(2N+1)\times(2N+1)$ identity and zero matrix, respectively. The blocks A, S and T originate from the local equation, while C, U and V come from the nonlocal equation. Their matrix entries are

$$\begin{aligned}
A_{m,n} &= \frac{1}{2\pi}\int e^{i(m-n)x} f\,dx, \quad C_{m,n} = -i\frac{1}{2\pi}\int e^{i(m-n)x}\mathcal{C}_{\mu+m}dx,\\
S_{m,n} &= -\frac{1}{2\pi}\int e^{i(m-n)x}\Big[-g + f(q_{0x}-c)i(\mu+(m-N)) - f^2\eta_{0x}i(\mu+(m-N))\\
&\qquad +\sigma\frac{-(\mu+(m-N))^2}{1+\eta_{0x}^2} - \sigma\frac{2\eta_{0xx}\eta_{0x}i(\mu+(m-N))}{(1+\eta_{0x}^2)^2}\Big]\,dx,\\
T_{m,n} &= \frac{1}{2\pi}\int e^{i(m-n)x}\left[(q_{0x}-c)i(\mu+(m-N)) - f\eta_{0x}i(\mu+(m-N))\right]dx,\\
U_{m,n} &= \frac{1}{2\pi}\int e^{i(m-n)x}\left[S_{\mu+m}i(\mu+(m-N))\right]dx,\\
V_{m,n} &= \frac{1}{2\pi}\int e^{i(m-n)x}\left[-ic(\mu+(m-N))\mathcal{C}_k + k(-i\eta_{0x}c\mathcal{S}_{\mu+m}) + q_{0x}\mathcal{C}_{\mu+m}\right]dx.
\end{aligned}$$

Lastly,

$$\begin{aligned}
\mathcal{C}_{\mu+m} &= \cosh((\mu+m)\eta_0) + \mathcal{T}_{\mu+m}\sinh((\mu+m)\eta_0),\\
\mathcal{S}_{\mu+m} &= \sinh((\mu+m)\eta_0) + \mathcal{T}_{\mu+m}\cosh((\mu+m)\eta_0),
\end{aligned}$$

with $\mathcal{T}_{\mu+m} = \tanh((\mu+m)h)$. All block matrices in (3.29) are of size $(2N+1)\times(2N+1)$ with N being the number of modes we retain. The convergence properties of the Floquet-Fourier-Hill method as $N\to\infty$ are discussed in [20, 45].

3.4.2 A Necessary Condition for Instabilities

Since the traveling wave solutions of Section 3.3 are constructed through numerical continuation from the trivial flat water state, it is natural to begin by considering the spectral stability of the flat water state. This is conveniently done using the Hamiltonian form of the

problem, following Mackay and Saffman [62] and using notions from resonant interaction theory, as in [68]. These concepts are particularly easy to use in the flat water case, since the spectral problem (3.23-3.24) is one with constant coefficients. It is well known that the eigenvalues corresponding to different Floquet exponents do not interact, thus we may restrict our attention to a fixed μ value. It may be convenient to not restrict μ to the unit interval around the origin, keeping in mind that values of μ that have the same non-integer part are equivalent.

For flat water, $\eta_0 \equiv 0$, $q_0 \equiv 0$, and the spectral problem (3.23-3.24) becomes

$$\lambda\left(-q_1\right) = (-c)\mathcal{D}_x q_1 + g\eta_1 - \sigma\mathcal{D}_x^2\eta_1,$$
$$\lambda\left(-i\mathcal{C}_{\mu+m}\eta_1\right) = -i\mathcal{C}_{\mu+m}c\mathcal{D}_x\eta_1 + \mathcal{S}_{\mu+m}\mathcal{D}_x q_1.$$

This system is easily solved, and the eigenvalues are explicitly given by

$$\lambda^s_{\mu+m} = ic(\mu+m) + is\sqrt{\left[g(\mu+m) + \sigma(\mu+m)^3\right]\mathcal{T}_{\mu+m}}, \tag{3.30}$$

with $s = \pm 1$. At this point the assumption $\sigma > 0$ mentioned in the footnote on page 1 is shown to be vital: if $\sigma < 0$ it is clear that the flat water state is not spectrally stable, and we end up with a variety of nonphysical and unobserved instabilities for surface water waves. With this assumption, all eigenvalues are on the imaginary axis and the flat water state is spectrally stable. The spectrum of (3.23-3.24) is a continuous function of the parameters appearing in $\mathcal{L}_1$ and $\mathcal{L}_2$ [41], including the traveling wave amplitude. In order for eigenvalues to leave the imaginary axis, they have to do so in pairs, symmetric with respect to both the real and imaginary axis. This is only possible through eigenvalue collisions, which are a necessary condition for the development of instabilities [61]. Thus we examine for which parameter values different eigenvalues given by (3.30) collide. This was originally investigated by MacKay and Saffman [62], who found that eigenvalues with the same sign s do not collide. Otherwise the collision condition becomes

$$\lambda^{s_1}_{\mu} = \lambda^{s_2}_{\mu+m} \quad \text{for any } m \in \mathbb{Z}, s_1 \neq s_2. \tag{3.31}$$

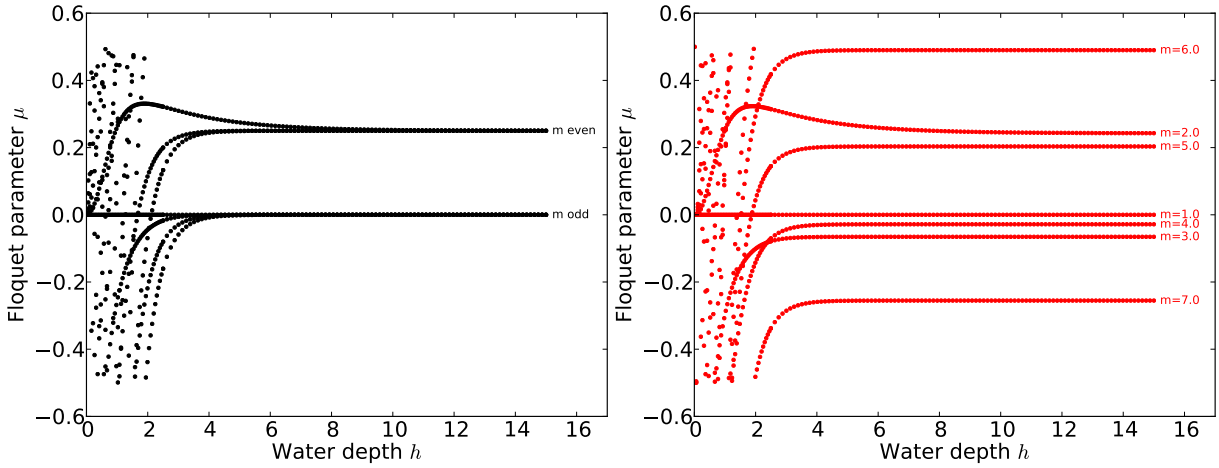

Figure 3.5: Values of the Floquet exponent μ for which the collision condition is met, as a function of depth h. As before, black curves (left) correspond to $\sigma = 0$, while curves in red (right) are for $\sigma = 1/90\pi$. Different curves are obtained for different values of m, as indicated. As h is increased, only two different values of μ for which small amplitude instabilities may exist are approached asymptotically when $\sigma = 0$: $\mu = 0$ and $\mu = 1/4$. With $\sigma = 1/(90\pi)$ this is not the case and small amplitude solutions are potentially unstable with respect to perturbations of many different periods.

This equation determines for which Floquet exponents μ (modulo 1) eigenvalues collide, depending on different parameters h, g, σ. Figure 3.5 displays values of μ for which (3.31) is satisfied, as a function of the depth h, for fixed g and σ ($\sigma = 0$ in black, and $\sigma = 1/(90\pi)$, in red). The different curves correspond to different values of m.

Figure 3.6 shows the positive imaginary part of the collision points (their real part is zero) as a function of the water depth for $\sigma = 0$ (left) and $\sigma = 1/(90\pi)$ (right). Table 3.1 compares such imaginary parts computed for different depths h with and without surface tension. One of the goals for examining the spectral stability of non-zero amplitude traveling wave profiles is to track whether the collided eigenvalues do result in instabilities, and if so, how these evolve for solutions of higher amplitude.

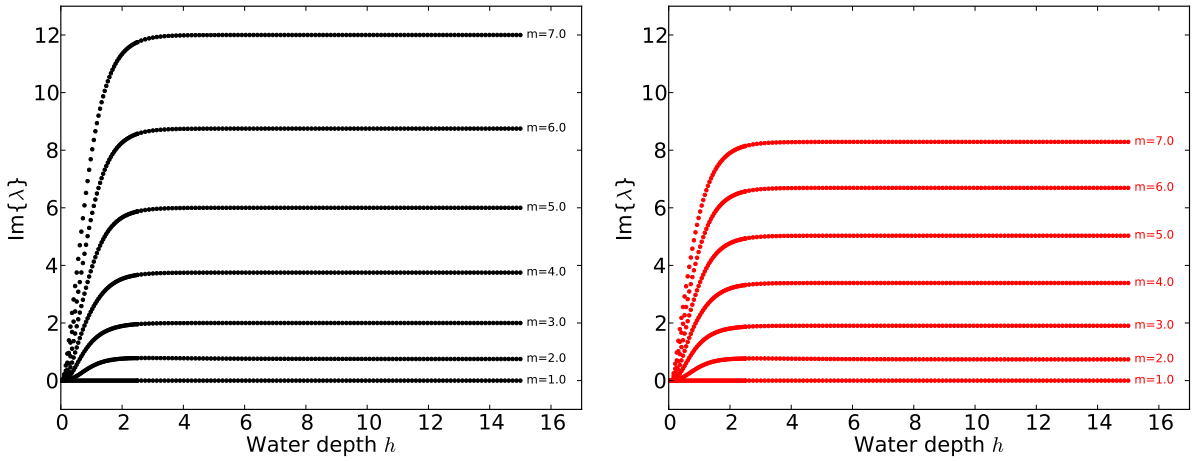

Figure 3.6: The imaginary part of the eigenvalues for which the collision condition is met as a function of depth h. On the left the case of gravity waves ($\sigma = 0$) is displayed. The case $\sigma = 1/(90\pi)$ is shown on the right. Different curves correspond to different values of m. Negative values would result in the mirror imagine of this figure below the horizontal axis.

3.4.3 Numerical Procedure

We proceed to solve the generalized eigenvalue problem (3.28) using the Floquet-Fourier-Hill method [23, 25] for a sufficient number of values of the Floquet exponent μ to ensure that all features of the spectrum are resolved. This is done in part by tracking (see below) the location of instabilities of solutions of smaller amplitude, as we continue up the solution branch. The collided eigenvalues (*i.e.*, the eigenvalues of higher multiplicity) of the flat water state are the starting point for this. As discussed below, we find that *all* periodic traveling water waves are spectrally unstable, irrespective of their amplitude and of the depth of the water. This result is not surprising for waves in deep water, where the presence of the Benjamin-Feir instability [7] is well known. Deconinck and Oliveras [25] computed bubbles of instability (*i.e.*, topological ovals of spectral elements across the imaginary axis, which emanate from the flat-water collided eigenvalues for small wave amplitude), but these bubbles are narrow and it was reasonable to hope that the inclusion of surface tension might prevent their formation, leading to spectrally stable wave profiles for at least some amplitude

	$h = 0.5$				$h = 1.5$				$h = \infty$			
	$\sigma = 0$		$\sigma = 1/90\pi$		$\sigma = 0$		$\sigma = 1/90\pi$		$\sigma = 0$		$\sigma = 1/90\pi$	
m	μ	Im$\{\lambda\}$	μ	Im$\{\lambda\}$	μ	Im$\{\lambda\}$	μ	Im$\{\lambda\}$	μ	Im$\{\lambda\}$	μ	Im$\{\lambda\}$
1	0	0	0	0	0	0	0	0	0	0	0	0
2	0.106	0.148	0.100	0.139	0.322	0.687	0.314	0.673	0.25	0.75	0.243	0.736
3	0.375	0.519	0.345	0.478	-0.108	1.730	-0.157	1.651	0	2	-0.065	1.904
4	-0.206	1.088	-0.292	0.973	-0.095	3.188	-0.316	2.900	0.25	3.75	-0.028	3.389

Table 3.1: This table gives the Floquet parameters μ for which we have an eigenvalue collision in the case of flat water. The approximate values shown here are for the test cases we consider in the numerical results section, presenting only those Floquet parameters for which the largest instabilities are expected.

and depth range. This is not the case. The goal of this and the following subsections is to demonstrate how surface tension affects the results of [25], while it cannot overcome the instabilities. For the three values of depth h in Figure 3.3, we examine the Floquet parameter μ for which instabilities are present, as well as the graph of the spectrum in the complex λ plane. We can do so along the entire solution branch in Figure 3.3. The figures include results only for the solution labeled with a square in Figure 3.3, roughly in the middle of the computed branch.

3.4.4 Bubble Tracking

It is interesting to note that the center of the bubbles of instability are not given by the collision values of Table 3.1. The locations of the bubbles move as we increase the amplitude of the traveling waves. We can track the movement of the center of the bubbles as well as of their width numerically, as shown in Figure 3.7. This was done for shallow water bubbles, since the bubbles are most important there. In Figure 3.7, we track the movement of the largest and second-largest bubble of instability, respectively. As usual, black curves correspond to $\sigma = 0$, red ones to $\sigma = 1/(90\pi)$. Lastly, the rightmost panel of Figure 3.7 shows the change in the size of the bubble *i.e.*, its associated instability growth rate) as a

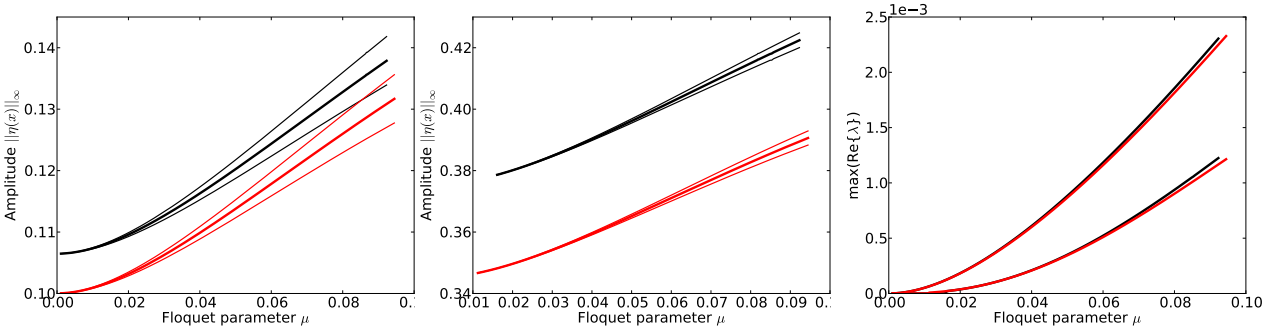

Figure 3.7: Tracking the bubble location and width as a function of solution amplitude, with curves in black for $\sigma = 0$, curves in red for $\sigma = 1/(90\pi)$. The left panel tracks the largest bubble, the middle panel the second largest. Their instability growth rates are shown on the right.

function of the solution amplitude, hence the largest bubble corresponds to the top curves, the second bubble to the bottom curves. The rapid movement of the bubbles presents a numerical difficulty that needs to be overcome with a careful choice of the Floquet exponents used in order to resolve all relevant features of the stability spectrum.

3.4.5 Stability Spectra

Figures 3.8-3.10 display the maximal real part of the spectral elements as a function of the Floquet parameter μ. Nonzero values correspond to instabilities. The results for shallow water ($h = 0.5$) are in Figure 3.8. They illustrate that the effect of surface tension is to shift the range of Floquet exponents for which instabilities occur, while barely affecting their growth rate. The zoom on the right shows that the numerical results are well resolved and that the sharp spikes on the left lie above a range of μ values for which instabilities are present. As the wave amplitude is decreased, the width of these ranges shrinks to zero, approaching one of the values of μ for which eigenvalues collide for the flat water state. Different instabilities are visible, with a wide variety of instability growth rates. Figure 3.9 shows the result for deep water ($h = 1.5$) and Figure 3.10 shows the result for infinitely deep water ($h = \infty$), where the results are dominated by the Benjamin-Feir instability, as in

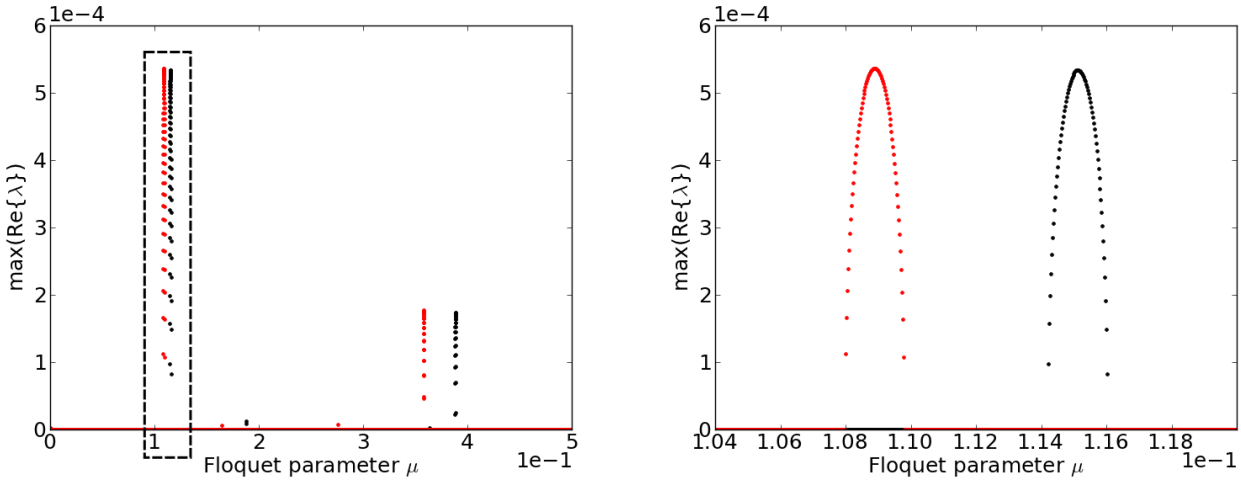

Figure 3.8: The maximal growth rate $\max \mathrm{Re}(\lambda)$ as a function of the Floquet exponent μ for $h = 0.5$ (shallow water). Throughout, black dots correspond to $\sigma = 0$, while red dots are for $\sigma = 1/(90\pi)$. Nonzero $\max \mathrm{Re}(\lambda)$ denote instabilities. The right panel is a zoom of the indicated region of the left panel.

[25]. Although the Benjamin-Feir instability is affected by the inclusion of surface tension, it appears to be affected much less than the bubbles, which are still present, but whose location may be shifted significantly.

In shallow water without surface tension, Deconinck and Oliveras [25] found the bubbles of instability shown in the first row of Figure 3.11. Two zooms of the complex λ plane shown on the left are shown there, demonstrating the absence of any instability at the origin (middle) and an enlargement of the bubble corresponding to the dominant instability (right). If surface tension is included, the results change as shown in the second row of Figure 3.11. The location of the bubbles changes, as remarked above. The largest real part is slightly increased, although this is hard to discern in Figure 3.11. The change in bubble location is a consequence of the change in eigenvalue collision location, displayed in Table 3.1. Importantly, more bubbles are visible with surface tension than without. This is illustrated in the second panel where two bubbles are shown to exist close to (but not at) the origin of the λ plane.

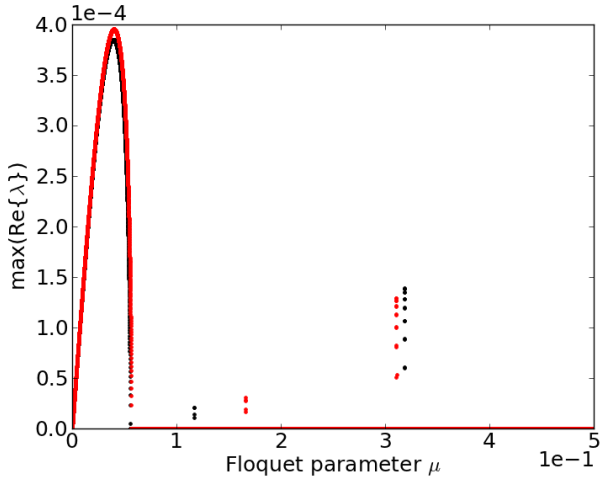

Figure 3.9: The maximal growth rate $\max \mathrm{Re}(\lambda)$ as a function of the Floquet exponent μ for $h = 1.5$ (deep water). Throughout, black dots correspond to $\sigma = 0$, while red dots are for $\sigma = 1/(90\pi)$. Nonzero $\max \mathrm{Re}(\lambda)$ denote instabilities.

For waves in deep water ($h > 1.363$) [6, 87] without surface tension, both the bubble instabilities as well as the Benjamin-Feir instability appear. In terms of the largest growth rate of the instabilities, the Benjamin-Feir instability dominates for $h > 1.4306$, see [25]. A representative result is shown in the top row of Figure 3.12. The results with surface tension included are shown in the bottom row. Once again, the growth rates are slightly higher with surface tension than without. This is more obvious in Figure 3.8. Zooming into the center of the complex plane clearly shows the figure eight characteristic of the Benjamin-Feir instability, both with and without surface tension. However, with surface tension, two other facets are apparent. Zooming in one more time to resolve the pattern seen at the center, we see a bubble of instability quite clearly for $\sigma = 1/(90\pi)$, absent for pure gravity waves. Another feature is the splitting of the Benjamin-Feir figure eight, away from the origin. This occurs for gravity waves as well, but it appears to happen for gravity-capillary waves for traveling waves of significantly lower amplitude.

Finally, the case of infinite depth is examined in Figure 3.13. As before, the results for pure gravity waves ($\sigma = 0$) are shown in the top row, those with $\sigma = 1/(90\pi)$ in the bottom

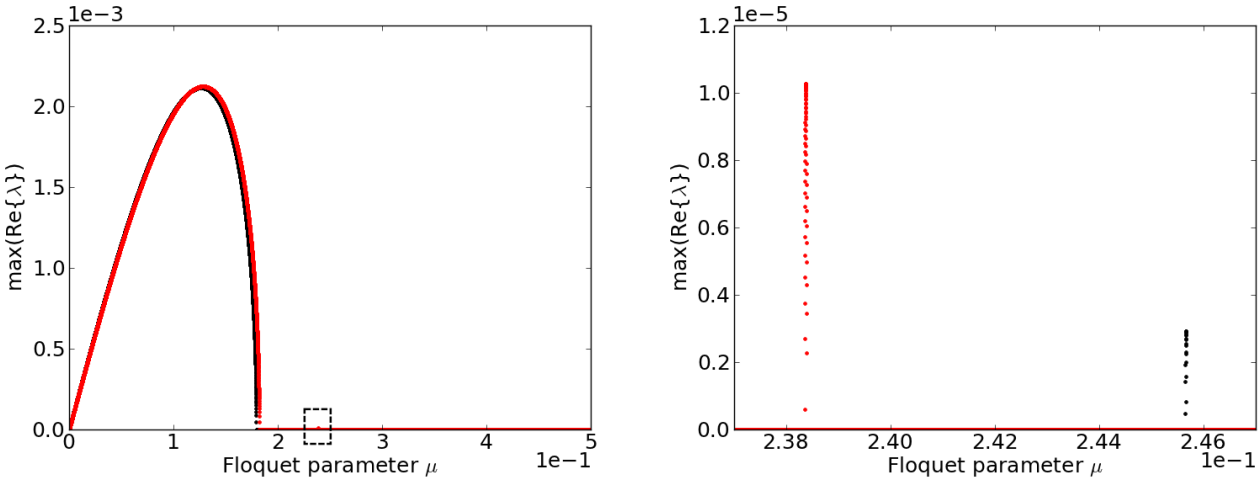

Figure 3.10: The maximal growth rate $\max \mathrm{Re}(\lambda)$ as a function of the Floquet exponent μ for $h = \infty$ (infinitely deep water). Throughout, black dots correspond to $\sigma = 0$, while red dots are for $\sigma = 1/(90\pi)$. The right panel is a zoom of the indicated region of the left panel.

row. Once again, the Benjamin-Feir instability and bubble instabilities are observed. The Benjamin-Feir instability is even more dominant than before, as shown in Figure 3.13. Both with and without surface tension, the bubbles can barely be seen. As for $h = 1.5$, zooming into the origin, shows that the Benjamin-Feir instability has split away from the origin for a traveling wave of this amplitude.

3.5 Conclusions

We have investigated the effect of small surface tension on the spectral stability of the one-dimensional evolution of periodic traveling water waves within the context of the classical Euler equations governing potential flow. First, we used numerical continuation to extend the results of [25] by computing traveling wave solutions of the Euler equations in the presence of surface tension. This was done using the water wave formulation of Ablowitz, Fokas, and Musslimani [1], and care was taken to avoid resonant or near-resonant waves.

With these solutions in hand, we numerically computed their stability spectrum using

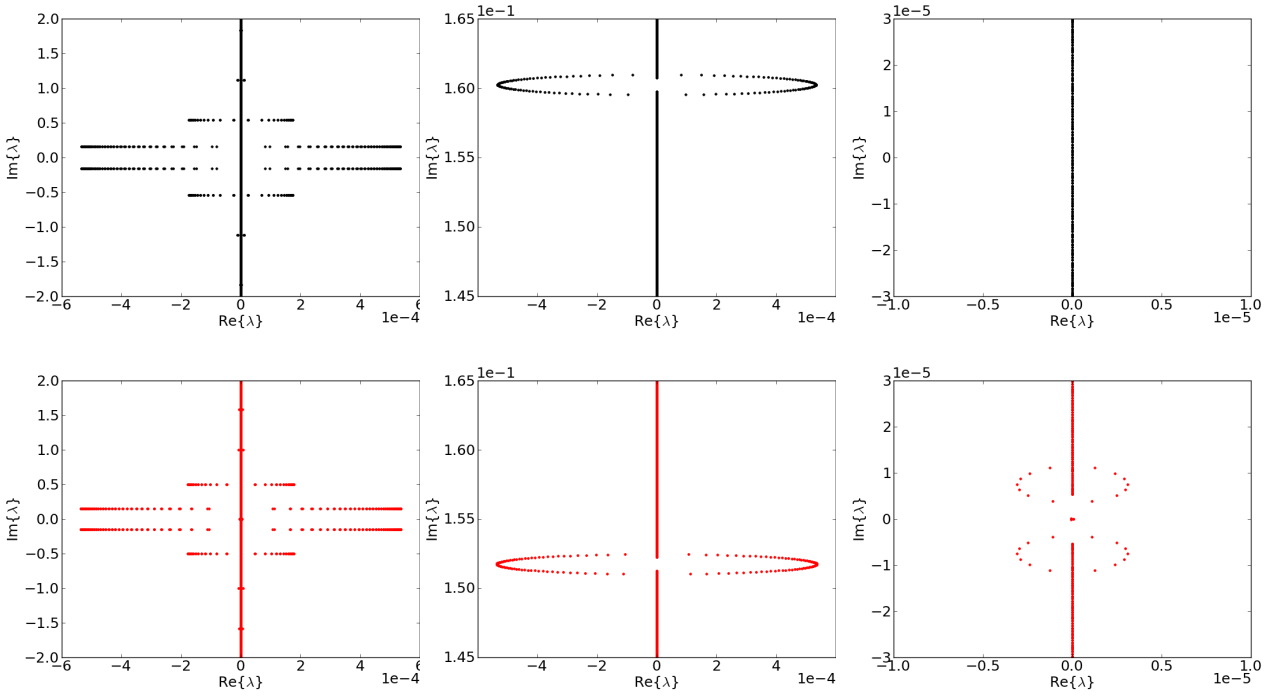

Figure 3.11: The complex λ plane for waves in shallow water (h=0.5), without (top) and with (bottom) surface tension. A discussion is presented in the main text.

the Floquet-Fourier-Hill method [23], ensuring that all relevant aspects of the spectrum were captured. To this end, we tracked the location of the bubbles of instability that originate from collided eigenvalues in the flat water state. We found that the inclusion of surface tension does not overcome the formation of the bubbles, so that all periodic traveling waves of the water wave problem are spectrally unstable. For pure gravity waves ($\sigma = 0$), this conclusion was already reached in [25], which focuses on the one-dimensional problem, and it can be inferred from restricting the two-dimensional studies of [68, 34] to one spatial dimension by allowing only one-dimensional perturbations. In fact, with surface tension, the growth rates observed are somewhat larger than those seen without. Our instability conclusion holds for both shallow and deep water. In shallow water, the bubbles appear to be the only mechanism for instability, while in deep water the Benjamin-Feir or modulational instability is typically dominant.

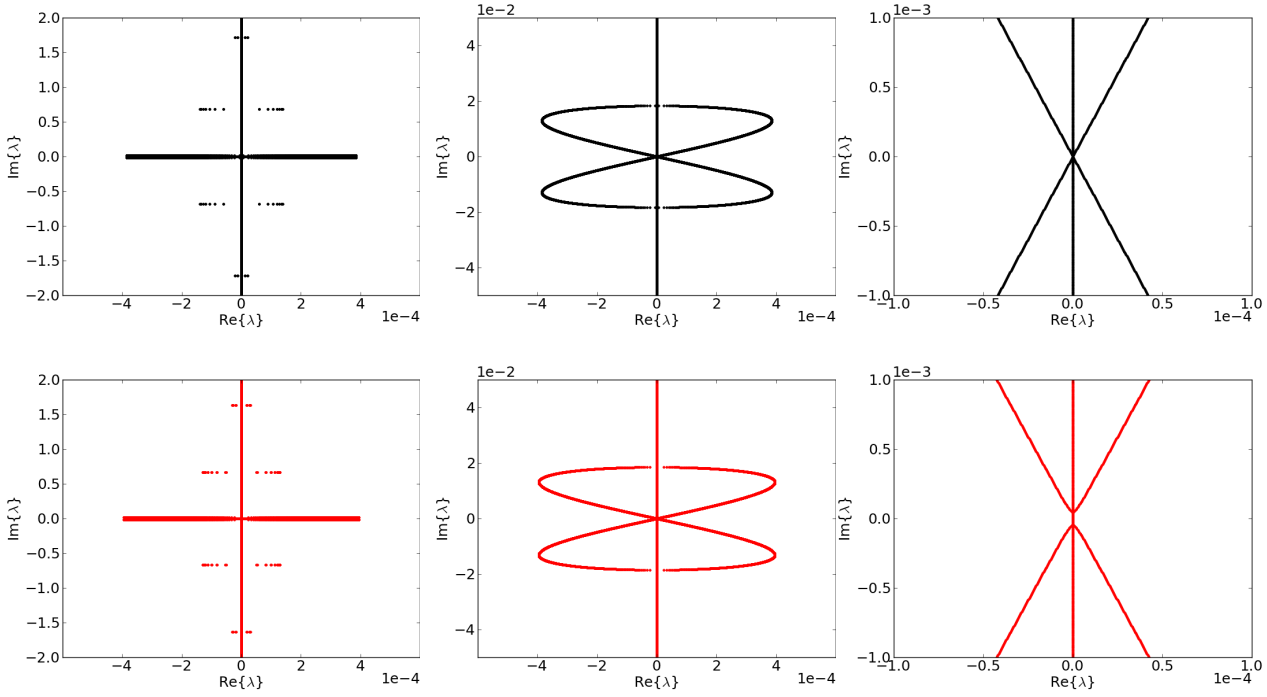

Figure 3.12: The complex λ plane for waves in deep water (h=1.5), without (top) and with (bottom) surface tension. A discussion is presented in the main text.

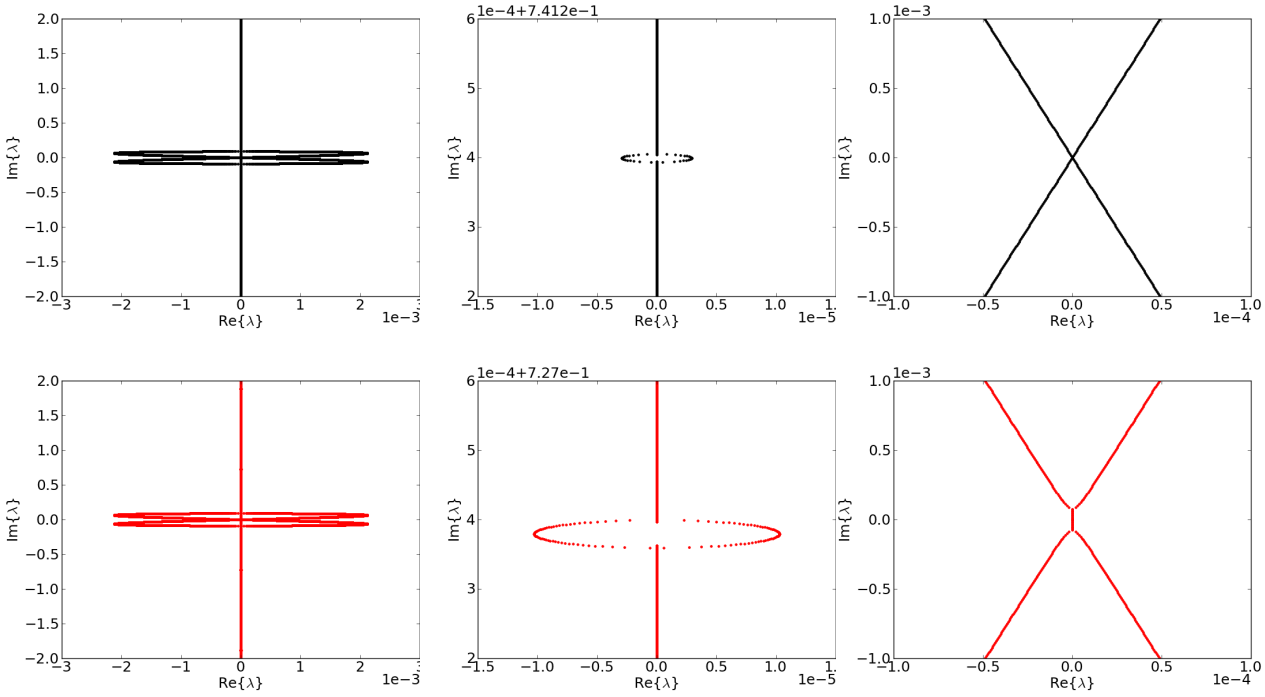

Figure 3.13: The complex eigenvalue plane showing bubble instabilities in water of infinite depth, $\sigma = 1/90\pi$ in red and $\sigma = 0$ in black.

Chapter 4

GRAVITY-CAPILLARY WAVES

4.1 Introduction

In this chapter, we present results from the paper "Instabilities of periodic gravity-capillary waves" by Trichtchenko, Deconinck and Wilkening, to be published. We are once again interested in finding the fully nonlinear solutions to Euler's equations and analyzing their spectral stability using Fourier-Floquet-Hill method [23]. We follow the work of Deconinck and Oliveras [25] as well as the work presented in the last chapter, but here we focus on the regime where forces of gravity and surface tension are almost equally important, *i.e.* gravity-capillary waves. We are mainly interested in solving Euler's equations in shallow water and therefore fix the water depth to be $h = 0.05$.

An important property of Euler's equations is the existence of resonant phenomena. It can be understood by considering a Stokes expansion [82] for the surface of the wave. Using regular perturbation theory, we expand the surface in terms of a small parameter ϵ representing the amplitude of the wave

$$\eta(x) = \sum_{n=1}^{\infty} \epsilon^n \eta_n. \tag{4.1}$$

From the work by Stokes [82] and convergence results by Levi-Civita [57] and Struik [83], we know we can also expand the wave profile in terms of a cosine series

$$\eta_n(x) = \sum_{m=1}^{n} \hat{\eta}_{nm} \cos(mx). \tag{4.2}$$

From this, we obtain a solvability condition for η_n with $m \in \mathbb{Z}$. If

$$(g+\sigma)\tanh(h) - \left(g + m^2\sigma\right)\frac{\tanh(mh)}{m} = 0 \tag{4.3}$$

does not hold, then we can solve for η_m. We call (4.3) the resonance condition. The coefficient of surface tension σ, determines the resonant harmonic $m \in \mathbb{Z}$. This was first noticed by Wilton [92]. Numerically, it is interesting to vary σ depending on which resonant mode we wish to capture. The relation between surface tension and resonant modes is shown in Figure 4.1. In this chapter, we examine what happens in the cases where we are near-resonance $k \neq \mathbb{Z}$ and in those where we are at resonance. However, this resonance condition is a weakly nonlinear theory result. This implies it is valid for small amplitude solutions. In

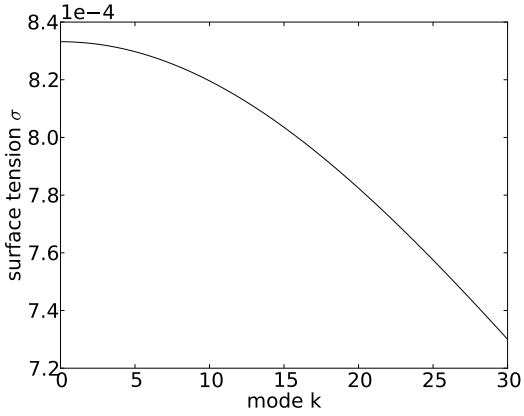

Figure 4.1: The relationship between surface tension σ and resonant modes k.

our work, we are interested in solutions of the fully nonlinear problem and thus, arbitrary amplitude waves.

Deconinck and Oliveras and the previous chapter present a thorough numerical overview of the spectral instabilities of periodic travelling one-dimensional gravity water waves and gravity waves with a small coefficient of surface tension. An emphasis of that work, is the presence of oscillatory instabilities even for waves in shallow water. Since the underlying waves are periodic, their stability analysis uses Hill's method [23], which incorporates the conclusions from Floquet's Theorem with Fourier analysis. This associates with each wave a range of Floquet exponents μ which may be taken as $(-\pi/L, \pi/L]$. The growth rates of the oscillatory instabilities are small, even for waves of moderate amplitude, and the range of Floquet exponents with which they are associated is narrow (on the order of 10^{-4} for $L = 2\pi$). Numerically, it is prohibitively expensive to consider an equally spaced set of μ values to capture these instabilities. Instead, more values of μ are considered near those values of the Floquet exponents where instabilities may arise, as predicted by MacKay and Saffman [62]. In that work, it was shown that both gravity as well as gravity waves with a small coefficient of surface tension, are unstable to high frequency perturbations.

It is well known that the incorporation of capillary effects leads to the presence of resonances in the Fourier representation of the periodic travelling water waves. If the

resonance condition (4.3) is satisfied, so-called Wilton ripples are found [86, 92]. This results in the presence of small denominators in the Stokes expansion of the wave profile. This is especially problematic for waves of moderate or high amplitude, whose accurate Fourier representation requires more modes. This is precisely the limit in which we work. However, in this limit, accuracy becomes very important. For the purposes of this work, we have used two different methods to compute accurate solutions. We use the quadruple precision results and examine their stability.

The layout of this chapter is as follows. The next section discusses the reformulation of the water wave problem we use and compares two different methods for computing solutions. We proceed by showing some sample solutions. Then we briefly describe the numerical method used to compute spectral stability. This is followed by numerical results of the stability calculations. We finish with conclusions and possible extensions to the project.

4.2 Solutions

We compute the solutions to Euler's equations numerically by using two methods. One method takes advantage of a reformulation by Ablowitz, Fokas and Musslimani [1]. The second method makes use of Dirichlet to Neumann operators [17]. Since the first method was described in the previous chapter, we focus on briefly outlining the second method.

4.2.1 Boundary Integral Method

The second method used to compute the solutions to Euler's equations is based on a method by Wilkening for the time periodic problem [91], but modified for the spatially periodic problem. As before, we switch into a travelling frame of reference moving at speed c and look at the stationary problem. If we only consider the equations at the surface for which $q(x,t) = c\phi(x,\eta(x,t),t)$ where we also rescaled the velocity potential, then

$$\begin{cases} \eta = \eta_x q_x - q_z, \\ c^2 q = c^2 \phi_z \eta + c^2 \dfrac{1}{2}\left(\phi_x^2 + \phi_z^2\right) + g\eta - \sigma \dfrac{\eta_{xx}}{(1+\eta_x^2)^{3/2}}. \end{cases} \tag{4.4}$$

As written, we have a system of two equations and two unknown surface variables $q(x)$ and $\eta(x)$. We can solve the first equation by making using of the inverse of the Dirichlet to

Neumann operator $G(\eta)$ [17]. If we rewrite the first equation as

$$q = -G^{-1}(\eta)\eta_x, \tag{4.5}$$

then we can use the method introduced by Wilkening in [91] as was done in the time periodic problem, except in this case applying the inverse to map the Neumann data to Dirichlet data. The second equation is solved via the modified Levenberg-Marquardt method [91], where we use it as an objective function in the case of spatially periodic waves with zero mean (represented by $P[\cdot]$) as given by

$$aq = P\left[a\phi_z\eta + a\frac{1}{2}\left(\phi_x^2 + \phi_z^2\right) + g\eta - \sigma\frac{\eta_{xx}}{\left(1+\eta_x^2\right)^{3/2}}\right], \tag{4.6}$$

with $a = c^2$. The velocity potential ϕ is computed by solving Laplace's equations for the bulk of the fluid. The solutions shown in Figure 4.6 were computed on a laptop using compiled C code. We use as many Fourier modes as needed to make sure the highest modes stay at machine precision. These numerical results are different from gravity waves with a small coefficient of surface tension as seen in [26] because they no longer show a monotonic decay of Fourier modes. The solutions computed here, show resonant modes governed by the value of surface tension. This will be discussed in more detail later.

4.2.2 Discussion of Numerical Methods

The reason we use the boundary integral method, as implemented by Wilkening for this problem, is that the gravity-capillary solutions are very sensitive to numerical accuracy. The algorithm for the boundary integral method as well as its supplemental routines is implemented in quadruple precision in C. We can see the results for double and quadruple precision calculations in Figure 4.2. The different colours in the figure represent solutions for different amplitudes in Fourier space. It can be seen that in the highlighted region for the double precision calculations on the left, the first few iterations over-estimate the amplitude of the resonant coefficient. It shows that the 20th Fourier mode at first decays and then grows. In the quadruple precision case on the right, as we increase wave amplitude, the Fourier modes show only growth for these small amplitude solutions. For the purposes of

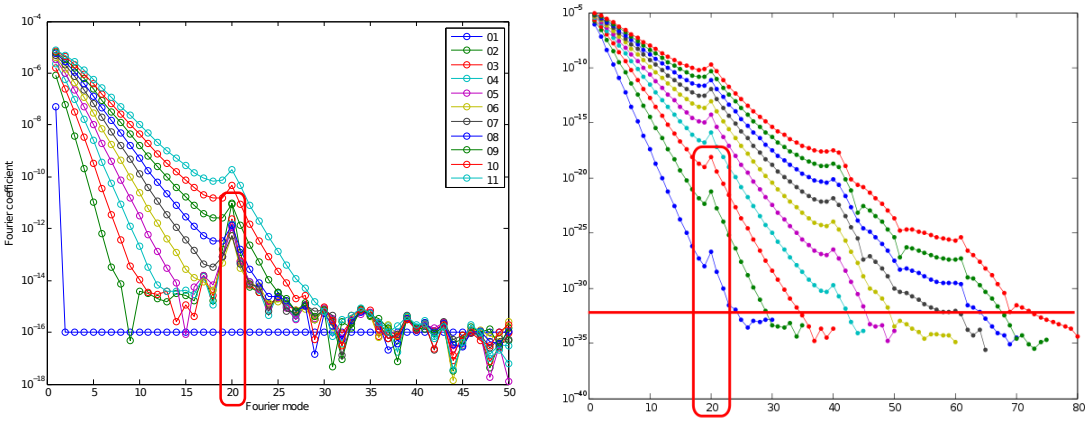

Figure 4.2: Comparison of double (left) and quadruple precision (right) calculations of different amplitude solutions in Fourier space. The x-axis represents the Fourier mode and the y-axis is the amplitude of that Fourier coefficient plotted on a semi-log scale. On the left, it can be seen that the 20th Fourier mode for the small amplitude solutions is initially overestimated.

our work, since our computation of the spectral stability problem are double precision, we show the modes that are higher than 10^{-16}, but we use these higher precision solutions.

4.3 Numerical Results for the Solutions

We begin by first presenting the bifurcation branch of solutions for different coefficients of surface tension, examining how gravity-capillary waves look when the balance between the two forces is varied. The bifurcation branches for different values of surface tension is seen in Figure 4.3. Noting the relation between the resonant mode and surface tension as seen in Figure 4.1 and that the smaller the resonant mode, the smaller the parameter of surface tension, we have labelled the curves according to their resonant modes. We can see that as we decrease the strength of surface tension, the directions of the bifurcation branches change.

We present the wave profiles for the coefficients of surface tension shown in Figure 4.3 in Figure 4.4 and Figure 4.5. These profiles are for the waves at the top of each bifurcation branch. On the left we present the wave profile in physical space and on the right, its Fourier coefficients on a semi-log scale. In Figure 4.4, we see that the main wave profile has a few

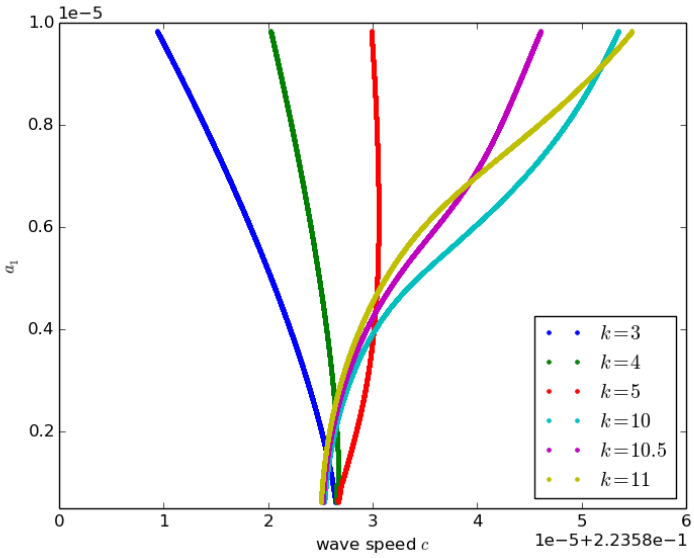

Figure 4.3: Multiple bifurcation branches for different coefficients of surface tension. The y-axis shows the first Fourier coefficient of the wave which is used as a continuation parameter and the x-axis is the speed of the wave.

small dimples and that the trough gets lower as we increase amplitude. This is indicative of a wave where surface tension has a strong effect. The coefficient of surface tension is 8.319×10^{-4}, 8.310×10^{-4} and 8.297×10^{-4} (from top to bottom) with resonant modes at $k = 3$, $k = 4$ and $k = 5$. Figure 4.5 shows wave profiles and their Fourier modes for waves where the dominant force is gravity. As in the case of a small coefficient of surface tension presented in the previous chapter, these waves have a shallow trough and steep crests. The top plot is for resonance at $k = 10$, the middle is for $k = 10.5$ and the bottom is for $k = 11$. We can see from the semi-log plots of the Fourier coefficients, that not only the resonant modes are present, but also their harmonics. Finally, in Figure 4.6, we fix the coefficient of surface tension so the 10th mode is resonant and we plot the wave profiles at three points on the bifurcation branch.

It is interesting to examine how individual Fourier modes grow as the amplitude of the wave increases. This is shown in Figure 4.7, Figure 4.8 and Figure 4.9. In these figures,

we plot the first 3 modes in the top row, the very center plot is always the resonant mode with the neighbouring modes to each side, the bottom row shows what happens to the harmonic as well as its neighbouring modes. The general trend is that the higher Fourier modes are of smaller amplitude than the mode we use as the continuation parameter, a_1. In Figure 4.6, we looked only at the logarithm of the absolute value of the coefficients. Here, we actually see these coefficients oscillate between positive and negative values as the amplitude is increased.

4.4 Stability

As presented in the last chapter, we use the Fourier-Floquet-Hill method to examine the stability of the solutions presented. Let the previously computed solution be $\eta_0(x)$ and $\eta_1(x)$ perturbations of a different period, then

$$\eta(x,t) = \eta_0(x) + \epsilon\eta_1(x)e^{\lambda t} + \dots. \tag{4.7}$$

Further, we apply Floquet decomposition, introduce a Floquet parameter μ and then apply the Fourier decomposition

$$\eta_1 = \sum_{m=-\infty}^{\infty} \hat{N}_m e^{i(m+\mu)x}. \tag{4.8}$$

After some manipulations and truncation of Fourier modes, we obtain a generalized eigenvalue problem. For details on the matrix entries, see the previous chapter. Since the problem is Hamiltonian, whenever $\mathbb{R}\{\lambda\} \neq 0$, this implies the solution is unstable. We can compute the eigenvalues for flat water explicitly

$$\lambda^{\pm}_{\mu+m} = ic(\mu+m) \pm i\sqrt{[g(\mu+m) + \sigma(\mu+m)^3]\tanh((\mu+m)h)}. \tag{4.9}$$

and conclude that flat water is spectrally stable. Eigenvalues are continuous with respect to the wave amplitude and therefore as amplitude increases they may develop a non-zero real part. Thus, a necessary condition for loss of stability is

$$\lambda^{\pm}_{\mu} = \lambda^{\pm}_{\mu+m}. \tag{4.10}$$

Some sample stability results are shown in Figure 4.12. The two new observed phenomena are the bubble at the center and the presence of double bubbles. The bubble around the center can be explained by noting that if $\mu = 0$, i.e. the perturbations are of the same period as the solution, $\lambda_0^{\pm} = 0$, the collision condition becomes

$$\lambda_m^{\pm} = icm \pm i\sqrt{[gm + \sigma m^3]\tanh(mh)} = 0. \tag{4.11}$$

Solving for σ using λ_m^+, we obtain resonance condition again

$$\sigma = \frac{g}{m}\left(\frac{\tanh(mh) - m\tanh(h)}{\tanh(h) - m\tanh(mh)}\right). \tag{4.12}$$

The presence of the double bubble is postulated to be a consequence of the fact that for 2π periodic waves, the bifurcation branch of nontrivial solutions starts at

$$c = \sqrt{(g + \sigma)\tanh(h)}. \tag{4.13}$$

The resonance condition (4.3) for a Wilton ripple to occur at $k = 10$ and thus a fixed σ also gives that

$$c = \sqrt{(g + (10^2)\sigma)\tanh(10h)}. \tag{4.14}$$

4.4.1 Convergence

Computation of stability spectra can be an expensive calculation. To make sure to capture instabilities, we need to sample a lot of Floquet parameters. For the purposes of our work, we sampled 2000 values, with $\mu \in [0, 0.5)$. The main goal was to see if gravity-capillary waves were unstable, and we saw instabilities in all the solutions we examined. Since we have to truncate the number of Fourier modes of the perturbation in (4.8), we examined the convergence as it depends on the number of those modes. Figure 4.10 shows a plot of the maximum instability with respect to the Floquet parameter where it is found. The results for 16-36 modes lie on top of each other and are indistinguishable by eye. However, we can see that when there are not enough Fourier modes of the perturbation, there are relatively large differences in the results for the types of instabilities observed. We used the Cauchy error to measure the difference between results at successive numbers of Fourier modes. As Figure 4.11 shows, at 24 modes, the results changes only by 10^{-14}. We use either 24 or 32 modes to compute our stability results.

4.5 Stability Results

There are a lot of different parameters to explore. We can examine the stability as we change the coefficient of surface tension as well as wave amplitude, for different Floquet parameters. Keeping surface tension fixed such that the resonant mode is at $k = 10$ and varying wave amplitude, the results are shown in Figure 4.12. As seen in [25] and [26], we have bubble instabilities. However, for a larger amplitude solution, we also start to see the presence of a bubble around the origin. For an even larger amplitude, we see the appearance of a double bubble. This is consistent with a value of surface tension for a resonance at $k = 10.5$ as well as $k = 11$ in Figure 4.13 and Figures 4.14. However, in Figure 4.14, the last row presents a zoom of the center region, which is where the double bubbles appear, and which is also of a different shape than we have observed in previous results.

It is also interesting to look at the eigenfunctions corresponding to the largest instabilities shown in Figures 4.15- 4.16. First, we plot the eigenfunctions corresponding to the eigenvalues with the largest real part for each Floquet parameter μ as shown on the left of Figures 4.15- 4.16. Then we plot the eigenfunction given by (4.8) for the largest, positive eigenvalue in the complex plane, with its real part on the x-axis and imaginary part on the y-axis as shown on the right of Figures 4.15 and Figure 4.16. We see the frequently visited parts of the complex eigenvalue plane from these plots. Also, we can get an idea of the periodicity of the eigenfunction. This is based on the denominator of the Floquet parameter, which can be a very large number in some cases. This can be done by comparing Figures 4.16 and 4.17. We can identify the shape seen in Figure 4.17 as an eigenfunction with Floquet parameter $\mu = 1/5 = 0.2$ and $\mu = 1/2 = 0.5$ respectively and we see these shapes repeated in Figure 4.16. Further, Figures 4.18 - 4.24 show how the full solution to the linearized water wave problem evolves according to

$$\eta(x,t) = \eta_0(x) + \epsilon e^{\lambda t} \sum_{m=-N}^{N} \hat{N}_m e^{i(m+\mu)x} + c.c., \tag{4.15}$$

where N represent the number of Fourier modes of the perturbation that we keep. In the present work, we keep ϵ to be $0.1a_1$, *i.e.* 10% of the first Fourier coefficient of the solution. Note that the complex conjugate represented by *c.c.* in (4.15) involves 4 terms because in a

Hamiltonian problem, the eigenvalues come in quadruplets unless they lie on the real axis. In that case, we need just 2 terms to preserve the Hamiltonian nature of the problem.

4.6 Conclusion

Using the same type of numerical techniques as in [25], [26] and [91], numerical solutions and stability of those solutions is computed. The computation of the fully nonlinear solutions in the regime of Wilton ripples is new, as is the analysis of their spectral stability. The new features in the complex eigenvalue plane that we see which were not present in gravity waves with small surface tension, are the double bubbles and the instability around the origin of the complex eigenvalue plane. We also see that these newly computed solutions are unstable to more Floquet parameters. By evolving the solution with the added perturbation, we see that the original wave profile gets overtaken by these perturbations.

There are still more avenues to explore. It would be interesting to further observe the growth of these instabilities as we vary the amplitude as well as the movement of these bubbles with respect to the Floquet parameter. However, this is computationally challenging. Preliminary results show that in cases examined in the previous chapter, the growth of these instabilities increases monotonically. Here we see that the growth rates are not monotonic, leading to more stable solutions for certain wave amplitudes. This seems to correspond to the solutions that have a more well-ordered Fourier representation. Finally, it would be interesting to push the accuracy of these methods to see if there is a maximal wave amplitude.

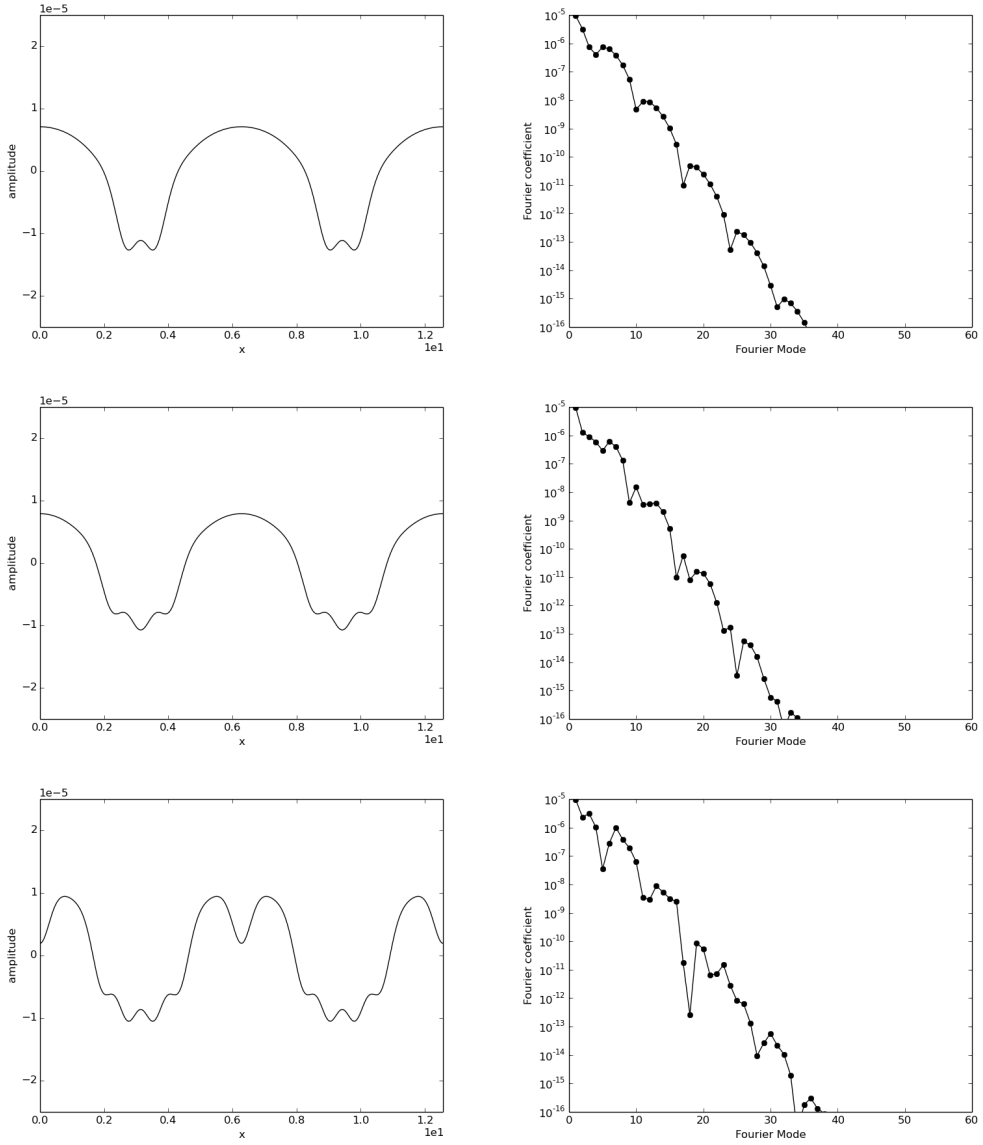

Figure 4.4: Wave profiles (left) and corresponding coefficients in Fourier space (right) for waves where surface tension is the dominating force. We see that the main wave profile has a few small dimples and that the trough gets lower for larger amplitude waves. The coefficient of surface tension is 8.319×10^{-4}, 8.310×10^{-4} and 8.297×10^{-4} (from top to bottom) with resonant modes being at $k = 3$, $k = 4$ and $k = 5$.

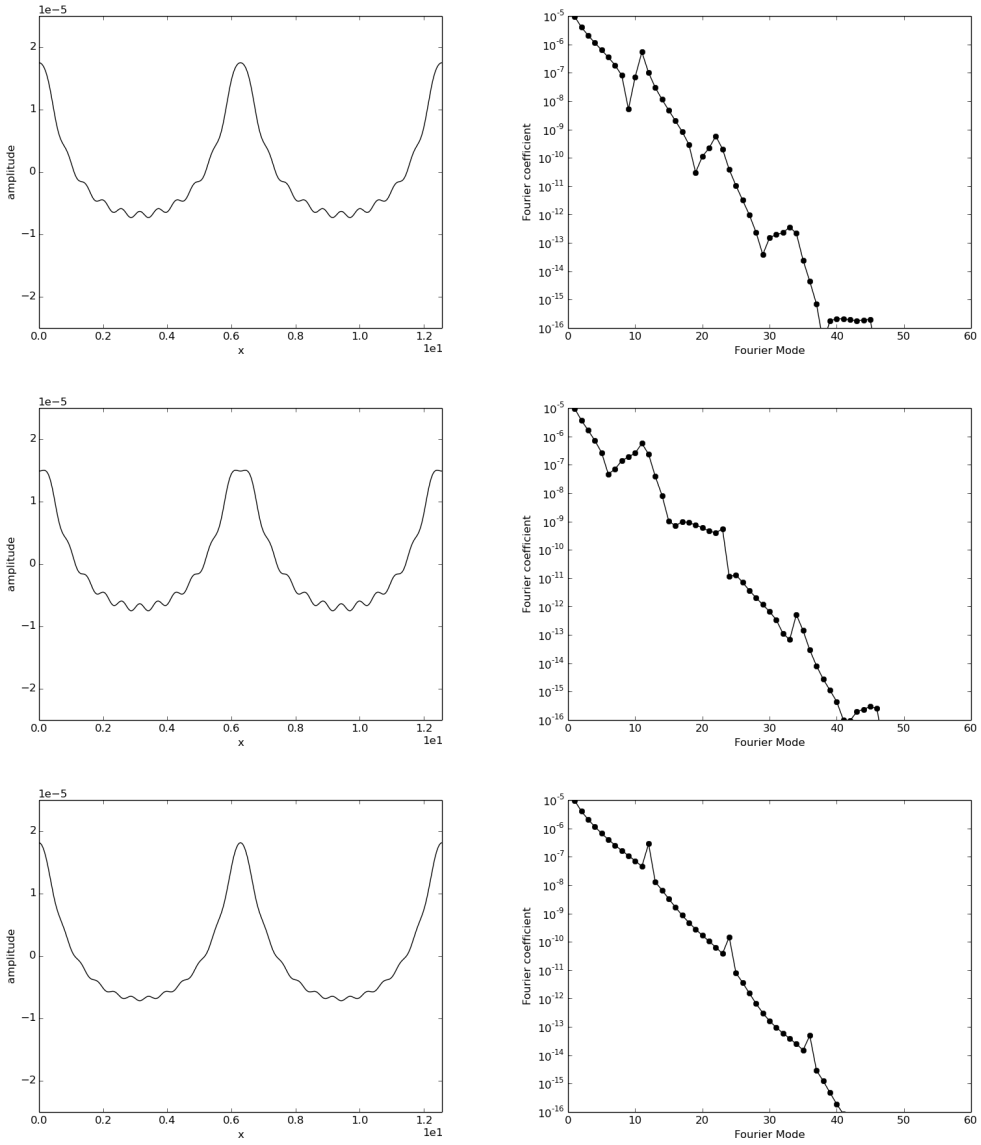

Figure 4.5: Wave profiles (left) and corresponding coefficients in Fourier space (right) for waves where gravity is the dominating force. We see that the main wave profile has a few small dimples and that the trough gets lower with increase in amplitude. The coefficient of surface tension is 8.319×10^{-4}, 8.310×10^{-4} and 8.297×10^{-4} (from top to bottom) with resonant modes being at $k = 10$, $k = 10.5$ and $k = 11$.

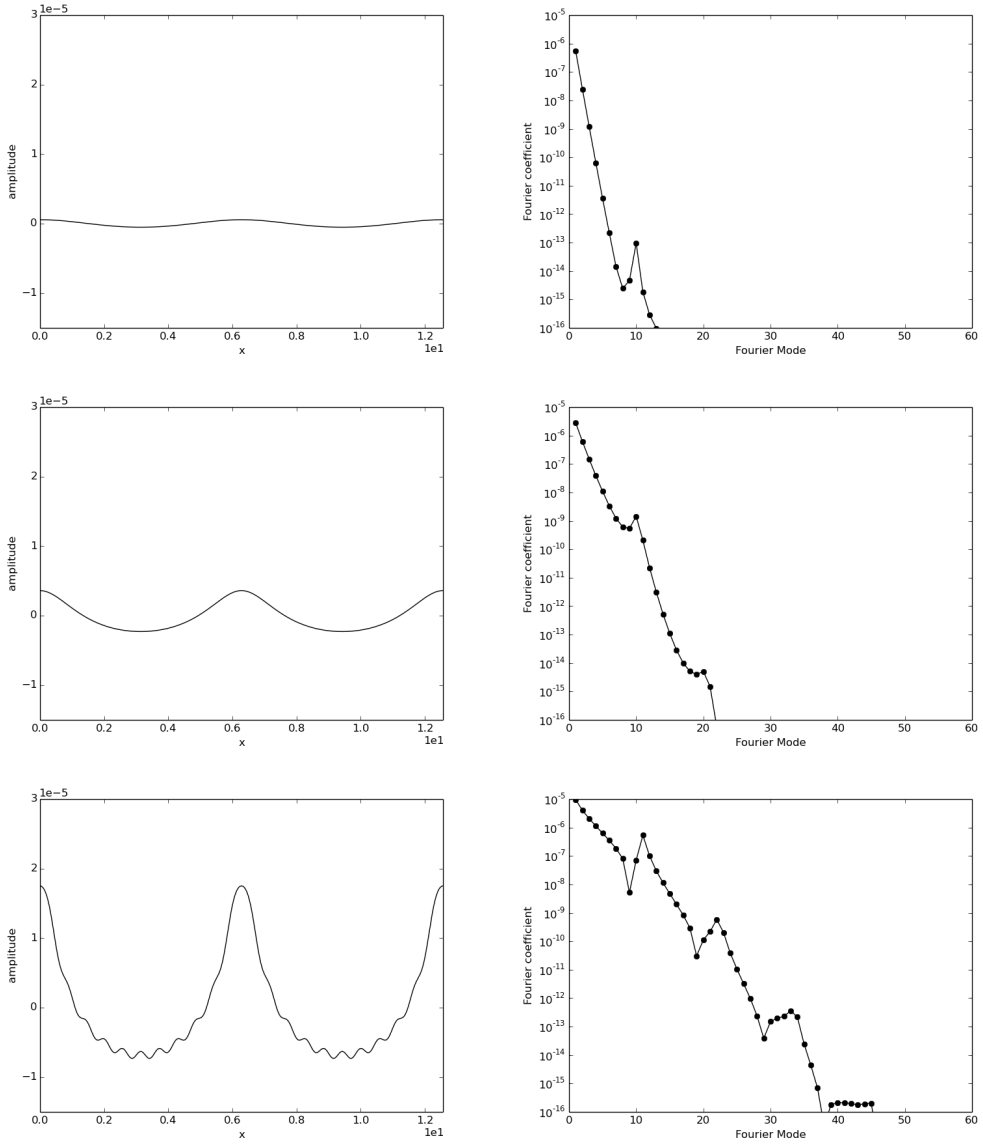

Figure 4.6: Wave profiles for different amplitude solutions (left) and the semi-log plot in Fourier space (right) for a parameter of surface tension such that resonance is at $k = 10$ ($\sigma = 8.196 \times 10^{-4}$).

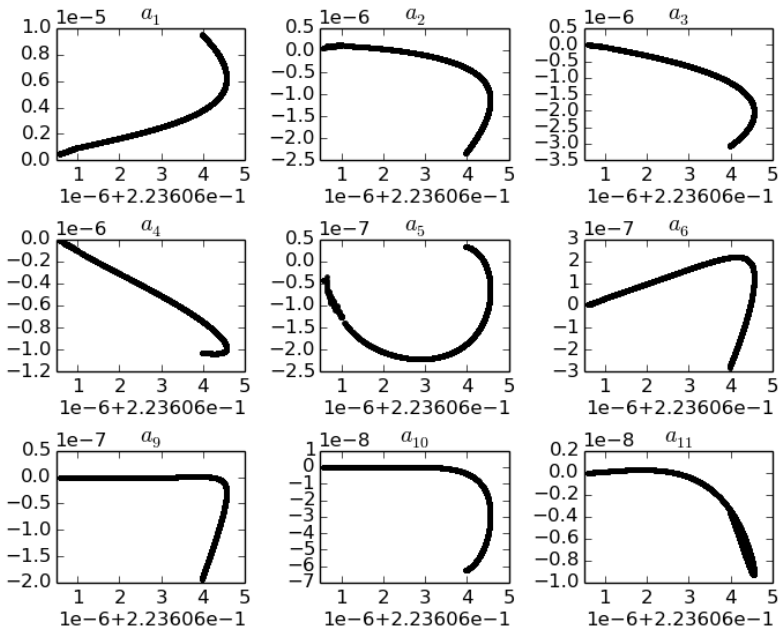

Figure 4.7: We examine several modes as the wave amplitude is increased for a coefficient of surface tension such that the resonant mode is the 5th one. We see that not only does the resonant mode grow, but so do its harmonics.

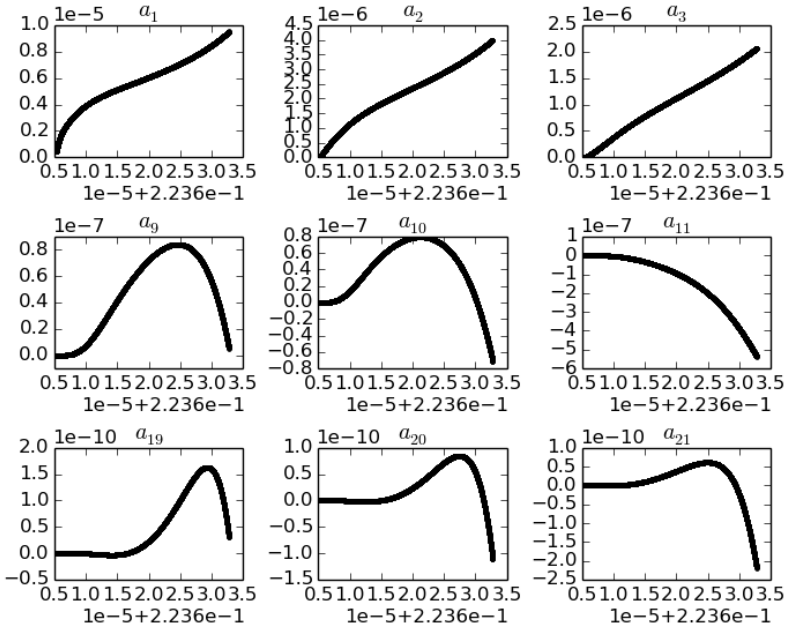

Figure 4.8: We examine several modes as the wave amplitude is increased for a coefficient of surface tension such that the resonant mode is the 10th one. We see that not only does the resonant mode grow, but so do its harmonics.

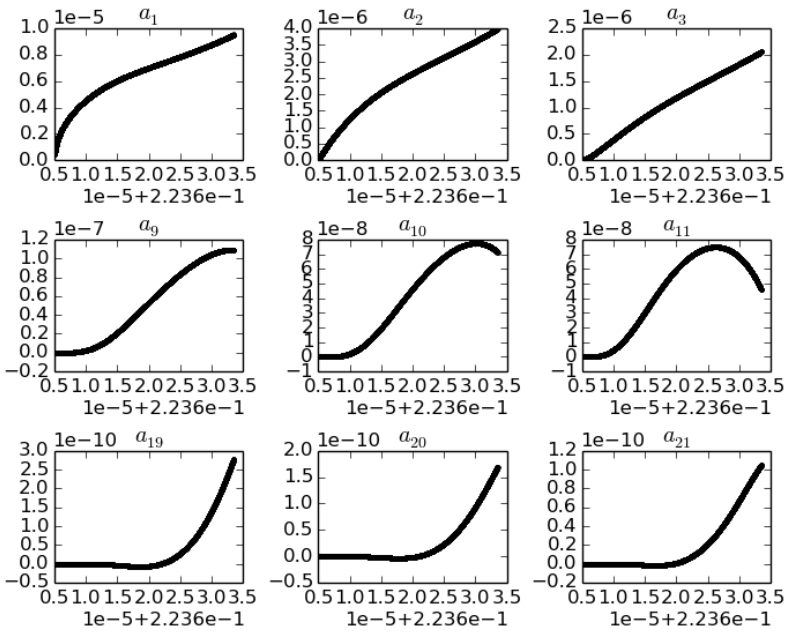

Figure 4.9: We examine several modes as the wave amplitude is increased for a coefficient of surface tension such that the resonant mode is the 11th one. We see that not only does the resonant mode grow, but also its harmonics.

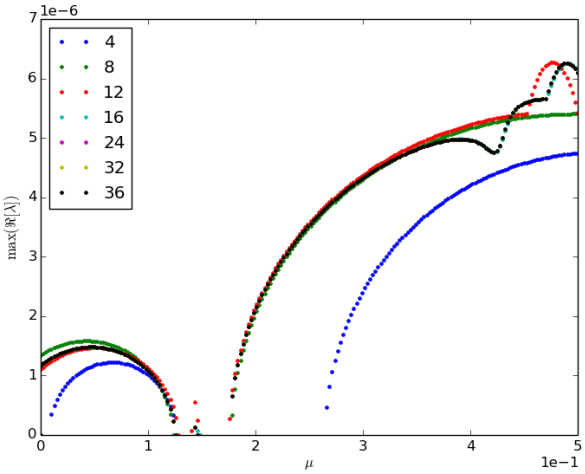

Figure 4.10: Results obtained when using a different number of Fourier modes to obtain the stability spectrum. Here we plot the maximum unstable eigenvalue with respect to the Floquet parameter and we observe that using 24, 32 and 36 modes visibly gives the same result. In other cases, the Floquet parameter with the most unstable eigenvalues changes.

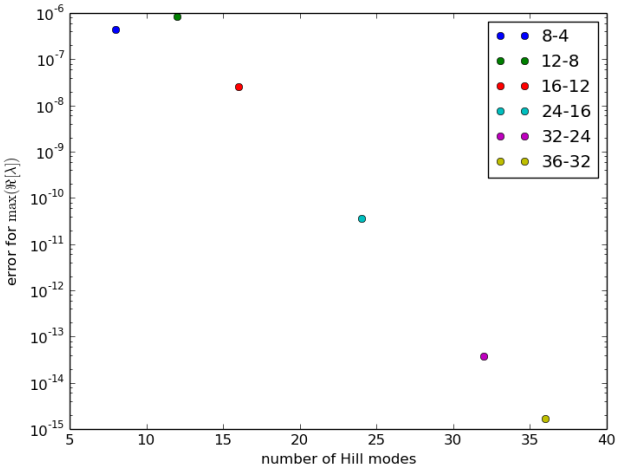

Figure 4.11: Results obtained when using a different number of Fourier modes to obtain the stability spectrum. Here we plot the log of the Cauchy error and see that increasing the accuracy from 24 to 32 modes, we only have an error of 10^{-14}.

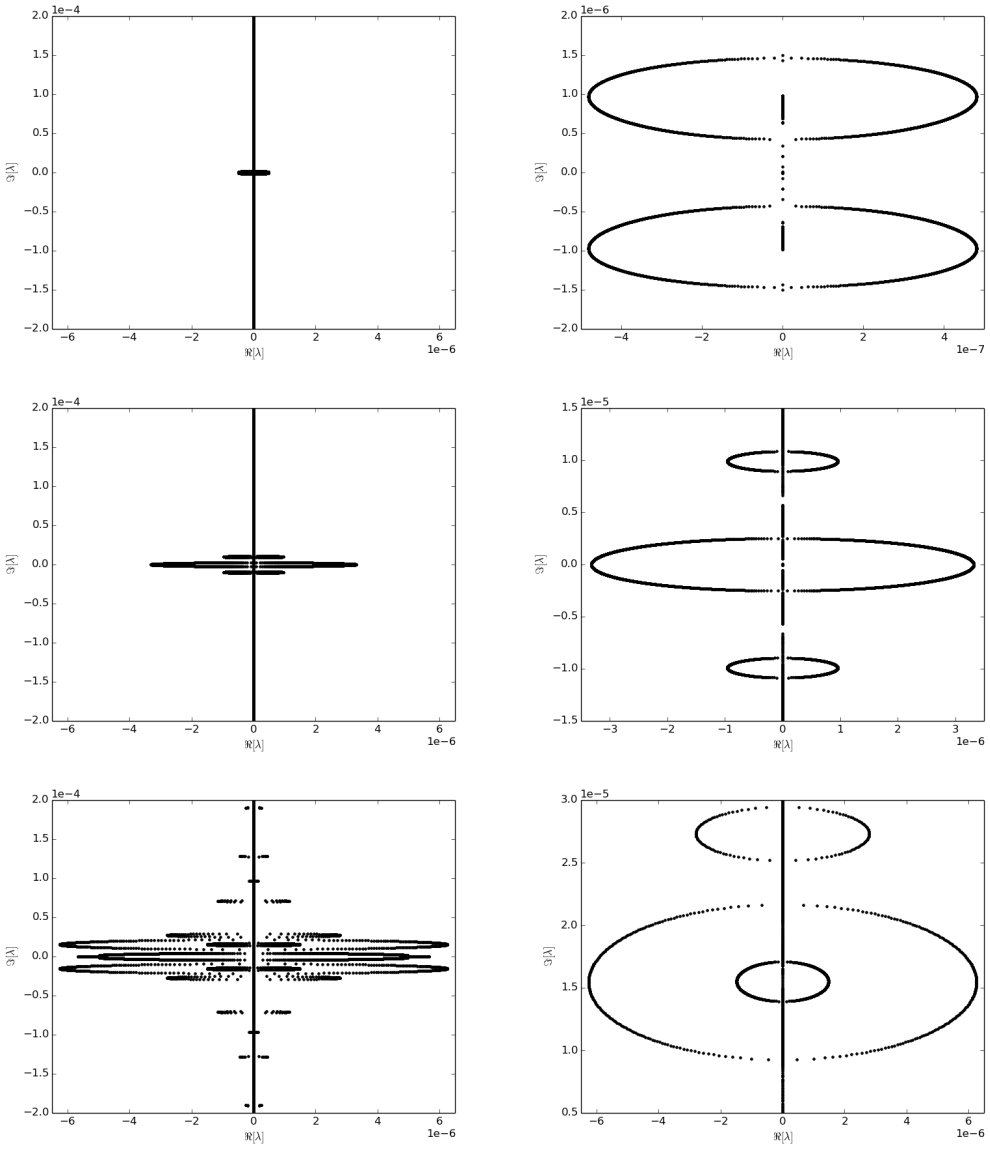

Figure 4.12: Some stability results for the solutions with the parameter of surface tension such that resonance occurs in the 10th mode shown in Figure 4.6. Amplitude of the solution analyzed increases top to bottom. The left column shows a fixed window in the complex eigenvalue plane and the right shows a zoom as indicated by the scales on the axes.

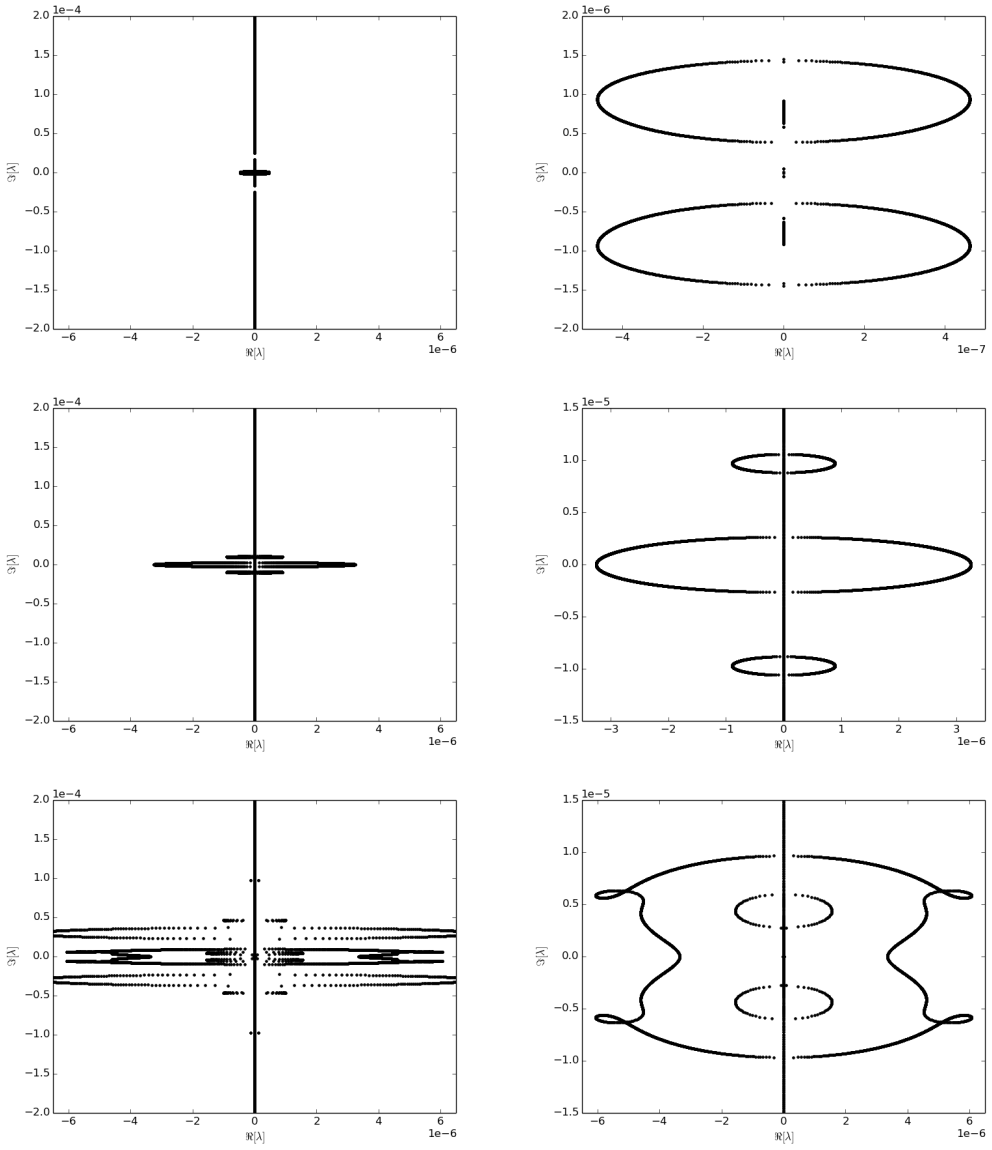

Figure 4.13: Some stability results for the solutions shown in Figure 4.5 with the parameter of surface tension such that resonance occurs at $k = 10.5$. The amplitude of the solution analyzed increases top to bottom. The left column shows a fixed window in the complex eigenvalue plane and the right shows a zoom as indicated by the scales on the axes.

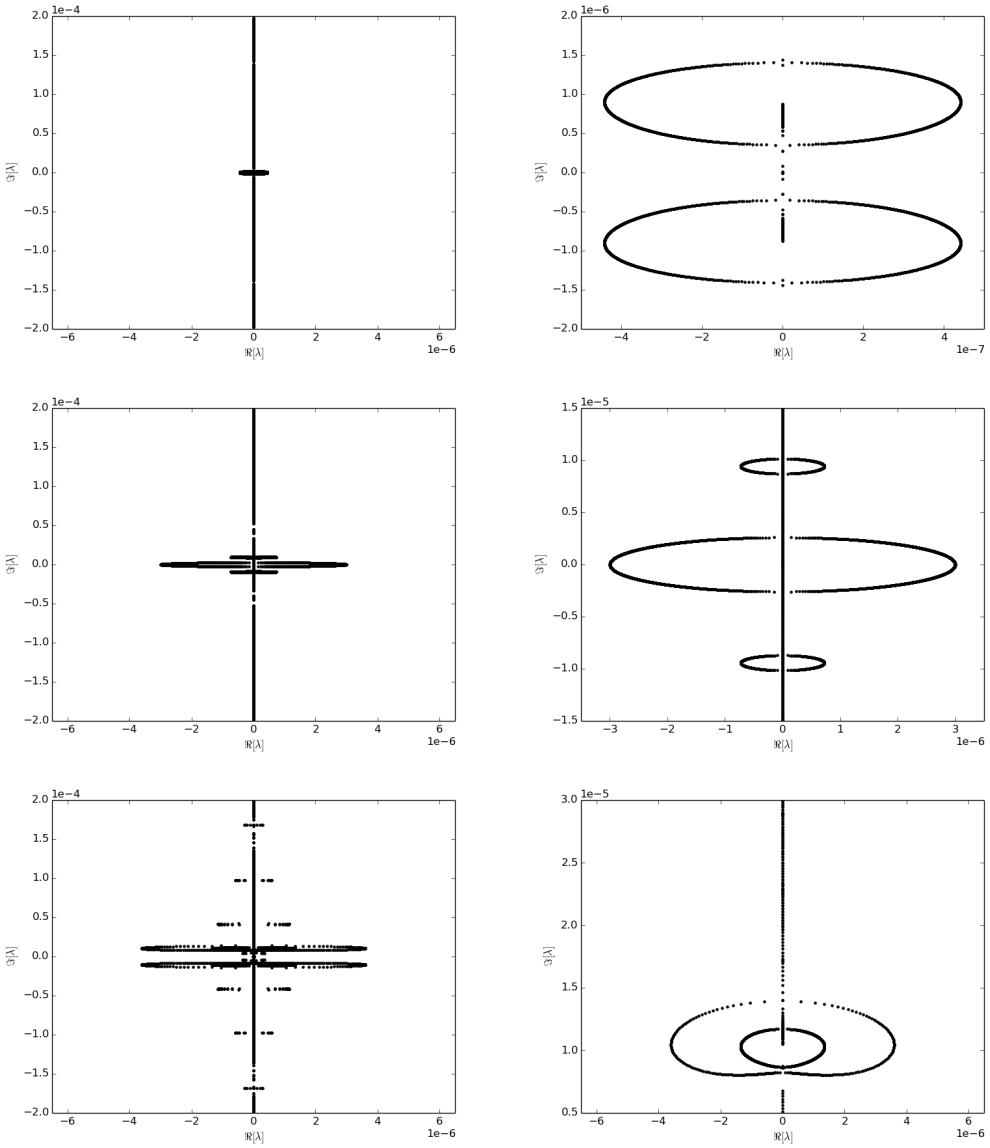

Figure 4.14: Some stability results for the solutions shown in Figure 4.5 with the parameter of surface tension such that resonance occurs at $k = 11$. The amplitude of the solution analyzed increases top to bottom. The left column shows a fixed window in the complex eigenvalue plane and the right shows a zoom as indicated by the scales on the axes.

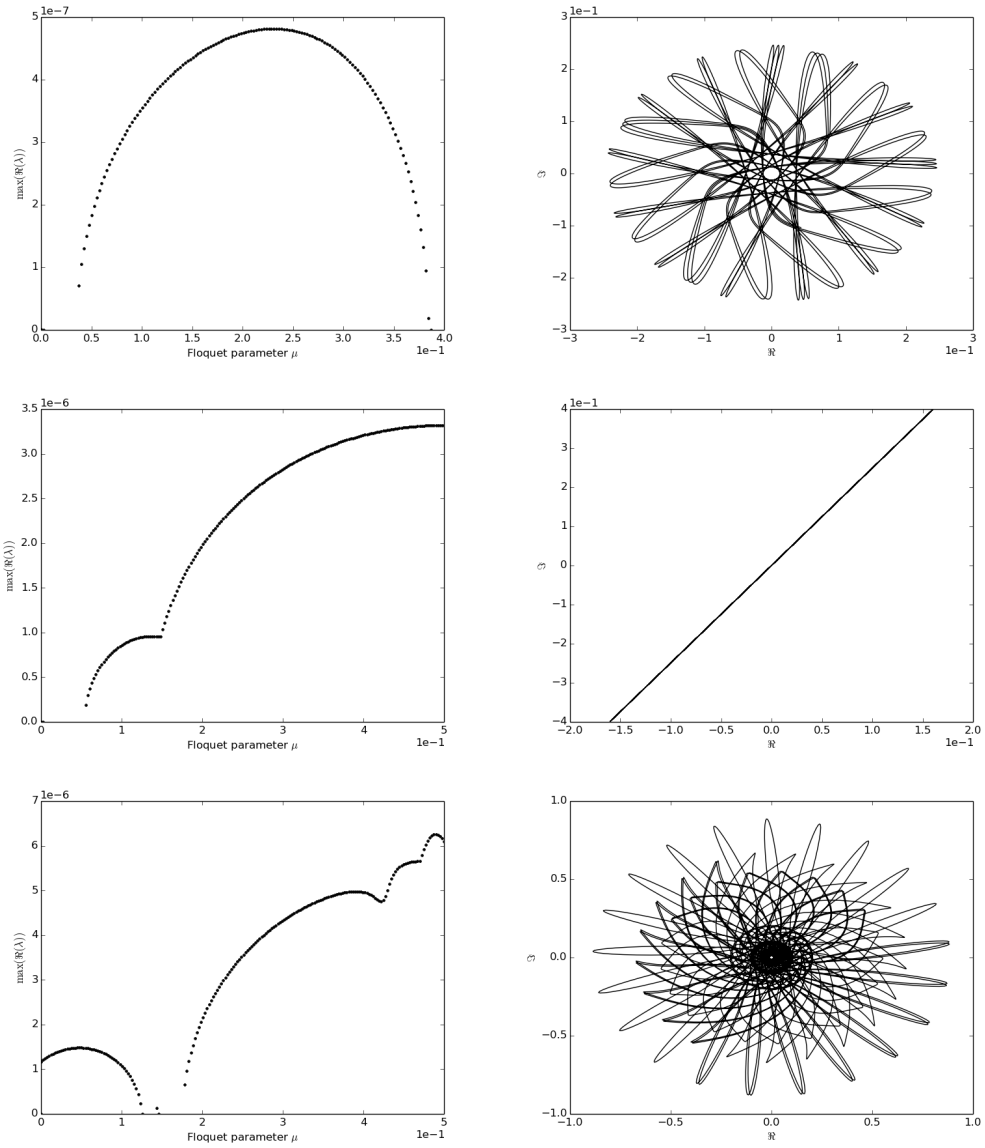

Figure 4.15: This figure shows some stability results for a coefficient of surface tension that gives resonance at $k = 10$ as we vary the amplitude. On the left, we see for which Floquet parameters we have the largest instabilities that in turn gives us the period of the unstable perturbations. On the right, we have the polar plot of the real versus imaginary parts of the eigenfunctions for the largest instabilities.

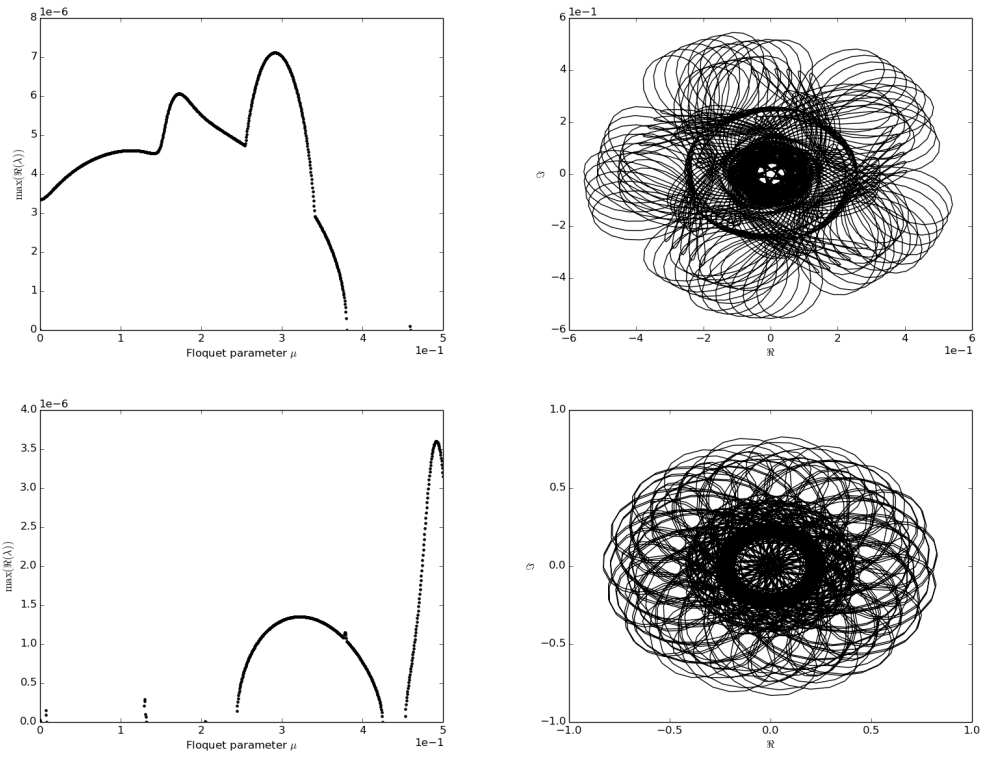

Figure 4.16: This figure shows some stability results for a coefficient of surface tension that gives resonance at $k = 10.5$ and 11 while the wave amplitude remains fixed. On the left, we see for which Floquet parameters we have the largest instabilities that in turn gives us the period of the unstable perturbations. On the right, we have the polar plot of the real versus imaginary parts of the eigenfunctions corresponding to the largest instabilities.

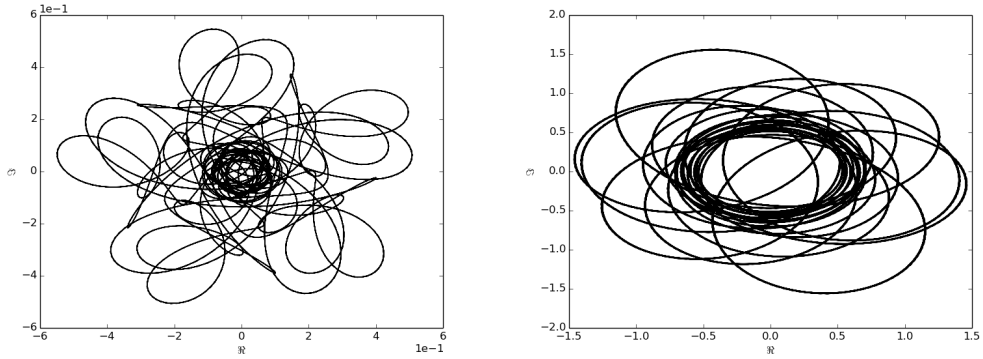

Figure 4.17: Replotting of the figures seen in the right column, but for rational Floquet parameters near the largest eigenvalues for resonance at $k = 10.5$ and $k = 11$ with $\mu = 0.2$ and $\mu = 0.5$ respectively.

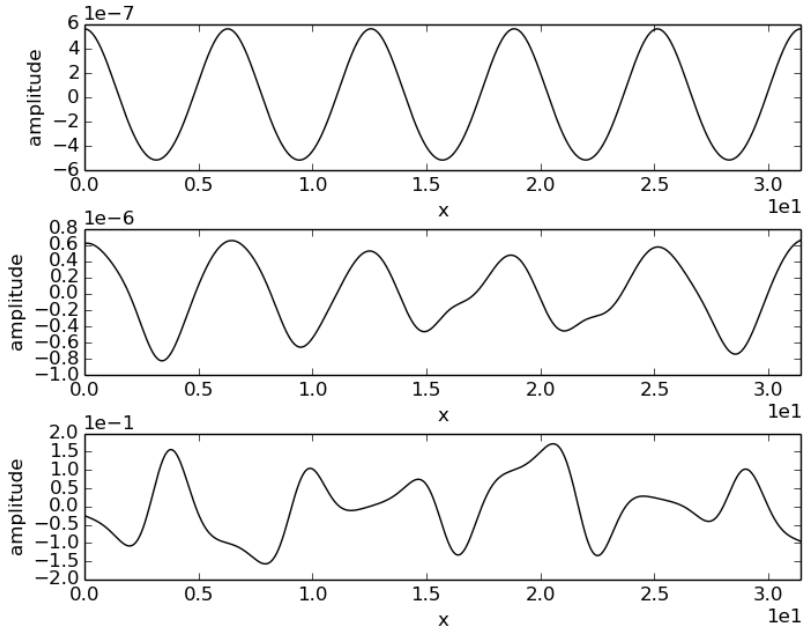

Figure 4.18: Evolution of the wave profiles when perturbed with the eigenfunctions corresponding to the largest eigenvalue show in the top box of Figure 4.12. The top box is the initial profile at $t = 0$, the middle is at $t = 1.3 \times 10^7$ and the bottom is for $t = 4.0 \times 10^7$ with $\mu = 0.23115578$ and $\lambda = 4.81475800724 \times 10^{-7} - 9.71119481185i \times 10^{-7}$

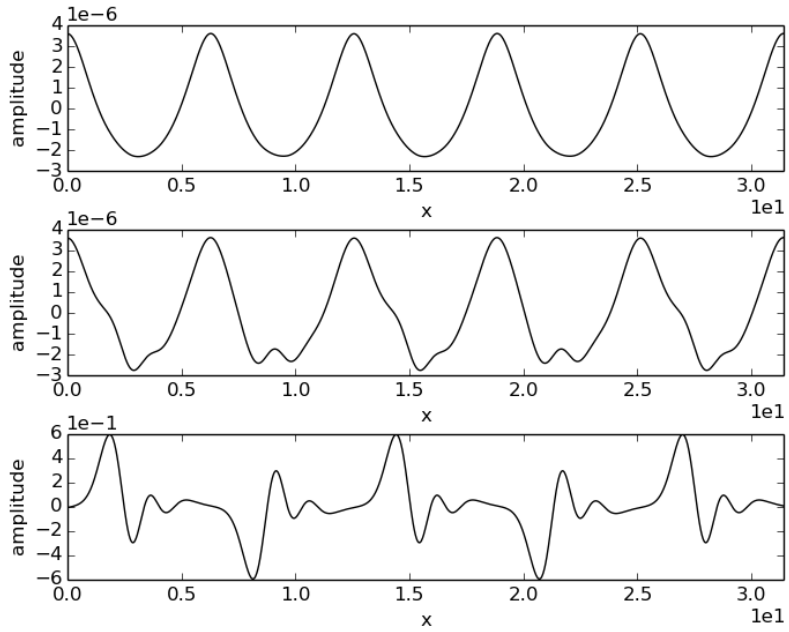

Figure 4.19: Evolution of the wave profiles when perturbed with the eigenfunctions corresponding to the largest eigenvalue show in the top box of Figure 4.12. The top box is the initial profile at $t = 0$, the middle is at $t = 1.0 \times 10^6$ and the bottom is for $t = 5.0 \times 10^6$ with $\mu = 0.5$ and $\lambda = 3.32016333269 \times 10^{-6}$

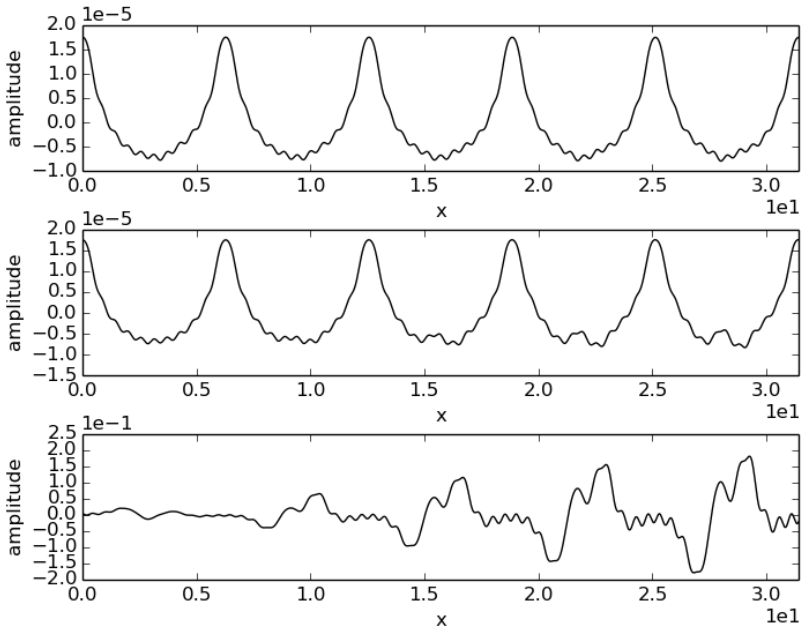

Figure 4.20: Evolution of the wave profiles when perturbed with the eigenfunctions corresponding to the largest eigenvalue shown in the top box of Figure 4.12. The top box is the initial profile at $t = 0$, the middle is at $t = 3.0 \times 10^5$ and the bottom is for $t = 2.0 \times 10^6$ with $\mu = 0.48994975$ and $\lambda = 6.25673658085 \times 10^{-6} + 1.54887125215i \times 10^{-5}$

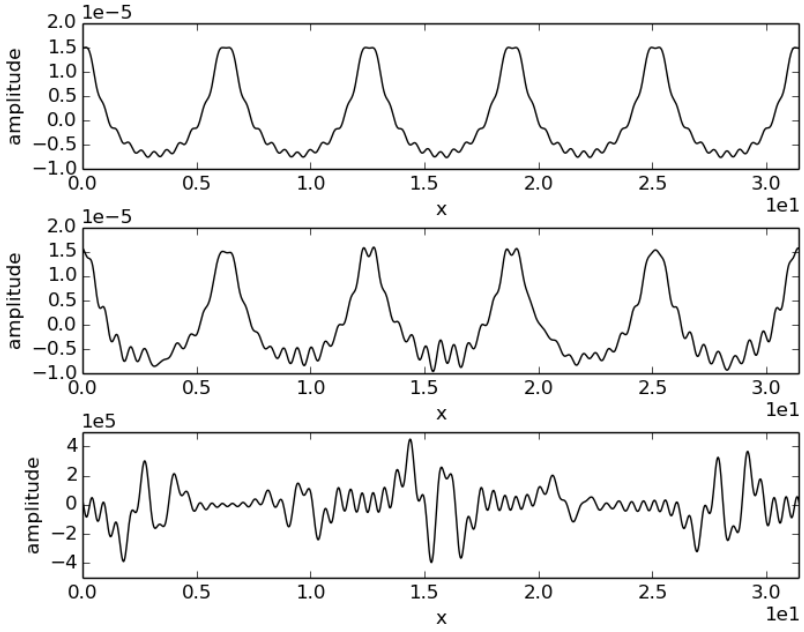

Figure 4.21: Evolution of the wave profiles when perturbed with the eigenfunctions $\mu = 0.1971972$ and $\lambda = 5.57044284138 \times 10^{-6} - 5.71304295611i \times 10^{-6}$ to the coefficient of surface tension for resonance at $k = 10.5$. The top box is the initial profile at $t = 0$, the middle is at $t = 5.0 \times 10^5$ and the bottom is for $t = 5.0 \times 10^6$.

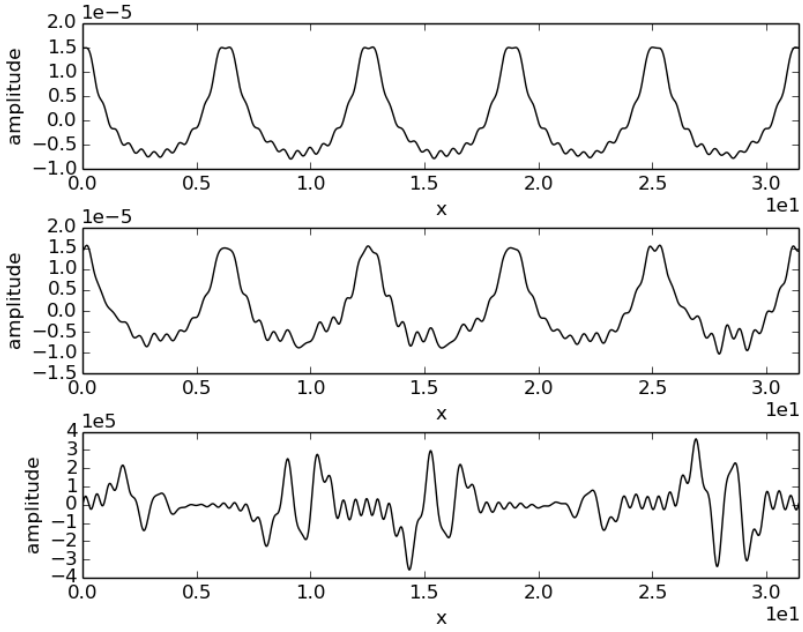

Figure 4.22: Evolution of the wave profiles when perturbed with the eigenfunctions $\mu = 0.1971972$ and $\lambda = 6.05817717444 \times 10^{-6} - 5.8089465785i \times 10^{-6}$ to the coefficient of surface tension for resonance at $k = 10.5$. The top box is the initial profile at $t = 0$, the middle is at $t = 5.0 \times 10^5$ and the bottom is for $t = 5.0 \times 10^6$.

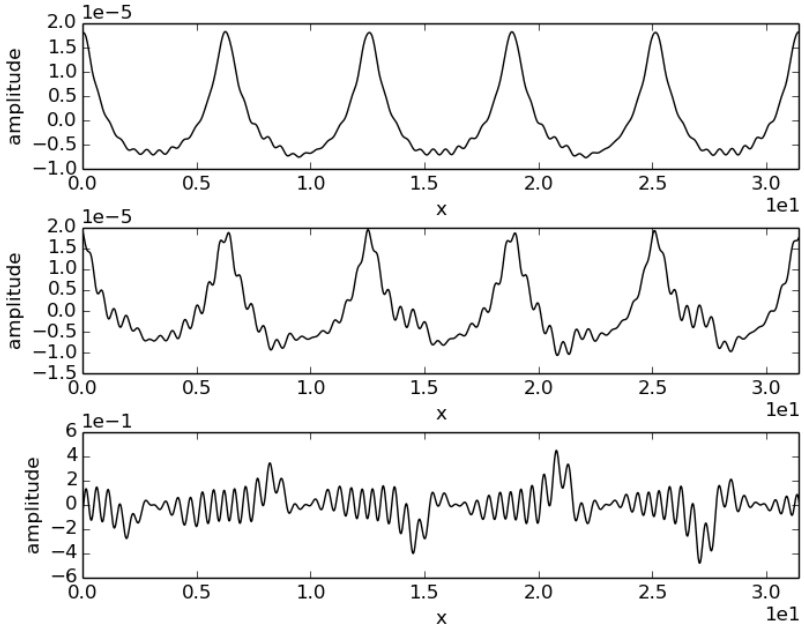

Figure 4.23: Evolution of the wave profiles when perturbed with the eigenfunctions $\mu = 0.47347347$ and $\lambda = 1.94133924544 \times 10^{-6} + 8.09440532587i \times 10^{-6}$ to the coefficient of surface tension for resonance at $k = 10.5$. The top box is the initial profile at $t = 0$, the middle is at $t = 1.2 \times 10^6$ and the bottom is for $t = 7.0 \times 10^6$.

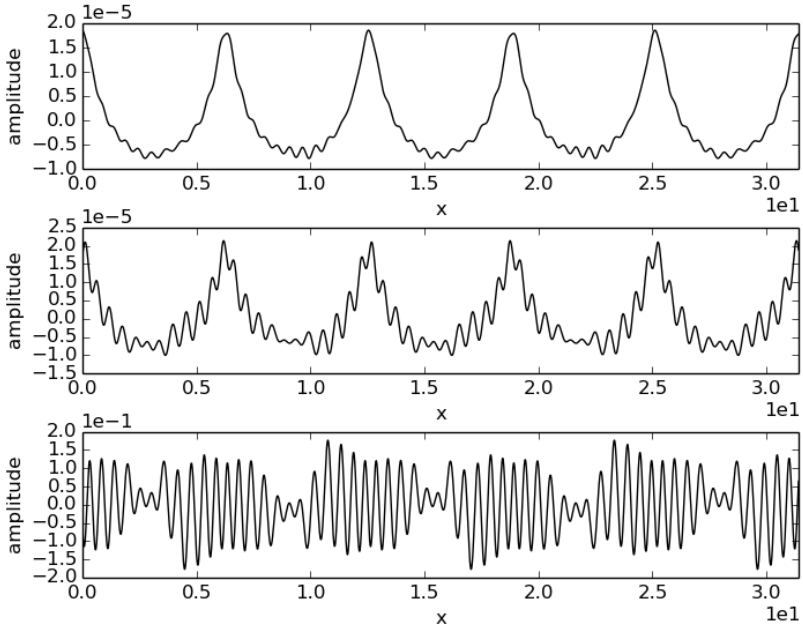

Figure 4.24: Evolution of the wave profiles when perturbed with the eigenfunctions $\mu = 0.49149149$ and $\lambda = 3.59926705991 \times 10^{-6} + 1.04354199298i \times 10^{-5}$ to the coefficient of surface tension for resonance at $k = 10.5$. The top box is the initial profile at $t = 0$, the middle is at $t = 7.0 \times 10^5$ and the bottom is for $t = 4.0 \times 10^6$.

Chapter 5

A GENERAL THEORY FOR THE STABILITY OF SMALL-AMPLITUDE SOLUTIONS OF HAMILTONIAN PDES

5.1 Introduction

In this chapter, we present the results to be published in a paper titled "High-frequency instabilities of small-amplitude solutions of Hamiltonian PDEs" by Deconinck & Trichtchenko. This is a more general theory than what has been presented so far in the previous chapters. As already mentioned, studying what happens when we linearize about a solution (for example the trivial case of $u = 0$) of a partial differential equation (PDE) dictates much of the dynamics of its solutions, including their stability or instability. In this chapter, we focus specifically on the spectral stability of periodic travelling-wave solutions of Hamiltonian PDEs as they bifurcate away from a trivial (usually zero) solution. Our work follows earlier ideas of MacKay [61] and MacKay and Saffman [62].

We start from an autonomous Hamiltonian system of PDEs [4] *i.e.*,

$$u_t = J\frac{\delta H}{\delta u}. \tag{5.1}$$

Here and throughout, indices x or t denote partial derivatives. Further, $u = (u_1(x,t), \ldots, u_N(x,t))^T$ is an N-dimensional vector function defined in a suitable function space, and J is a Poisson operator [4, 30]. More details and examples are given below. Finally, $H = \int_D \mathcal{H}(u, u_x, \ldots)dx$ is the Hamiltonian, whose density $\mathcal{H}$ depends on u and its spatial derivatives, defined for $x \in D$. We consider only the stability of periodic solutions, thus D is any interval of length L, the period. For some of our examples $\mathcal{H}$ will depend on spatial derivatives of u of arbitrary order.

To investigate the stability of travelling wave solutions of this system, we reformulate (5.1) in a frame moving with speed c, using the transformation $\hat{x} = x - ct$, $\hat{t} = t$, and considering solutions $u(\hat{x}, \hat{t}) = U(\hat{x})$ (successively omitting hats). This leads to

$$u_t - cu_x = J\frac{\delta H}{\delta u} \quad \Leftrightarrow \quad u_t = J\frac{\delta H_c}{\delta u}, \tag{5.2}$$

for a modified Hamiltonian H_c. Travelling wave solutions are solutions of the ordinary differential system

$$-cU_x = J\frac{\delta H}{\delta U} \quad \Leftrightarrow \quad 0 = J\frac{\delta H_c}{\delta U}. \tag{5.3}$$

Thus if J is invertible, travelling waves are stationary points of the Hamiltonian H_c. The system (5.3) typically has the zero (trivial) solution for a range of c values. The small-amplitude solutions whose stability we investigate bifurcate away from these trivial zero-amplitude solutions at special values of the speed parameter c, as is schematically shown in Fig. 5.1. It is our goal to see to what extent anything can be said about the stability of the small-amplitude solutions (with amplitudes in the shaded regions of Fig. 5.1) from knowledge of the zero-amplitude solutions at the bifurcation point. An outline of the steps in this process is as follows

1. Obtain the **quadratic Hamiltonian** H_c^0 for the system linearized around the zero solution.

2. Compute the **dispersion relation** $\omega(k)$ using Fourier analysis. For periodic systems of period L, the values of k are restricted to be of the form $2\pi n/L$, $n \in \mathbb{Z}$.

3. Determine at which values of $c = \omega/k$, the **bifurcation branches** start.

4. Compute the **stability spectrum** λ for the zero solution using a Floquet decomposition.

5. Check the **collision condition** for different λ.

6. Compute the **Krein signature** at the collision point for the colliding eigenvalues.

5.2 Motivating example

Our investigations began with the study of the so-called Whitham equation [88], [89, page 368]. The equation is usually posed on the whole line,

$$u_t + N(u) + \int_{-\infty}^{\infty} K(x-y)u_y(y,t)dy = 0, \tag{5.4}$$

where $N(u)$ denotes the collection of all nonlinear terms in the equation. It is assumed that $\lim_{\epsilon\to 0} N(\epsilon u)/\epsilon = 0$. The last term encodes the dispersion relation of the linearized

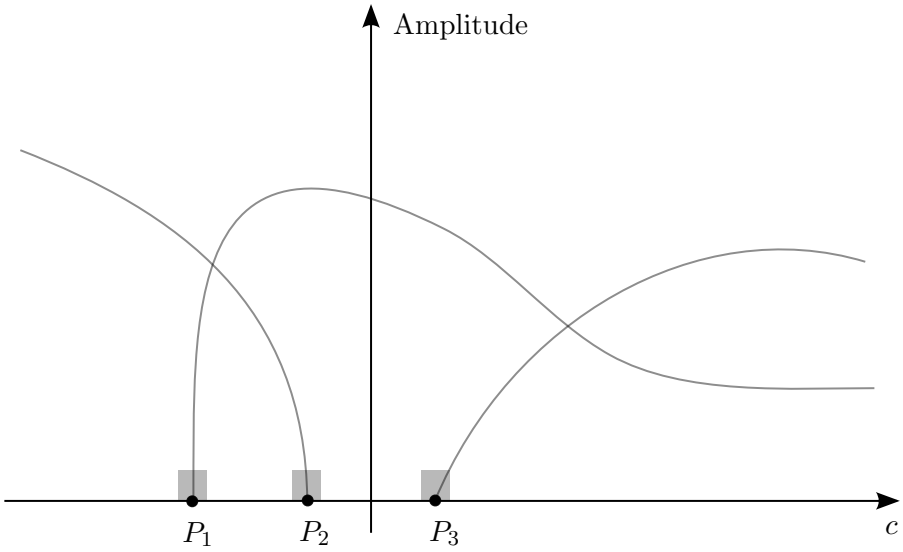

Figure 5.1: A cartoon of the bifurcation structure of the travelling waves for a third-order ($N = 3$) system: solution branches bifurcate away from the trivial zero-amplitude solution at specific values of the travelling wave speed c.

Whitham equation. The kernel $K(x)$ is the inverse Fourier transform of the phase speed $c(k)$, where $c(k) = \omega(k)/k$, with $\omega(k)$ the dispersion relation. Here $c(k)$ is assumed to be real valued and nonsingular for $k \in \mathbb{R}$. Thus

$$K(x) = \frac{1}{2\pi} \fint_{-\infty}^{\infty} c(k) e^{ikx} dk, \tag{5.5}$$

where $\fint$ denotes the principal value integral. Depending on $c(k)$, this equation may have to be interpreted in a distributional sense [32, 80]. Letting $u \sim \exp(ikx - \omega(k)t)$, it is a straightforward calculation to see that the dispersion relation of the linear Whitham equation is $\omega(k)$. In fact, the linear Whitham equation is easily seen to be a rewrite of the linear evolution equation [2]

$$u_t = -i\omega(-i\partial_x)u, \tag{5.6}$$

where $\omega(-i\partial_x)$ is a linear operator with the property $\omega(k) = -\omega(-k)$. Indeed, letting $\omega(-i\partial_x)$ act on

$$u(x,t) = \frac{1}{2\pi}\int_{-\infty}^{\infty} e^{ikx}\hat{u}(k,t)dk, \tag{5.7}$$

and replacing $\hat{u}(k,t)$ by

$$\hat{u}(k,t) = \int_{-\infty}^{\infty} e^{-iky}u(y,t)dy, \tag{5.8}$$

the linear part of (5.4) is obtained after one integration by parts. We restrict our considerations to odd dispersion relations, to ensure the reality of the Whitham equation.

One of Whitham's reasons for writing down the equation [88, 89] was to describe waves in shallow water (leading to the inclusion of a KdV-type nonlinearity $N(u) \sim uu_x$) that feel the full dispersive response of the one-dimensional water wave problem (without surface tension), for which

$$\omega^2(k) = gk\tanh(kh), \tag{5.9}$$

with g the acceleration of gravity and water depth h. It is common to choose $c(k) = \omega_1(k)/k > 0$ in (5.4), so that $\omega_1(k)$ is the root of (5.9) with the same sign as k. In what follows, we refer to this choice as the Whitham equation. The stability of periodic travelling wave solutions of the Whitham equation has received some attention recently. Notable are [31], where the focus is on solitary waves, and [43], where the modulational instability of small-amplitude periodic solutions is emphasized. Most recently, the spectral stability of periodic solutions of the Whitham equation was examined in [76]. The goal of considering an equation like (5.4) is to capture as much of the dynamics of the full water wave problem as possible, without having to cope with the main difficulties imparted by the full water wave problem [86] discussed in previous chapters. One of the important aspects of the dynamics of a nonlinear problem is the (in)stability of its travelling wave solutions. Thus far, we have shown that periodic travelling wave solutions of the one-dimensional Euler water wave problem are spectrally unstable for all possible values of their parameters h, g, amplitude, and wave period. The nature of the instabilities depends on the value of these parameters: as is well known, waves in deep water are susceptible to the Benjamin-Feir or modulational instability (see [96] for a review). In addition, waves in both deep and shallow water of all

non-zero amplitudes are unstable with respect to high-frequency perturbations. The work in [76] does not reveal any high-frequency instabilities for solutions of small amplitude in water that is shallow in the context of the Whitham equation. Thus an important aspect of the Euler water wave dynamics is absent from (5.4). We will provide an analytical indication that the Whitham equation misses the presence of these instabilities, while explaining why they are missed. This explanation leads to a way to address this problem.

For suitable $N(u)$, the Whitham equation (5.4) is a Hamiltonian system. The Lagrangian structure with the dispersion relation given by $\omega_1(k)$ as in (5.9) was already given by Whitham in [88], from which the Hamiltonian structure easily follows. Explicitly, for the linearized Whitham equation posed on the whole line, for any odd $\omega(k)$ we have

$$H = -\frac{1}{2}\int_{-\infty}^{\infty}\int_{-\infty}^{\infty} K(x-y)u(x)u(y)dxdy, \tag{5.10}$$

with $J = \partial_x$. Then

$$u_t = \partial_x \frac{\delta H}{\delta u}. \tag{5.11}$$

If instead the linearized equation is posed with periodic boundary conditions $u(x+L,t) = u(x,t)$, it follows immediately from (5.6) that we have

$$u_t + \int_{-L/2}^{L/2} K(x-y)u(y)dy = 0, \tag{5.12}$$

where we have used a Fourier series instead of a Fourier transform. Further,

$$K(x) = \frac{1}{L}\sum_{j=-\infty}^{\infty} c(k_j)e^{ik_j x}, \tag{5.13}$$

and $k_j = 2\pi j/L$, $j \in \mathbb{Z}$. The Hamiltonian formulation for the periodic Whitham equation (5.12) is also given by (5.11), but with

$$H = -\frac{1}{2}\int_{-L/2}^{L/2}\int_{-L/2}^{L/2} K(x-y)u(x)u(y)dxdy. \tag{5.14}$$

In fact, a formal limit $L \to \infty$ immediately results in the recovery of the equation posed on the whole line. Thus the Whitham equation and its periodic solutions fit into the framework

developed in this manuscript. It is one of many examples we use below. Other notable examples are the Euler water wave problem (as expected, allowing us to check our results with those of MacKay & Saffman [62]), the KdV equation, the Sine-Gordon equation, *etc.* We are particularly interested in the comparison between the results for the Euler water wave problem and those for the Whitham equation.

The results of Examples 5.4.2 and 5.5.2 show that the Whitham equation cannot possess the high-frequency instabilities present in the water wave problem. This leads us to propose a new model equation, a so-called Boussinesq-Whitham or bidirectional Whitham equation. This equation is shown to at least satisfy the same necessary condition for the presence of high-frequency instabilities as the water wave problem, and these high-frequency instabilities originate from the same points on the imaginary axes as they do for the Euler equations.

5.3 Method

We gave the basic steps for the method in the introduction, but here we discuss the details of each of the steps of the method. Throughout this chapter, our emphasis is on generality and usability, as opposed to rigor. As a consequence some of the statements made below are necessarily vague: more precise statements would limit the generality aimed for. Within the context of more specific examples, more precision may be possible.

1. **Quadratic Hamiltonian**. A linear system of equations is obtained by linearizing the system (5.3) around the zero solution: let $u = \epsilon v + \mathcal{O}(\epsilon^2)$ and omit terms of order $o(\epsilon)$. Alternatively, if J is independent of u and its spatial derivatives, one may expand the Hamiltonian H_c as a function of ϵ and retain its quadratic terms. This Hamiltonian H_c^0 of the linearized system is the starting point for the next steps.

2. **Dispersion relation**. The linearized system has constant coefficients and is easily solved using Fourier analysis. Its time dependence is governed by the dispersion relation $F(\omega, k) = 0$ of the problem. Here $F(\omega, k) = 0$ is of degree N in ω. It is a fundamental assumption of our approach that **all solutions** $\omega_j(k)$ **are real for** $k \in \mathbb{R}$. The dispersion relation can be expressed entirely in terms of the coefficients appearing

in the quadratic Hamiltonian H_c^0. Recall that the dispersion relation is obtained by investigating solutions whose spatial and temporal dependence is proportional to $\exp(ikx - i\omega t)$. For periodic systems of period L, the values of k are restricted to be of the form $2\pi n/L$, $n \in \mathbb{Z}$.

3. **Bifurcation branches**. The values of the phase speed $c = \omega/k$ for which nontrivial solutions bifurcate away from the zero-amplitude solution are determined by the condition that the zero solution is *not* the unique solution to the Fourier transformed problem. In effect, this is the classical bifurcation condition that a Jacobian is singular. This simple calculation determines the bifurcation branch starting points explicitly in terms of the different solutions to the dispersion relation. In what follows, we follow the first branch, starting at c_1, without loss of generality.

   It is assumed that only a single non-trivial bifurcation branch emanates from a bifurcation point. Although more general cases can be incorporated, we do not consider them here. Further, we fix the period of the solutions on the bifurcation branch (usually to 2π). Other choices can be made. Instead of varying the amplitude as a function of the speed for fixed period, one could fix the speed and vary the period, *etc.* The methods presented can be redone for those scenarios in a straightforward fashion.

4. **Stability spectrum**. The spectrum of the linear operator determining the spectral stability of the zero solution at the bifurcation branch on the first branch is calculated. Since this spectral problem has constant coefficients, this calculation can be done explicitly. Again, this is done entirely in terms of the dispersion relation of the problem. Using a Floquet decomposition (see [23, 51]), the spectrum is obtained as a collection of point spectra, parameterized by the Floquet exponent $\mu \in (-\pi/L, \pi/L]$. Due to the reality of the branches of the dispersion relation, the spectrum is confined to the imaginary axis. In other words, the zero-amplitude solutions are spectrally stable. The use of the Floquet decomposition allows for the inclusion of perturbations that are not necessarily periodic with period L. Instead, the perturbations may be quasiperiodic with two incommensurate periods, subharmonic (periodic, but with

period an integer multiple of L), or spatially localized [23, 38, 51].

5. **Collision condition**. Given the explicit expression for individual eigenvalues λ, it is easy to find the conditions for which eigenvalues corresponding to different parameters (Floquet exponent, branch number of the dispersion relation, *etc.*) coincide on the imaginary axis. This is referred to as the **collision condition**. Once again, it is given entirely in terms of the dispersion relation.

   It is a consequence of the Floquet theorem [15] that collisions need to be considered only for spectral elements corresponding to the same value of the Floquet exponent since the subspaces of eigenfunctions for a fixed Floquet exponent are invariant under the flow of the linearized equation.

6. **Krein signature**. Having obtained the stability spectrum at the starting point of the bifurcation branches, we wish to know how the spectrum evolves as we move up a bifurcation branch. One tool to investigate this is the Krein signature [53, 54, 55, 61, 69]. In essence, the Krein signature of an eigenvalue is the sign of the Hamiltonian of the linearized system evaluated on the eigenspace of the eigenvalue. Different characterizations are given below. If two imaginary eigenvalues of the same signature collide as a parameter changes, their collision does not result in them leaving the imaginary axis. Thus the collision of such eigenvalues does not result in the creation of unstable modes. In other words, it is a necessary condition for collisions to lead to instability that the Krein signature of the colliding eigenvalues is different. This scenario is illustrated in Fig. 5.2. That figure also illustrates the quadrifold symmetry of the stability spectrum of the solution of a Hamiltonian system: for each eigenvalue $\lambda \in \mathbb{C}$, λ^*, $-\lambda$ and $-\lambda^*$ are also eigenvalues. Here λ^* denotes the complex conjugate of λ. It should be noted that the occurrence of a collision is required for eigenvalues to leave the imaginary axis, due to the quadrifold symmetry of the spectrum.

   Thus we calculate the Krein signature of any coinciding eigenvalues, obtained in Step 5. If these Krein signatures are equal, the eigenvalues will remain on the imaginary axis as the amplitude is increased. Otherwise, the eigenvalues may leave the imaginary

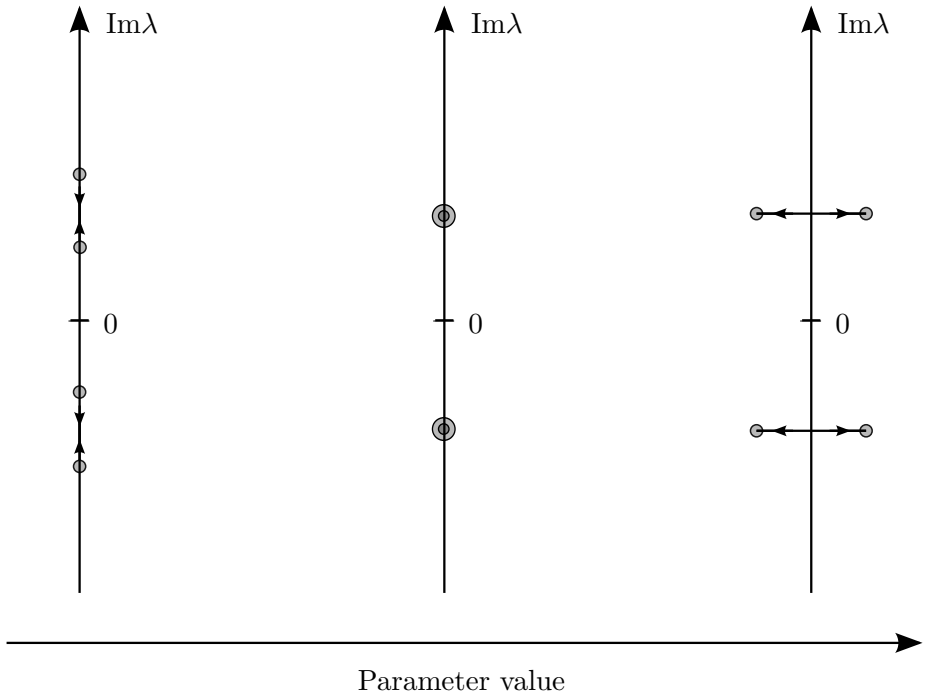

Figure 5.2: Colliding eigenvalues in the complex plane as a parameter is increased. On the left, two eigenvalues are moving towards each other on the positive imaginary axis, accompanied by a complex conjugate pair on the negative imaginary axis. In the middle, the eigenvalues in each pair have collided. On the right, a Hamiltonian Hopf bifurcation occurs: the collided eigenvalues separate, leaving the imaginary axis (implying that the two Krein signatures were different).

axis, through a so-called Hamiltonian Hopf bifurcation [85], resulting in instability. Thus we establish a necessary condition for the instability of periodic solutions of small amplitude. The Krein signature condition cannot be expressed entirely in terms of the dispersion relation, and the coefficients of H_c^0 are required as well. Please refer to the next two sections for details.

Although all calculations are done for the zero-amplitude solutions at the starting point of a bifurcation branch, the continuous dependence of the stability spectrum on the parameters in the problem [41], including the velocity of the travelling wave or the amplitude of the solutions, guarantees that the stability conclusions obtained persist for solutions of small amplitude. Thus meaningful conclusions about solutions in the shaded regions of the

bifurcation branches of Fig. 5.1 are reached, despite the fact that we are unable to say anything about the size of the maximal amplitude for which these conclusions are valid.

5.4 Scalar Hamiltonian PDEs

In this section, we investigate the stability of 2π-periodic travelling wave solutions of Hamiltonian systems of the form

$$u_t = \partial_x \frac{\delta H}{\delta u}, \tag{5.15}$$

where $u(x,t)$ is a scalar real-valued function. Thus $J = \partial_x$. Since this Poisson operator is singular, all equations of this form conserve the quantity $\int_0^{2\pi} u dx$, which is the Casimir for this Poisson operator. Systems of this form include the Korteweg- de Vries equation [35, 95] and its many generalizations, the Whitham equation (5.4), and many others. As mentioned above, our only interest is in the linearization of these equations around their trivial solution. We write the quadratic part H^0 of H as

$$H^0 = -\frac{1}{2}\int_0^{2\pi} \sum_{n=0}^{\infty} \alpha_n u_{nx}^2 dx, \tag{5.16}$$

where the coefficients $\alpha_n \in \mathbb{R}$. For most examples, the number of terms in (5.16) is finite, and all but a few of the coefficients α_n are nonzero. For the Whitham equation (5.4), the number of nonzero terms is infinite, but convergence is easily established. Using the notation (5.16), the linearized equation is

$$u_t = -\sum_{n=0}^{\infty} (-1)^n \alpha_n u_{(2n+1)x}. \tag{5.17}$$

As before, indices on u denote partial derivatives. Specifically, $u_{(2n+1)x}$ denotes $\partial_x^{2n+1} u$. We proceed with the six steps outlined in the introduction.

1. **Quadratic Hamiltonian.** The modified Hamiltonian H_c^0 is given by

$$H_c^0 = \frac{c}{2}\int_0^{2\pi} u^2 dx - \frac{1}{2}\int_0^{2\pi} \sum_{n=0}^{\infty} \alpha_n u_{nx}^2 dx. \tag{5.18}$$

2. **Dispersion relation.** For equations of the form (5.15), the dispersion relation has only a single branch:

$$\omega(k) = \sum_{n=0}^{\infty} \alpha_n k^{2n+1}, \tag{5.19}$$

The absence of even powers of k in (5.19) is due to our imposition that (5.17) is a conservative equation, *i.e.*, there is no dissipation. All integers are allowable k values, since we have equated the period to be 2π. The equation (5.17) may be written as

$$u_t = -i\omega(-i\partial_x)u. \tag{5.20}$$

3. **Bifurcation branches.** Since (5.15) is scalar, only one branch can bifurcate away from the trivial solution. To find the corresponding value of c, we write (5.17) in a moving frame, as

$$u_t - cu_x = i\omega(i\partial_x)u. \tag{5.21}$$

This equation has its own dispersion relation, given by

$$\Omega(k) = \omega(k) - ck, \tag{5.22}$$

obtained by looking for solutions of the form $u = \exp(ikx - i\Omega t)\hat{u}$. Letting $u = \sum_{n=-\infty}^{\infty} \exp(inx)\hat{u}_n$, it follows that $\partial_t \hat{u}_n = -i\Omega(n)\hat{u}_n$. Thus a nonzero stationary solution may exist provided $\Omega(N) = 0$, for $N \in \mathbb{N}, N \neq 0$. We have used the oddness of $\Omega(N)$ to restrict to strictly positive values of N. Thus the starting point of the bifurcation branch in the (speed, amplitude)-plane is $(c, 0)$, where c is determined by

$$c = \frac{\omega(N)}{N}, \tag{5.23}$$

for any integer $N > 0$. Choosing $N > 1$ implies that the fundamental period of the solutions is not 2π, but $2\pi/N$. In practice, we choose $N = 1$.

A Fourier series approximation to the explicit form of the small-amplitude solutions corresponding to this bifurcation branch may be obtained using a standard Stokes expansion [81, 89].

4. **Stability spectrum.** In order to compute the stability spectrum associated with the zero-amplitude solution at the start of the bifurcation branch, we let $u(x,t) = U(x)\exp(\lambda t)$+c.c., where c.c. denotes the complex conjugate of the preceding term. As usual, if any λ are found for which the real part is positive, the solution is spectrally unstable [51]. All bounded eigenfunctions $U(x)$ may be represented as

$$U(x) = \sum_{n=-\infty}^{\infty} a_n e^{i(n+\mu)x}, \tag{5.24}$$

where $\mu \in (-1/2, 1/2]$ is the Floquet exponent. Such a representation for $U(x)$ is valid even for solutions on the bifurcation branch of nonzero amplitude [23]. Since (5.21) is a problem with constant coefficients, only a single term in (5.24) is required. We obtain

$$\lambda_n^{(\mu)} = -i\Omega(n+\mu) = -i\omega(n+\mu) + i(n+\mu)c, \quad n \in \mathbb{Z}. \tag{5.25}$$

As expected, all eigenvalues are imaginary, and the zero-amplitude solution is neutrally stable. For a fixed value of μ, (5.25) gives a point set on the imaginary axis in the complex λ plane. As μ is varied in $(-1/2, 1/2]$, these points trace out intervals on the imaginary axis. Depending on $\omega(k)$, these intervals may cover the imaginary axis.

5. **Collision condition.** The most generic scenarios for two eigenvalues given by (5.25) to collide are that (i) two of them are zero, and they collide at the origin, and (ii) two of them are equal, but nonzero. We ignore the first possibility, since the next step proves to be inconclusive for this case, as discussed in the introduction. The second

possibility requires $\lambda_n^{(\mu)} = \lambda_m^{(\mu)}$, for some $m, n \in \mathbb{Z}$, $m \neq n$, $\mu \in (-1/2, 1/2]$, and $\lambda_n^{(\mu)}$, $\lambda_m^{(\mu)} \neq 0$. This may be rewritten as

$$\frac{\omega(n+\mu) - \omega(m+\mu)}{n-m} = \frac{\omega(N)}{N}, \quad m, n \in \mathbb{Z}, m \neq n \text{ and } \mu \in (-1/2, 1/2]. \tag{5.26}$$

This equation has an elegant graphical interpretation: the right-hand side is fixed by the choice of N, fixing the bifurcation branch in Step 3. It represents the slope of a line through the origin and the point $(N, \omega(N))$ in the (k, ω) plane. The left hand side is the slope of a line in the same plane passing through the points $(n+\mu, \omega(n+\mu))$ and $(m+\mu, \omega(m+\mu))$, see Fig. 5.3.

Even though the graph of the dispersion relation admits parallel secant lines, this is not sufficient for a solution of (5.26), as it is required that their abscissas are an integer apart.

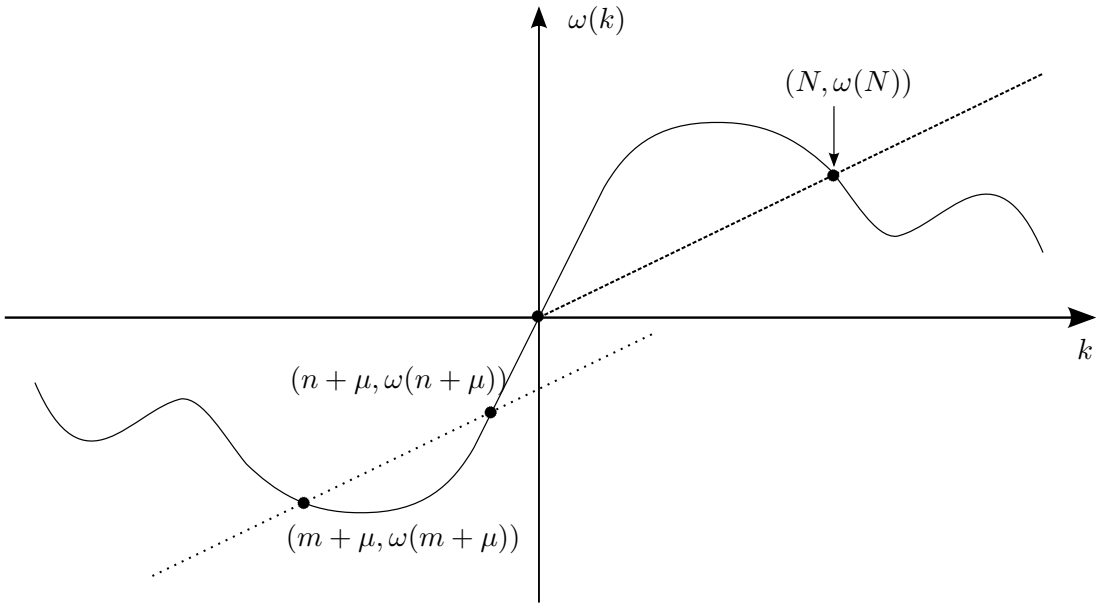

Figure 5.3: The graphical interpretation of the collision condition (5.26). The solid curve is the graph of the dispersion relation $\omega(k)$. The slope of the dashed line in the first quadrant is the right-hand side in (5.26). The slope of the parallel dotted line is its left-hand side.

6. **Krein signature.** The Krein signature of an eigenvalue is the sign of the Hamiltonian H_c^0 evaluated on the eigenspace associated with the eigenvalue. We are considering two simple eigenvalues colliding, thus the eigenspace for each eigenvalue consists of multiples of the eigenfunction only. To allow for eigenfunctions of the form $a_n \exp(i(n+\mu)x + \lambda_n^{(\mu)} t)$+c.c, which are not 2π-periodic (unless $\mu = 0$), it is necessary to replace the integral in (5.16) with a whole-line average. More details on this process are found, for instance, in [25]. A simple calculation shows that the contribution to H_c^0 from the (n, μ) mode is proportional to

$$H_c^0|_{(n,\mu)} \sim -|a_n|^2 \frac{\Omega(n+\mu)}{n+\mu}. \tag{5.27}$$

Other terms are present in the Hamiltonian density, but they have zero average. The sign of this expression is the Krein signature of the eigenvalue $\lambda_n^{(\mu)}$. Thus a necessary condition for $\lambda_n^{(\mu)}$ and $\lambda_m^{(\mu)}$ to leave the imaginary axis for solutions of positive amplitude is that the signs of (5.27) with (n, μ) and (m, μ) are different, contingent on μ, m and n satisfying (5.26). Explicitly, this condition is

$$\operatorname{sign}\left[\frac{\omega(n+\mu)}{n+\mu} - c\right] \neq \operatorname{sign}\left[\frac{\omega(m+\mu)}{m+\mu} - c\right]. \tag{5.28}$$

Alternatively, the product of the left-hand side and the right-hand side should be negative. Using (5.26), (5.28) becomes

$$(n+\mu)(m+\mu) < 0, \tag{5.29}$$

or, provided $mn \neq 0$, and using that $\mu \in (-1/2, 1/2]$,

$$nm < 0. \tag{5.30}$$

Remark.

- It is clear from (5.27) why our methods do not lead to any conclusions about collisions of eigenvalues at the origin. If $\lambda_n^{(\mu)} = 0$, then $\Omega(n+\mu) = 0$, and the contribution to the Hamiltonian of such a mode vanishes. As a consequence, the associated Krein signature is zero.

- When the theory of [53] is restricted to the case of solutions of zero-amplitude, so as to recover the constant coefficient stability problem, the graphical stability criterion given there coincides with the one presented here.

5.4.1 The (generalized) Korteweg - de Vries equation

We consider the generalized KdV (gKdV) equation

$$u_t + \sigma u^n u_x + u_{xxx} = 0, \tag{5.31}$$

where we restrict n to integers 1 or greater. Here σ is a constant coefficient, chosen as convenient. Important special cases discussed below are the KdV equation ($n = 1$) and the modified KdV (mKdV) equation ($n = 2$). Many of the details below extend easily to more general nonlinearities, with the main requirement being that the linearized equation is $u_t + u_{xxx} = 0$. The stability of periodic solutions of the gKdV equation has received some attention recently [11, 12, 22, 46]. For the integrable cases $n = 1$ and $n = 2$, more detailed analysis is possible, see [9, 21, 24]. We do not claim to add anything new to these discussions, but we wish to use this example to illustrate how the six-step process outlined in this section leads to easy conclusions before moving on to more complicated settings.

1. The modified Hamiltonian is given by

$$H_c^0 = \frac{1}{2}\int_0^{2\pi} (u_x^2 + cu^2)dx. \tag{5.32}$$

2. The dispersion relation is

$$\omega = -k^3. \tag{5.33}$$

3. Bifurcation branches in the (c, amplitude)-plane start at $(c, 0)$, with

$$c = \frac{\omega(k)}{k} = -k^2. \tag{5.34}$$

Since we desire 2π periodic solutions, we choose $k = 1$. Any choice $k = N$, where N is a non-zero integer is allowed. Choosing $k = 1$, bifurcation branches start at $(-1, 0)$.

For the integrable cases $n = 1$ (KdV) and $n = 2$ (mKdV), these bifurcation branches may be calculated in closed form. For the KdV equation in a frame travelling with speed c, the 2π-periodic solutions are given by (with $\sigma = 1$)

$$u = \frac{12\kappa^2 K^2(\kappa)}{\pi^2} \mathrm{cn}^2\left(\frac{K(\kappa)x}{\pi}, \kappa\right), \tag{5.35}$$

where cn denotes the Jacobian elliptic cosine function and $K(\kappa)$ is the complete elliptic integral of the first kind [27, 73]. Further,

$$c(\kappa) = \frac{4K^2(\kappa)}{\pi^2}(2\kappa^2 - 1), \tag{5.36}$$

resulting in an explicit bifurcation curve $(c(\kappa), 12\kappa^2 K^2(\kappa)/\pi^2)$, parameterized by the elliptic modulus $\kappa \in [0, 1)$. This bifurcation curve is shown in Fig. 5.4a.

For the mKdV equation ($n = 2$), different families of travelling-wave solutions exist [24]. We consider two of the simplest. For $\sigma = 3$ (focusing mKdV), a family of 2π-periodic solutions is given by

$$u = \frac{2\sqrt{2}\kappa K(\kappa)}{\pi} \mathrm{cn}\left(\frac{2K(\kappa)x}{\pi}, \kappa\right), \tag{5.37}$$

with $c(\kappa)$ given by (5.36), resulting in an explicit bifurcation curve $(c(\kappa), 2\sqrt{2}\kappa K(\kappa)/\pi)$, parameterized by the elliptic modulus $\kappa \in [0, 1)$. This bifurcation curve is shown in

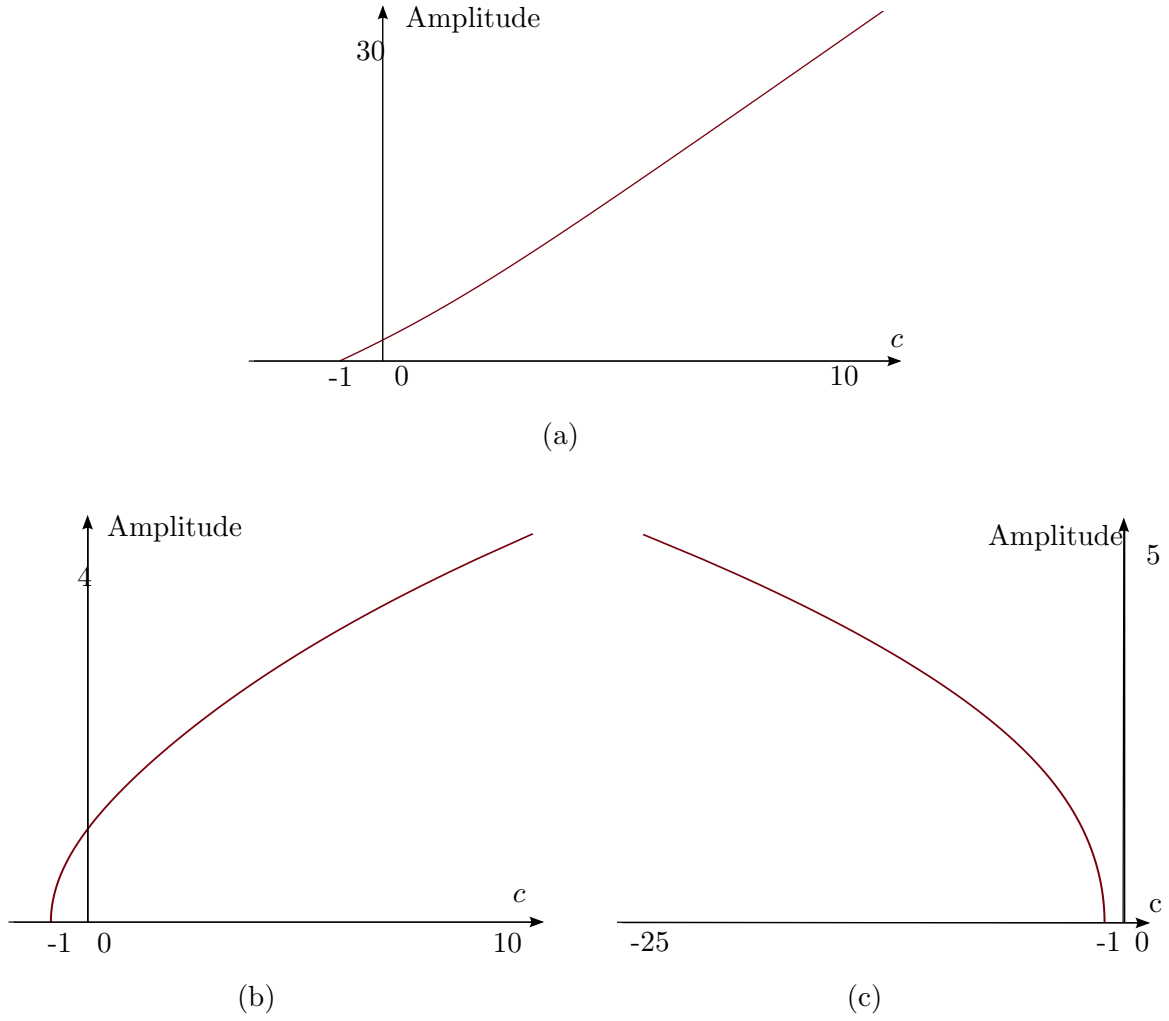

Figure 5.4: The amplitude *vs.* c bifurcation plots for the travelling-wave solutions of the generalized KdV equation (5.31). (a) The KdV equation, $n = 1$, for the cnoidal wave solutions (5.35). Note that all bifurcation branches start at $(-1, 0)$, as stated above.

Fig. 5.4b. It should be noted that a solution branch exists where the solution is expressed in terms of the Jacobian dn function [27, 73]: $u = \sqrt{(2)}K(\kappa)\mathrm{dn}(K(\kappa)x/\pi, \kappa)/\pi$, but this solution does not have a small-amplitude limit and our methods do not apply directly to it. Rather, the solutions limit to the constant solution $u = 1/\sqrt{2}$ as $\kappa \to 0$. A simple transformation $v = u - 1/\sqrt{2}$ transforms the problem to one where our methods apply.

For $\sigma = -3$ (defocusing mKdV), a period 2π solution family is

$$u = \frac{2\sqrt{2}\kappa K(\kappa)}{\pi}\mathrm{sn}\left(\frac{2K(\kappa)x}{\pi}, \kappa\right), \tag{5.38}$$

with $c(\kappa) = -4(1+\kappa^2)K^2(\kappa)/\pi^2$. Here sn is the Jacobian elliptic sine function [27, 73], resulting in an explicit bifurcation curve $(c(\kappa), 2\sqrt{2}\kappa K(\kappa)/\pi)$, parameterized by the elliptic modulus $\kappa \in [0, 1)$. This bifurcation curve is shown in Fig. 5.4c.

4. The stability spectrum is given by (5.25), with $\omega(k) = -k^3$ and $c = -1$, resulting in

$$\lambda_\mu^{(n)} = i(n+\mu)(1+(n+\mu)^2). \tag{5.39}$$

These eigenvalues cover the imaginary axis, as n and μ are varied. The imaginary part of this expression is displayed in Fig. 5.5a. For the sake of comparison with Fig. 2 in [9] we let $\mu \in [-1/4, 1/4)$, which implies that n is any half integer. The results of Fig. 2 in [9] are for elliptic modulus $\kappa = 0.8$, implying a solution of moderate amplitude. The comparison of these two figures serves to add credence to the relevance of the results obtained using the zero-amplitude solutions at the start of the bifurcation branch.

5. With $k = n + \mu$ and $k + l = m + \mu$, for some $l \in \mathbb{Z}$, the collision condition is written as

$$l^2 + 3kl + 3k^2 - 1 = 0, \tag{5.40}$$

where the trivial solution $l = 0$ has been discarded. This is the equation of an ellipsoid in the (k, l) plane. It intersects lines of nonzero integer l in six integer points: $\pm(1, -2)$, $\pm(0, 1)$, $\pm(1, -1)$. Since for all of these, $\Omega(k) = 0$, any collisions happen only at the origin $\lambda_n^{(\mu)} = 0$. This is also illustrated in Fig. 5.5b.

6. The final step of our process is preempted by the results of the previous step. No Krein signature of colliding eigenvalues can be computed, since no eigenvalues collide.

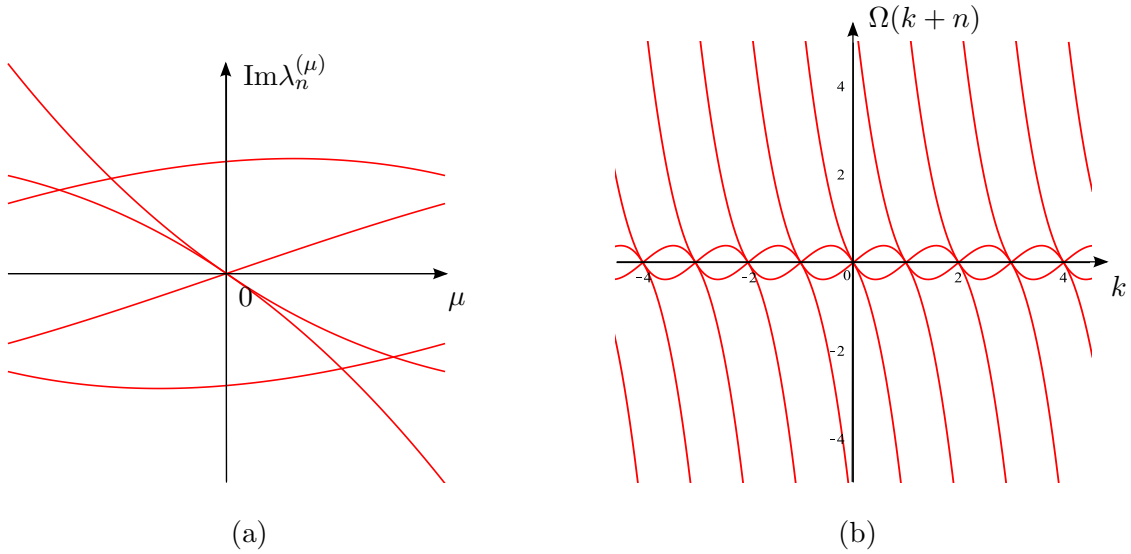

(a) (b)

Figure 5.5: (a) The imaginary part of $\lambda_n^{(\mu)} \in (-0.7, 0.7)$ as a function of $\mu \in [-1/4, 1/4)$. (b) The curves $\Omega(k+n)$, for various (integer) values of n, illustrating that collisions occur at the origin only.

Since eigenvalues do not collide away from the origin they cannot leave the imaginary axis through such collisions and no high-frequency instabilities occur for small amplitude solutions of the gKdV equation. This result applies to the KdV and mKdV equations as special cases. The absence of high-frequency instabilities for small amplitude solutions is consistent with the results in, for instance, [9, 21, 22].

5.4.2 The Whitham equation

As our final scalar example, we consider the Whitham equation (5.4). For this example, no analytical results exist, but the work of Sanford *et al.* [76] allows for a comparison with numerical results. Sanford *et al.* do not report the presence of high-frequency instabilities for solutions of any period, and their absence has been verified by us using the same methods. Hur & Johnson [43] consider periodic solutions, focusing on the modulational instability. However, they do include a Krein signature calculation of the eigenvalues of the zero-amplitude solutions, reaching the same conclusions obtained below. In what follows the nonlinear term $N(u)$ will be ignored, as in the previous examples.

1. The modified Hamiltonian is $H_V^0 = \frac{V}{2}\int_0^{2\pi} u^2 dx - \frac{1}{2}\int_{-\pi}^{\pi}\int_{-\pi}^{\pi} K(x-y)u(x)u(y)dxdy$.

   We use V to denote the speed of the travelling wave, to avoid confusion with the phase speed $c(k)$ in the kernel of the Whitham equation.

2. The dispersion relation is given by (5.9).

3. The bifurcation branch starts at $(V, 0) = (\sqrt{g\tanh(h)}, 0)$, where we have chosen $N = 1$ so that the minimal period of the solutions is 2π.

4. The elements of the stability spectrum are given by

$$\lambda_n^{(\mu)} = i(n+\mu)\sqrt{g\tanh(h)} - i\text{sign}(n+\mu)\sqrt{g(n+\mu)\tanh(h(n+\mu))}. \tag{5.41}$$

5. The dispersion relation for the Whitham equation is plotted in Fig. 5.6(a), together with the line through the origin with slope $\omega(1)/1$. Since the dispersion relation is concave down (up) in the first (third) quadrant, no secant line of the dispersion relation through two points with abscissa that are integers apart exists that is parallel to the line through the origin, but does not coincide with it. Thus collisions of eigenvalues away from the origin do not occur. This is also illustrated in Fig. 5.6(b), where the imaginary part of $\lambda_n^{(\mu)}$ is plotted for various integers n.

6. No Krein signature calculation is relevant since eigenvalues do not collide away from the origin.

We have followed the methods in [76] in order to verify the theory. Using the cosine collocation method with 128 Fourier modes, we can compute solutions along the bifurcation branch. Choosing a relatively small amplitude solution shown on the left in Figure 5.7. Analyzing the spectral stability of that solution using the Fourier-Floquet-Hill method [23], we obtain the spectrum seen on the right of Figure 5.7, for which we used 2000 Floquet parameters. Only the presence of the Benjamin-Feir instability is seen and no high frequency instabilities as predicted.

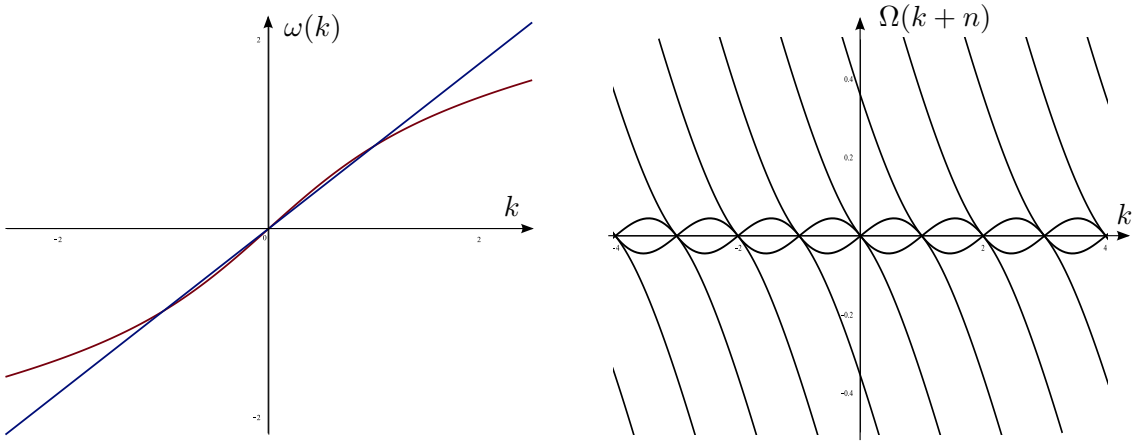

(a) (b)

Figure 5.6: (a) The dispersion relation for the Whitham equation. The line through the origin has slope $\omega(1)/1$, representing the right-hand side of (5.26). (b) The curves $\Omega(k+n)$, for various (integer) values of n, illustrating that collisions occur at the origin only.

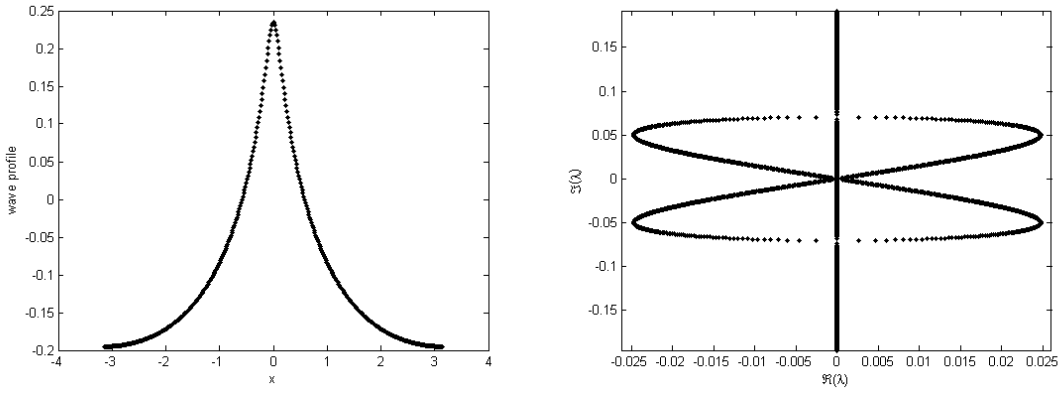

Figure 5.7: A small amplitude wave profile (left) and the corresponding complex eigenvalue plane (right) for the Whitham equation showing no presence of high frequency instabilities.

We conclude that periodic solutions of sufficiently small amplitude of the Whitham equation are not succeptible to high-frequency instabilities. This is consistent with the results presented in [76] and reproduced in Figure 5.7. Thus, the Whitham equation is unable to replicate the instabilities found in the shallow depth water wave problem for

solutions of small amplitude, despite having a dispersion relation that is identical to one branch of the water wave dispersion relation. We will return to this in the next section where a similar theory is developed for Hamiltonian PDEs with canonical Poisson structure, including the water wave problem [94].

5.5 Two-component Hamiltonian PDEs with canonical Poisson structure

We generalize the ideas of the previous section to the setting of two-component Hamiltonian PDEs with canonical Poisson structure. In other words, the evolution PDE can be written as

$$\frac{\partial}{\partial t}\begin{pmatrix} q \\ p \end{pmatrix} = J\nabla H \quad \Leftrightarrow \quad \begin{cases} q_t &= \dfrac{\delta H}{\delta p} \\ p_t &= -\dfrac{\delta H}{\delta q} \end{cases}, \tag{5.42}$$

where the Poisson operator J is given by

$$J = \begin{pmatrix} 0 & 1 \\ -1 & 0 \end{pmatrix}. \tag{5.43}$$

This Poisson operator is nonsingular, thus there are no Casimirs. Examples of systems of this form are the Nonlinear Schrödinger equation in real coordinates [10], the Sine-Gordon equation [33, 47, 48], and the water wave problem [94]. As before, our interest is in the linearization of this system around the zero-amplitude solution. The quadratic Hamiltonian corresponding to this linearization can be written as

$$H^0 = \int_0^{2\pi} \left(\frac{1}{2}\sum_{n=0}^{\infty} c_n q_{nx}^2 + \frac{1}{2}\sum_{n=0}^{\infty} b_n p_{nx}^2 + p\sum_{n=0}^{\infty} a_n q_{nx} \right) dx, \tag{5.44}$$

with A_n, B_n, $C_n \in \mathbb{R}$. Typically the number of terms in the sums above is finite, but an example like the water wave problem requires the possibility of an infinite number of nonzero contributing terms in the Hamiltonian. As for the Whitham equation, convergence of the resulting series is not problematic. The form (5.44) is the most general form of a quadratic Hamiltonian depending on two functions $q(x,t)$ and $p(x,t)$. Indeed, any quadratic

term of a form not included above is reduced to a term that is included by straightforward integration by parts. The linearization of (5.42) is given by

$$\begin{cases} q_t &= \sum_{n=0}^{\infty} a_n q_{nx} + \sum_{n=0}^{\infty} (-1)^n b_n p_{2nx}, \\ p_t &= -\sum_{n=0}^{\infty} (-1)^n c_n q_{2nx} - \sum_{n=0}^{\infty} (-1)^n a_n p_{nx}. \end{cases} \tag{5.45}$$

We proceed with the six step program outlined in the introduction.

1. **Quadratic Hamiltonian.** The modified Hamiltonian H_c^0 is given by

$$H_c^0 = \int_0^{2\pi} \left(cpq_x + \frac{1}{2} \sum_{n=0}^{\infty} c_n q_{nx}^2 + \frac{1}{2} \sum_{n=0}^{\infty} b_n p_{nx}^2 + p \sum_{n=0}^{\infty} a_n q_{nx} \right) dx. \tag{5.46}$$

   This expression serves as a repository for the coefficients which are needed in what follows.

2. **Dispersion relation.** We look for solutions to (5.45) of the form $q = \hat{q} \exp(ikx - i\omega t)$ and $p = \hat{p} \exp(ikx - i\omega t)$. Requiring the existence of non-trivial (*i.e.*, non-zero) solutions, we find that $\omega(k)$ is determined by

$$\det \begin{pmatrix} i\omega + \sum_{n=0}^{\infty} a_n (ik)^n & \sum_{n=0}^{\infty} b_n k^{2n} \\ -\sum_{n=0}^{\infty} c_n k^{2n} & i\omega - \sum_{n=0}^{\infty} a_n (-1)^n (ik)^n \end{pmatrix} = 0. \tag{5.47}$$

   This is a quadratic equation for $\omega(k)$ resulting in two branches of the dispersion relation, $\omega_1(k)$ and $\omega_2(k)$. Assuming that (5.45) is dispersive, $\omega_1(k)$ and $\omega_2(k)$ are real-valued for $k \in \mathbb{R}$. This is not easily translated in a condition on the coefficients a_n, b_n, c_n and d_n, since their reality is not assumed.

3. **Bifurcation branches.** Travelling wave solutions are stationary solutions of

$$\begin{cases} q_t &= cq_x + \sum_{n=0}^{\infty} a_n q_{nx} + \sum_{n=0}^{\infty} (-1)^n b_n p_{2nx} = \frac{\delta H_c^0}{\delta p}, \\ p_t &= cp_x - \sum_{n=0}^{\infty} (-1)^n c_n q_{2nx} - \sum_{n=0}^{\infty} (-1)^n a_n p_{nx} = -\frac{\delta H_c^0}{\delta q}. \end{cases} \tag{5.48}$$

This system has the dispersion relations $\Omega_{1,2}(k) = \omega_{1,2}(k) - ck$. In Fourier space the stationary equations become

$$\begin{cases} 0 &= ikc\hat{q} + \sum_{n=0}^{\infty} a_n (ik^n)\hat{q} + \sum_{n=0}^{\infty} (-1)^n b_n (ik)^{2n}\hat{p}, \\ 0 &= ikc\hat{p} - \sum_{n=0}^{\infty} (-1)^n c_n (ik)^{2n}\hat{q} - \sum_{n=0}^{\infty} (-1)^n a_n (ik)^n \hat{p}. \end{cases} \tag{5.49}$$

Thus c is obtained from the condition that these equations have a nontrivial solution $(\hat{q}, \hat{p})$. This condition requires that the 2×2 determinant of the system above is zero. A simple comparison with (5.47) gives that there are two bifurcation points given by $(\omega_1(N)/N, 0)$ and $(\omega_2(N)/N, 0)$. Any positive integer value of N is allowed, but we usually choose $N = 1$ so that the fundamental period is 2π. In what follows, we examine the small-amplitude solutions starting from the branch $(c, 0) = (\omega_1(N)/N, 0)$, without loss of generality.

4. **Stability spectrum.** To find the stability spectrum, we let $q = Q\exp(\lambda t)$, $p = P\exp(\lambda t)$. Using Floquet's Theorem,

$$Q = e^{i\mu x} \sum_{j=-\infty}^{\infty} Q_j e^{ijx}, \quad P = e^{i\mu x} \sum_{j=-\infty}^{\infty} P_j e^{ijx}, \tag{5.50}$$

with $\mu \in (-1/2, 1/2]$. Since (5.48) has constant coefficients, it suffices to consider monochromatic waves, *i.e.*, only one term of the sums in (5.50) is retained. It follows that λ satisfies (5.47) with $i\omega$ replaced by $-\lambda + i(n + \mu)c$. Thus

$$\lambda_{n,l}^{(\mu)} = i(n + \mu)c - i\omega_l(n + \mu) = -i\Omega_l(n + \mu), \qquad l = 1, 2. \tag{5.51}$$

As expected, the zero solution is neutrally stable, since $\omega_{1,2}(k)$ are real, assuming dispersive equations. The stability spectrum consists of two one-parameter point sets, one for $l = 1$ and the other for $l = 2$.

5. **Collision conditions.** Ignoring collisions at the origin, we require $\lambda^{(\mu)}_{n_1,l_1} = \lambda^{(\mu)}_{n_2,l_2} \neq 0$ for some $n_1, n_2 \in \mathbb{Z}$, $\mu \in (-1/2, 1/2]$, $l_1, l_2 \in \{1, 2\}$. This gives

$$\frac{\omega_{l_1}(n_1 + \mu) - \omega_{l_2}(n_2 + \mu)}{n_1 - n_2} = \frac{\omega_1(N)}{N}. \tag{5.52}$$

The right-hand side depends on ω_1 since we have chosen in Step 3. As before, this collision condition may be interpreted as a parallel secant condition, but with the additional freedom of being able to use points from both branches of the dispersion relation. This is illustrated in Fig. 5.8.

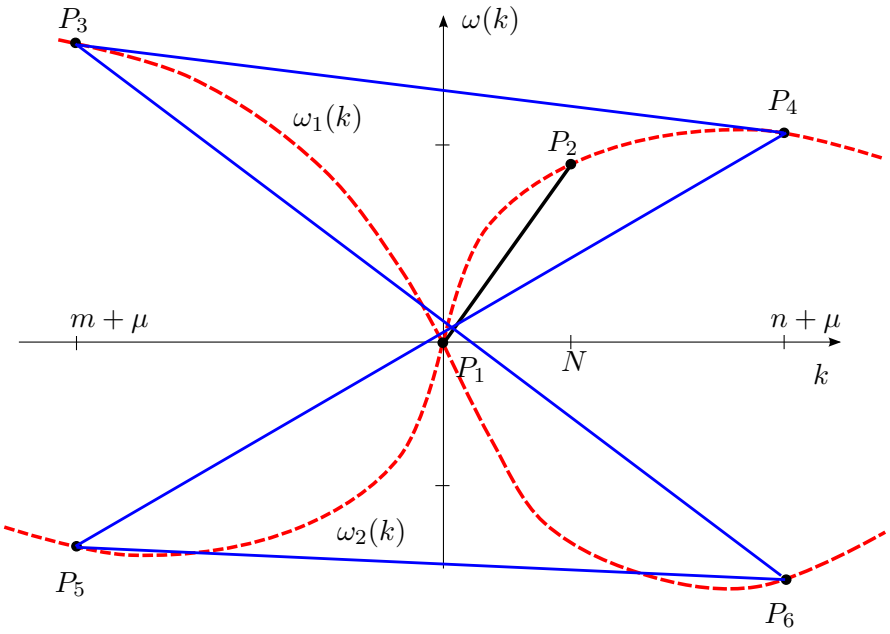

Figure 5.8: The graphical interpretation of the collision condition (5.52). The dashed curves are the graphs of the dispersion relations $\omega_1(k)$ and $\omega_2(k)$. The slope of the segment P_1P_2 is the right-hand side in (5.52). The collision condition (5.52) seeks points whose abscissas are an integer apart, so that at least one of the segments P_3P_4, P_3P_6, P_5P_4 or P_5P_6 is parallel to the segment P_1P_2.

6. **Krein signature.** In the setting of a system of Hamiltonian PDEs as opposed to a scalar PDE, we use a different but equivalent characterization of the Krein signature [61]. The Krein signature is the contribution to the Hamiltonian of the mode under consideration. Since our Hamiltonians are quadratic, this implies that the Krein signature of the eigenvalue λ with eigenvector v is given by

$$\text{signature}(\lambda, v) = \text{sign}(v^\dagger \mathcal{L}_c v), \tag{5.53}$$

where $\mathcal{L}_c$ is the Hessian of the Hamiltonian H_c^0, and $v^\dagger$ denotes the complex conjugate of the transposed vector. Since the Hessian $\mathcal{L}_c$ is a symmetric linear operator, the argument of the sign in (5.53) is real. Recall that the linearization of the system (5.3) can be written as

$$\partial_t \begin{pmatrix} q \\ p \end{pmatrix} = J\mathcal{L}_c \begin{pmatrix} q \\ p \end{pmatrix}, \tag{5.54}$$

which makes it easy to read off $\mathcal{L}_c$. For the case of (5.48),

$$\mathcal{L}_c = \begin{pmatrix} \sum_{n=0}^{\infty} c_n (-1)^n \partial_x^{2n} & -c\partial_x + \sum_{n=0}^{\infty} a_n (-1)^n \partial_x^n \\ c\partial_x + \sum_{n=0}^{\infty} a_n \partial_x^n & \sum_{n=0}^{\infty} b_n (-1)^n \partial_x^{2n} \end{pmatrix}. \tag{5.55}$$

Next, the eigenvectors v are given by

$$\begin{pmatrix} q \\ p \end{pmatrix} = e^{\lambda t + i\mu x + inx} \begin{pmatrix} Q_n \\ P_n \end{pmatrix}, \tag{5.56}$$

where $(Q_n, P_n)^T$ satisfies

$$\lambda \begin{pmatrix} Q_n \\ P_n \end{pmatrix} = J\hat{\mathcal{L}}_c \begin{pmatrix} Q_n \\ P_n \end{pmatrix}. \tag{5.57}$$

Here $\hat{\mathcal{L}}_c$ is the symbol of $\mathcal{L}_c$, *i.e.*, the 2×2 matrix obtained by replacing $\partial_x \to i(n+\mu)$ in (5.55):

$$\hat{\mathcal{L}}_c = \begin{pmatrix} \sum_{n=0}^{\infty} c_n(n+\mu)^{2n} & -ic(n+\mu) + \sum_{n=0}^{\infty} a_n(-1)^n(in+i\mu)^n \\ ic(n+\mu) + \sum_{n=0}^{\infty} a_n(in+i\mu)^n & \sum_{n=0}^{\infty} b_n(n+\mu)^{2n} \end{pmatrix}. \tag{5.58}$$

Using (5.57), (5.53) is rewritten as

$$\text{signature}\left(\lambda_{n,l}^{(\mu)}, v_{n,l}^{(\mu)}\right) = \text{sign}\left(\lambda_{n,l}^{(\mu)} \det\begin{pmatrix} Q_n & P_n \\ Q_n^* & P_n^* \end{pmatrix}\right). \tag{5.59}$$

The determinant is imaginary, since interchanging the rows gives the complex conjugate result. Since $\lambda_{n,l}^{(\mu)}$ is imaginary, the result is real and the signature is well defined. Again, it is clear that no conclusions can be drawn if $\lambda_{n,l}^{(\mu)} = 0$. Since we wish to examine whether signatures are equal or opposite, we consider the product of the signatures corresponding to $\lambda_{n_1,l_1}^{(\mu)}$ and $\lambda_{n_2,l_2}^{(\mu)}$. Using (5.58) we find that signatures are opposite, provided that

$$\sum_{j_1=0}^{\infty} c_{j_1}(n_1+\mu)^{2j_1} \sum_{j_2=0}^{\infty} c_{j_2}(n_2+\mu)^{2j_2} \left(\omega_{l_1}(n_1+\mu) + \sum_{j_3=0}^{\infty} a_{2j_3+1}(-1)^{j_3}(n_1+\mu)^{2j_3+1}\right) \times \left(\omega_{l_2}(n_2+\mu) + \sum_{j_4=0}^{\infty} a_{2j_4+1}(-1)^{j_4}(n_2+\mu)^{2j_4+1}\right) < 0. \tag{5.60}$$

The above condition is obtained by expressing the eigenvectors in (5.57) in terms of the entries of the first row of (5.58). An equivalent condition is obtained using the second row:

$$\sum_{j_1=0}^{\infty} b_{j_1}(n_1+\mu)^{2j_1} \sum_{j_2=0}^{\infty} b_{j_2}(n_2+\mu)^{2j_2} \left(\omega_{l_1}(n_1+\mu) - \sum_{j_3=0}^{\infty} a_{2j_3+1}(-1)^{j_3}(n_1+\mu)^{2j_3+1} \right) \times \left(\omega_{l_2}(n_2+\mu) - \sum_{j_4=0}^{\infty} a_{2j_4+1}(-1)^{j_4}(n_2+\mu)^{2j_4+1} \right) < 0. \tag{5.61}$$

Depending on the system at hand, the condition (5.60) or (5.61) may be more convenient to use.

Remark. An important class of systems is those for which $\omega_1(k) = -\omega_2(k)$. We refer to such systems as even systems. It follows immediately from (5.47) that for even systems $a_{2j+1} = 0$, $j = 1, 2, \ldots$. The Krein conditions (5.60) and (5.61) simplify significantly, becoming

$$\omega_{l_1}(n_1+\mu)\omega_{l_2}(n_2+\mu) \sum_{j_1=0}^{\infty} c_{j_1}(n_1+\mu)^{2j_1} \sum_{j_2=0}^{\infty} c_{j_2}(n_2+\mu)^{2j_2} < 0, \tag{5.62}$$

or

$$\omega_{l_1}(n_1+\mu)\omega_{l_2}(n_2+\mu) \sum_{j_1=0}^{\infty} b_{j_1}(n_1+\mu)^{2j_1} \sum_{j_2=0}^{\infty} b_{j_2}(n_2+\mu)^{2j_2} < 0. \tag{5.63}$$

We summarize our results.

Assume that the linearization of the Hamiltonian system (5.42) is dispersive (*i.e.,* its dispersion relations $\omega_1(k)$ and $\omega_2(k)$ are real valued for $k \in \mathbb{R}$). Let N be a strictly positive integer. Consider $2\pi/N$-periodic travelling wave solutions of this system of sufficiently small-amplitude and with velocity sufficiently close to $\omega_1(N)/N$. In order for these solutions to be spectrally unstable with respect to high-frequency instabilities as a consequence of two-eigenvalue collisions, it is necessary that there exist $l_1,\ l_2\ \in \{1,2\}$, $n_1,\ n_2\ \in \mathbb{Z}$, $n_1 \neq n_2$, $\mu \in (-1/2, 1/2]$ for which

$$\frac{\omega_{l_1}(n_1+\mu)}{n_1+\mu} \neq \frac{\omega_1(N)}{N}, \quad \frac{\omega_{l_2}(n_2+\mu)}{n_2+\mu} \neq \frac{\omega(N)}{N}, \tag{5.64}$$

such that

$$\frac{\omega_{l_1}(n_1+\mu)-\omega_{l_2}(n_2+\mu)}{n_1-n_2}=\frac{\omega_1(N)}{N}, \tag{5.65}$$

and (5.60), or equivalently, (5.61) holds.

We proceed with examples.

5.5.1 The Sine-Gordon equation

As a first example, we consider the Sine-Gordon (SG) equation [79]:

$$u_{tt}-u_{xx}+\sin u=0. \tag{5.66}$$

The stability of the periodic travelling wave solutions of this equation has been studied recently by Jones *et al.* [47, 48]. Different classes of periodic travelling wave solutions exist, but only two of those can be considered as small-amplitude perturbations of a constant background state. We consider the so-called superluminal ($c^2>1$) librational waves. The subluminal ($c^2<1$) librational waves require the use of the transformation $v=u-\pi$ so that their small amplitude limit approaches the zero solution. We do not consider them here. The limits of the rotational waves are either soliton solutions or have increasingly larger amplitude. As such the rotational waves do not fit in the framework of this paper. An overview of the properties of these solutions as well as illuminating phase-plane plots are found in [47]. In contrast to [47, 48], we fix the period of our solutions, as elsewhere in this paper. This makes a comparison of the results more complicated.

1. **Quadratic Hamiltonian.** With $q=u$, $p=u_t$,

$$H_c^0=\int_0^{2\pi}\left(cpq_x+\frac{1}{2}p^2+\frac{1}{2}q^2+\frac{1}{2}q_x^2\right)dx. \tag{5.67}$$

   Thus $b_0=1$, $c_0=1$, $c_1=1$ are the only non-zero coefficients.

2. **Dispersion relation.** Using (5.47),

$$\omega_{1,2} = \pm\sqrt{1+k^2}. \tag{5.68}$$

These expressions are real valued for $k \in \mathbb{R}$, thus the SG equation is dispersive, when linearized around the superluminal librational waves. Both branches of the dispersion relation are displayed in Fig. 5.9a.

3. **Bifurcation branches.** With $N = 1$, we obtain $c = \omega_1(1)/1 = \sqrt{2}$.

4. **Stability spectrum.** The stability spectrum is given by (5.51):

$$\lambda_{n,l}^{(\mu)} = -i\Omega_l(n+\mu) = i(n+\mu)\sqrt{2} \mp i\sqrt{1+(n+\mu)^2}, \tag{5.69}$$

with $l = 1$ ($l = 2$) corresponding to the $-$ ($+$) sign. Here $n \in \mathbb{Z}$, $\mu \in [-1/2, 1/2)$.

5. **Collision condition.** The collision condition (5.52) becomes

$$\frac{\omega(n_1+\mu) - \omega_2(n_2+\mu)}{n_1 - n_2} = \sqrt{2}. \tag{5.70}$$

We have chosen $\omega_{l_1} = \omega_1$ and $\omega_{l_2} = \omega_2$, since it is clear that the collision condition can only be satisfied if points from both dispersion relation branches are used. This is illustrated in Fig. 5.9a. In fact, many collisions occur, as is illustrated in Fig. 5.9b. One explicit solution is given by

$$n_1 = 3,\ n_2 = 0,\ \mu = \frac{\sqrt{10}-3}{2} \approx 0.081138830. \tag{5.71}$$

6. **Krein signature.** Since $\omega_2(k) = -\omega_1(k)$, we may use the conditions (5.62) or (5.63). Since only one $b_j \neq 0$, (5.63) is (slightly) simpler to use. We get that

$$\omega_1(n_1+\mu)\omega_2(n_2+\mu) < 0 \tag{5.72}$$

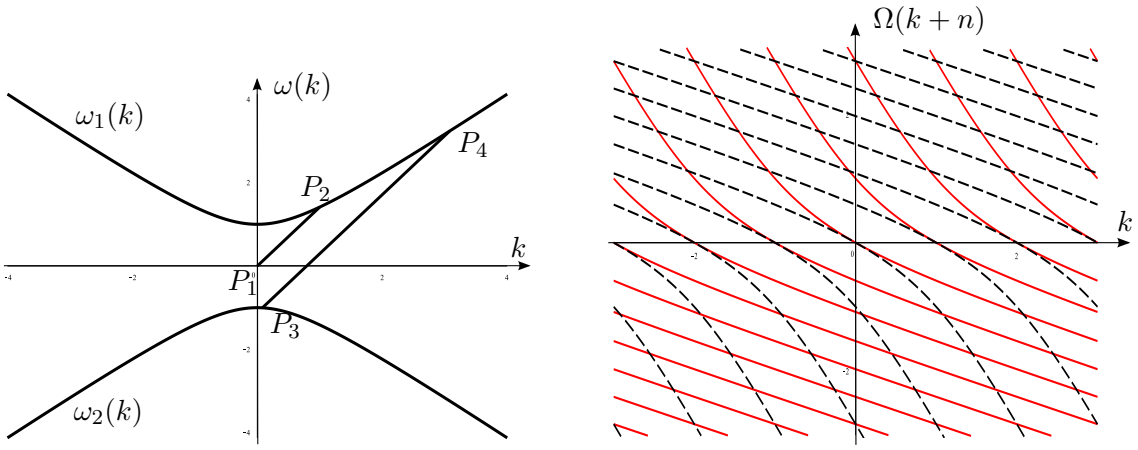

(a) (b)

Figure 5.9: (a) The two branches of the dispersion relation for the Sine-Gordon equation. The line segment P_1P_2 has slope $\omega(1)/1$, representing the right-hand side of (5.52). The slope of the parallel line segment P_3P_4 represents the left-hand side of (5.52). (b) The two families of curves $\Omega_1(k+n)$ (red, solid) and $\Omega_2(k+n)$ (black, dashed), for various (integer) values of n, illustrating that many collisions occur away from the origin.

is a necessary condition for the presence of high-frequency instabilities of small-amplitude superluminal librational solutions of the SG equation. The condition is trivially satisfied as it was remarked in the previous step that points from both dispersion relation branches have to be used to have collisions.

Now that we have the conclusion that there are eigenvalue collisions that may lead to instabilities, we can verify what happens numerically. Using elliptic functions, we can compute the solution to the Sine-Gordon equation analytically, making sure it is 2π periodic. This solutions is shown on the left of Figure 5.10. After analyzing the stability of that solution, the right inset of Figure 5.10, shows there are no high frequency instabilities, only the Benjamin-Feir instability. This is consistent with the analysis shown in [47] and [48].

5.5.2 The water wave problem

As a final example, we consider the water wave problem: the problem of determining the dynamics of the surface of an incompressible, irrotational fluid under the influence of grav-

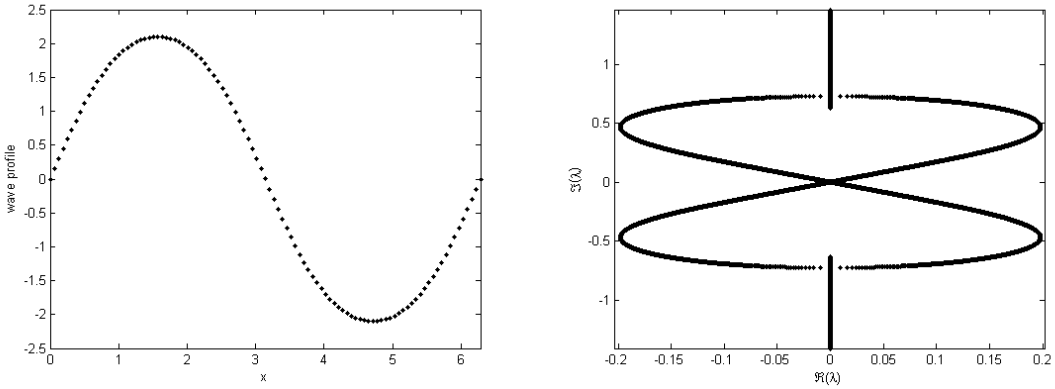

Figure 5.10: A small amplitude wave profile (left) and the corresponding complex eigenvalue plane (right) for the Sine-Gordon equation showing no presence of high frequency instabilities, despite the collision of eigenvalues of opposite Krein signature.

ity. For this example, the effects of surface tension are ignored and we consider only two-dimensional fluids, *i.e.*, the surface is one dimensional. The Euler equations governing the dynamics are

$$\phi_{xx} + \phi_{zz} = 0, \qquad (x,z) \in D, \tag{73a}$$

$$\phi_z = 0, \qquad z = -h, \tag{73b}$$

$$\eta_t + \eta_x \phi_x = \phi_z, \qquad z = \eta(x,t), \tag{73c}$$

$$\phi_t + \frac{1}{2}(\phi_x^2 + \phi_z) + g\eta = 0, \qquad z = \eta(x,t), \tag{73d}$$

where x and z are the horizontal and vertical coordinate, respectively; $z = \eta(x,t)$ is the free top boundary and $\phi(x,z,t)$ is the velocity potential. Further, g is the acceleration of gravity and h is the average depth of the fluid.

The main goal of the water wave problem is to understand the dynamics of the free surface $\eta(x,t)$. Thus it is convenient to recast the problem so as to involve only surface variables. Zakharov [94] showed that the water wave problem is Hamiltonian with canonical variables $\eta(x,t)$ and $\varphi(x,t) = \phi(x,\eta(x,t),t)$. In other words $\varphi(x,t)$ is the velocity potential evaluated at the surface. Following [17], the Hamiltonian is written as

$$H = \frac{1}{2}\int_0^{2\pi} \left(\varphi G(\eta)\varphi + g\eta^2\right) dx, \tag{74}$$

where $G(\eta)$ is the Dirichlet $\to$ Neumann operator: $G(\eta)\varphi = (1+\eta_x^2)^{1/2}\phi_n$, at $z = \eta(x,t)$. Here ϕ_n is the normal derivative of ϕ. Using the water wave problem, $G(\eta)\varphi = \phi_z - \eta_x\phi_x = \eta_t$, which is the first of Hamilton's equations: the water wave problem for $\eta(x,t)$ and $\varphi(x,t)$ is

$$\eta_t = \frac{\delta H}{\delta \varphi}, \quad \varphi_t = -\frac{\delta H}{\delta \eta}. \tag{75}$$

1. **Quadratic Hamiltonian.** Since for our purposes, only the linearization of (75) in a moving frame is required, it suffices to evaluate the Dirichlet $\to$ Neumann operator $G(\eta)$ at the flat surface $\eta = 0$, resulting in

$$G(0) = -i\partial_x \tanh(-ih\partial_x). \tag{76}$$

The quadratic Hamiltonian H_c^0 is given by

$$H_c^0 = c\int_0^{2\pi} \varphi\eta_x dx + \frac{1}{2}\int_0^{2\pi} \left(\varphi(-i\tanh(-ih\partial_x)\varphi_x + g\eta^2\right) dx, \tag{77}$$

giving rise to the linearized equations in a frame moving with velocity c:

$$\eta_t = \frac{\delta H_c^0}{\delta \varphi} = c\eta_x - i\tanh(-ih\partial_x)q_x, \tag{78a}$$

$$\varphi_t = -\frac{\delta H_c^0}{\delta \eta} = c\varphi_x + g\eta. \tag{78b}$$

2. **Dispersion relation.** The well-known dispersion relation [86] for the water wave problem is immediately recovered from the linearized system (78a-b) with $c = 0$ (so as to not be in a moving frame), resulting in

$$\omega^2 = gk\tanh(kh). \tag{79}$$

Note that the right-hand side of this expression is always positive. Thus there are two branches to the dispersion relation:

$$\omega_{1,2} = \pm \mathrm{sign}(k)\sqrt{gk\tanh(kh)}. \tag{80}$$

Thus ω_1 (ω_2) corresponds to positive (negative) phase speed, independent of the sign of k.

3. **Bifurcation branches.** Branches originate from $(c, \text{amplitude}) = (\omega_1(1)/1, 0)$ and $(c, \text{amplitude}) = (\omega_2(1)/1, 0)$. Without loss of generality, we focus on the first branch, for which the phase speed $\sqrt{g\tanh(h)}$ is positive. This allows for a straightforward comparison of our results with those for the Whitham equation, in Example 5.4.2.

4. **Stability spectrum.** The elements of the spectrum are given by

$$\begin{aligned}
\lambda_{n,1}^{(\mu)} &= -i\,\Omega_1(n+\mu) \\
&= i(n+\mu)\sqrt{g\tanh(h)} - i\,\mathrm{sign}(n+\mu)\sqrt{g(n+\mu)\tanh(h(n+\mu))}, \qquad (81a) \\
\lambda_{n,2}^{(\mu)} &= -i\,\Omega_2(n+\mu) \\
&= i(n+\mu)\sqrt{g\tanh(h)} + i\,\mathrm{sign}(n+\mu)\sqrt{g(n+\mu)\tanh(h(n+\mu))}. \qquad (81b)
\end{aligned}$$

The $\mathrm{sign}(n+\mu)$'s may be omitted in these expressions, as the same set of spectral elements is obtained.

5. **Collision condition.** The condition (5.52) is easily written out explicitly, but for our purposes it suffices to plot $\Omega_1(k+n)$ and $\Omega_2(k+n)$, for different values of n. This is done in Fig. 5.11b with $g = 1$ and $h = 1$. Although only the first collision is visible in the figure (all intersection points are horizontal integer shift of each other and correspond to the same value of μ and $\lambda_{n,j}^{(\mu)}$), it is clear from the curves shown

that many collisions occur. The figure is qualitatively the same for all finite values of depth.

All such collision points are potential origins of high-frequency instabilities, once it is established in the next step that their Krein signatures differ. It appears from the numerical results in [25] as well as previous chapters that the bubble of non-imaginary eigenvalues closest to the origin contains the high-frequency eigenvalues with the largest real part. Thus for waves in shallow water $kh < 1.363$ (no Benjamin-Feir instability) [6, 87, 96], these are the dominant instabilities. For waves in deep water ($kh > 1.363$) the Benjamin-Feir instability typically dominates, although there is a range of depth in deep water where the high-frequency instabilities have a larger growth rate, see [25]. The dependence on depth h of the location on the imaginary axis from which the high-frequency bubble closest to the origin bifurcates is shown in Fig. 5.11(c), with $g = 1$. As $h \to \infty$, the imaginary part of $\lambda \to 3/4$. This asymptote is drawn in Fig. 5.11(c) for reference. This figure demonstrates that for all positive values of the depth h, the instabilities considered are not modulational as they do not bifurcate away from the origin as the amplitude increases.

6. **Krein signature.** The conditions (5.62) and (5.63) become

$$\omega_{l_1}(n_1+\mu)\omega_{l_2}(n_2+\mu)g^2 < 0, \tag{82}$$

and

$$\omega_{l_1}(n_1+\mu)\omega_{l_2}(n_2+\mu)\sum_{j_1=1}^{\infty}\alpha_{j_1-1}h^{2j_1-1}(n_1+\mu)^{2j_1}\sum_{j_2=1}^{\infty}\alpha_{j_2-1}h^{2j_2-1}(n_2+\mu)^{2j_2} < 0, \tag{83}$$

respectively. Here the coefficients α_j are related to the Bernoulli numbers [27], as they are defined by the Taylor series

$$\tanh(z) = \sum_{j=0}^{\infty} a_j z^{2j+1}, \quad |z| < \pi/2. \tag{84}$$

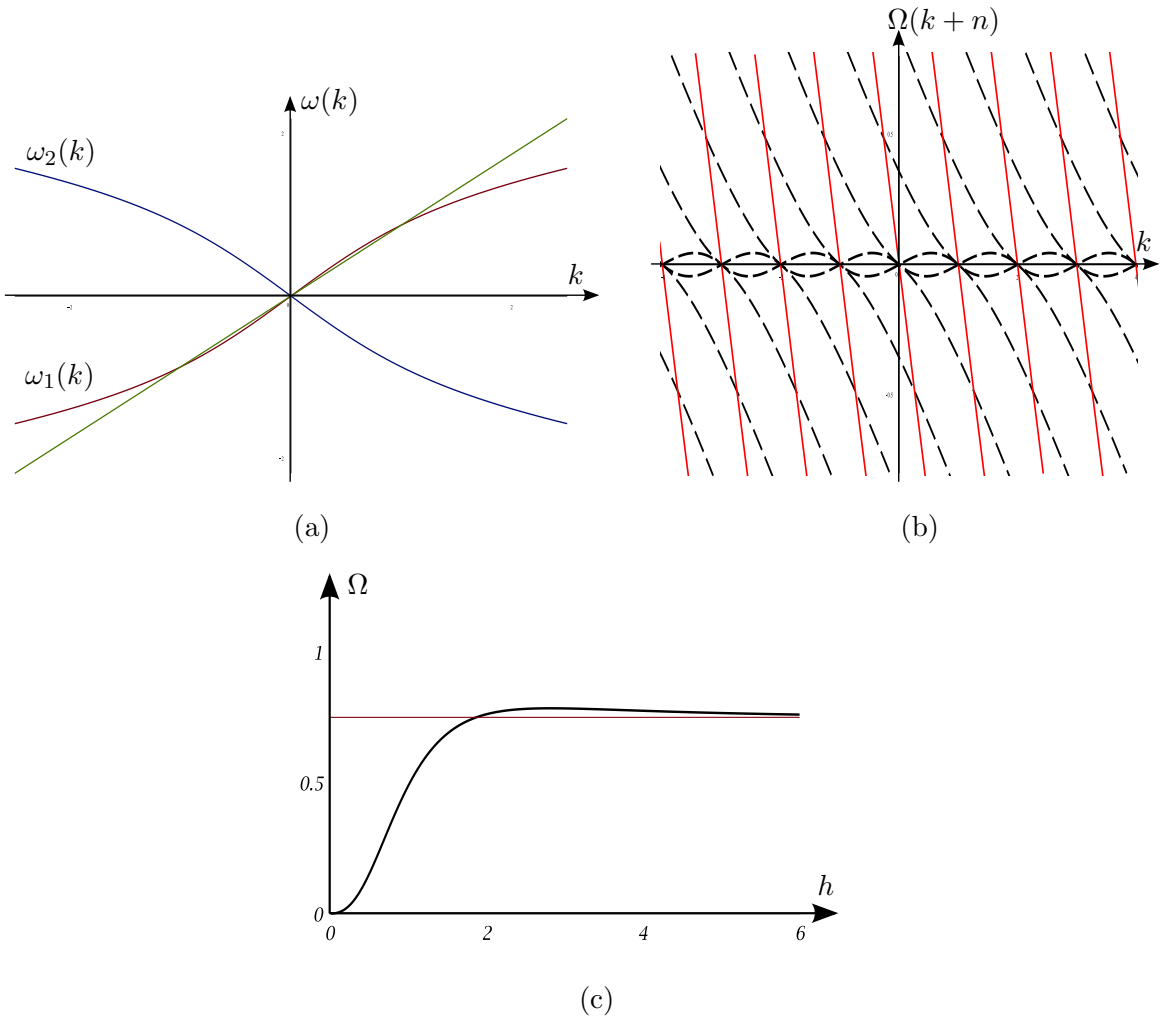

Figure 5.11: (a) The two branches of the dispersion relation for the water wave problem ($g = 1$, $h = 1$). The line through the origin has slope $\omega_1(1)/1$, representing the right-hand side of (5.52). (b) The two families of curves $\Omega_1(k + n)$ (red, solid) and $\Omega_2(k + n)$ (black, dashed), for various (integer) values of n, illustrating that many collisions occur away from the origin. (c) The origin of the high-frequency instability closest to the origin as a function of depth h.

Because of the finite radius of convergence of this series, (83) is only valid for small values of the wave numbers $n_1 + \mu$ and $n_2 + \mu$, but it is possible to phrase all results in terms of tanh directly, avoiding this difficulty. For instance, using (84), (83) may be rewritten as

$$\omega_{l_1}(n_1+\mu)\omega_{l_2}(n_2+\mu)\frac{\omega_\alpha^2(n_1+\mu)}{g}\frac{\omega_\beta^2(n_2+\mu)}{g}<0$$
$$\Rightarrow \qquad \omega_{l_1}(n_1+\mu)\omega_{l_2}(n_2+\mu)<0,$$

in agreement with (82). The indices α, $\beta \in \{0,1\}$ are irrelevant since ω_α and ω_β both appear squared. This serves to illustrate that for specific examples one of the two criteria (5.60) and (5.61) (or (5.62) and (5.63) for even systems) may be significantly easier to evaluate, although they are equivalent.

It was remarked in Example 5.4.2 that no collisions are possible due to the concavity of the dispersion relation. As a consequence, all collisions away from the origin observed in Fig. 5.11b involve both branches of the dispersion relation, *i.e.*, they involve a solid curve and a dashed curve. This is easily seen from Fig. 5.11a: a parallel cord with abscissae of the endpoints that are integers apart is easily found by sliding a parallel cord away from the cord $((0,0),(1,\omega_1(1)))$ until the integer condition is met. This implies that $\omega_{l_1}(n_1+\mu)$ and $\omega_{l_2}(n_2+\mu)$ in the collision condition (5.52) have opposite sign and (82) is always satisfied. Thus colliding eigenvalues of zero-amplitude water wave solutions *always* have opposite Krein signature. As a consequence, the necessary condition for the presence of high-frequency instabilities is met. In fact, it was observed in [25] that all colliding eigenvalues give rise to bubbles of instabilities as the amplitude was increased. In fact, a similar analysis also shows this is true for waves with surface tension. These results were presented in previous chapters.

Our general framework easily recovers the results of MacKay & Saffman [62]. There the set-up is for arbitrary amplitudes of the travelling wave solutions, but the results are only truly practical for the zero-amplitude case.

Remark. It follows from these considerations that the high-frequency instabilities present in the water wave problem are a consequence of counter-propagating waves as no such instabilities are present in the Whitham equation (5.4). Although it is often stated that the value of the Whitham equation lies in that it has the same dispersion relation as

the water wave problem (see for instance [89]), this is in fact not the case as it contains only one branch of the dispersion relation. Thus the equation does not allow for the interaction of counter-propagating modes, and as such misses out on much of the important dynamics of the Euler equations.

5.6 A Boussinesq-Whitham equation

The goal of this section is the introduction of a model equation that has the same dispersion relation as the Euler equations (73a-d) at the level of heuristics that led Whitham to the model equation (5.4). In other words, we propose a bidirectional Whitham equation, so as to capture both branches of the water wave dispersion relation. We refer to this equation as the Boussinesq-Whitham (BW) equation. It is given by

$$q_{tt} = \partial_x^2 \left(\alpha q^2 + \int_{-\infty}^{\infty} K(x-y) q(y) dy \right), \tag{85}$$

where

$$K(x) = \frac{1}{2\pi} \int_{-\infty}^{\infty} c^2(k) e^{ikx} dk, \tag{86}$$

and $c^2(k) = g \tanh(kh)/k$, $\alpha > 0$ for the water wave problem without surface tension. Since our methods focus on the analysis of zero amplitude solutions, the sign of α is not relevant in what follows. This equation is one of many that may stake its claim to the name "Boussinesq-Whitham equation". Equation (85) is a "Whithamized" version of the standard Bad Boussinesq equation and it may be anticipated that it captures at least the small-amplitude instabilities of the water wave problem in shallow water. It should be remarked that the Bad Boussinesq equation is ill posed as an initial-value problem [66], but it might be anticipated that the inclusion of the entire water-wave dispersion relation overcomes the unbounded growth that is present due to the polynomial truncation. We return to this at the end of this section.

Before applying our method to examine the potential presence of high-frequency instabilities of small-amplitude solutions of the BW equations, we need to present its Hamiltonian

structure. Further, since (85) is defined as an equation on the whole line, a periodic analogue is required, as in Section 5.2.

It is easily verified that (85) is Hamiltonian with Poisson operator [66]

$$J = \begin{pmatrix} 0 & \partial_x \\ \partial_x & 0 \end{pmatrix}, \tag{87}$$

and Hamiltonian

$$H = \int_{-\infty}^{\infty} \left(\frac{1}{2}p^2 + \frac{\alpha}{3}q^3 \right) dx + \frac{1}{2} \int_{-\infty}^{\infty} dx \int_{-\infty}^{\infty} dy\, K(x-y)q(x)q(y). \tag{88}$$

Indeed, (85) can be rewritten in the form (5.1) with $u = (q, p)^T$.

To define a periodic version of (85), let

$$K(x) = \frac{1}{L} \sum_{j=-\infty}^{\infty} c^2(k_j) e^{ik_j x}, \tag{89}$$

where $k_j = 2\pi j/L$, $j \in \mathbb{Z}$. The periodic BW equation is obtained from (5.1), using (87) and (88), but with all $\pm$ infinities in the integration bounds replaced by $\pm L/2$, respectively. Since (85) has a Poisson operator (87) that is different from those used in Sections 5.4 and 5.5, minor modifications to the use of the method are necessary.

1. **Quadratic Hamiltonian.** Ignoring the contributions of the nonlinear term, the quadratic Hamiltonian in a frame of reference moving with speed V is given by

$$H_V^0 = \int_0^{2\pi} \left(Vqp + \frac{1}{2}p^2 \right) dx + \frac{1}{2} \int_0^{2\pi} dx \int_0^{2\pi} dy\, K(x-y)q(x)q(y), \tag{90}$$

   where we have fixed the period of the solutions to be $L = 2\pi$. The inclusion of the first term in (90) is one place where the effect of the different form for J is felt, as its functional form is a direct consequence of the form of (87).

2. **Dispersion Relation.** A direct calculation confirms that

$$\omega^2 = gk \tanh(kh), \tag{91}$$

which is, by construction, identical to the dispersion relation for the full water wave problem, see (79). This gives rise to two branches of the dispersion relation (80), corresponding to right- and left-going waves.

3. **Bifurcation Branches.** Bifurcation branches for 2π-periodic solutions start at $(V_{1,2}, 0)$, where the phase speeds $V_{1,2}$ are given by $V_{1,2} = \pm\sqrt{g\tanh(k)}$.

4. **Stability Spectrum.** The stability spectrum elements are, again by construction, identical to those for the water wave problem, given in (81a-b).

5. **Collision Condition.** Given that the spectral elements are identical to those for the water wave problem, the collision condition is identical too. It is displayed in Fig. 5.11(a-b). Thus, collisions away from the origin occur. It remains to be seen whether these can result in the birth of high-frequency instabilities.

6. **Krein Signature.** As for the canonical case of Section 5.5, we use (5.53). Thus we calculate the Hessian $\mathcal{L}_c$ of the Hamiltonian H_c^0.

   Let

$$c^2(k) = \sum_{j=0}^{\infty} \gamma_j k^{2j}, \tag{92}$$

   where $\gamma_j = gh^{2j+1}a_j$, with the coefficients a_j defined in (84). A direct calculation gives that the Hamiltonian (90) is rewritten as

$$H_V^0 = \frac{1}{2}\int_0^{2\pi} \left(p^2 + Vqp + \sum_{j=0}^{\infty} \gamma_j q_{jx}^2 \right) dx. \tag{93}$$

   Using this form of the Hamiltonian, the calculation of the Hessian is straightforward, leading to

$$\mathcal{L}_V = \begin{pmatrix} \sum_{j=0}^{\infty} \gamma_j (-1)^j \partial_x^{2j} & V \\ V & 1 \end{pmatrix}. \tag{94}$$

Next, we compute the eigenvectors $v = (q, p)^T$. We have

$$\begin{pmatrix} q \\ p \end{pmatrix} = e^{i\lambda t} \begin{pmatrix} Q(x) \\ P(x) \end{pmatrix}, \tag{95}$$

where $(Q, P)^T$ satisfies

$$\lambda \begin{pmatrix} Q \\ P \end{pmatrix} = \begin{pmatrix} 0 & \partial_x \\ \partial_x & 0 \end{pmatrix} \mathcal{L}_V \begin{pmatrix} Q \\ P \end{pmatrix}. \tag{96}$$

This is a second place where the Poisson operator J plays a crucial role as it affects the form of $v = (q, p)^T$, and thus the expression for the signature. One easily verifies that

$$\begin{pmatrix} Q \\ P \end{pmatrix} = e^{i(n+\mu)x} \begin{pmatrix} i(n+\mu) \\ \lambda - i(n+\mu)V \end{pmatrix} \tag{97}$$

satisfies (96).

We need to evaluate the sign of

$$
\begin{aligned}
&\begin{pmatrix} Q \\ P \end{pmatrix}^{\dagger} \mathcal{L}_V \begin{pmatrix} Q \\ P \end{pmatrix} \\
&= e^{-i(n+\mu)x} \begin{pmatrix} -i(n+\mu) \\ -\lambda + i(n+\mu)V \end{pmatrix}^T \begin{pmatrix} \sum_{j=0}^{\infty} \gamma_j (-1)^j \partial_x^{2j} & V \\ V & 1 \end{pmatrix} \begin{pmatrix} i(n+\mu) \\ \lambda - i(n+\mu)V \end{pmatrix} e^{i(n+\mu)x} \\
&= \begin{pmatrix} -i(n+\mu) \\ -\lambda + i(n+\mu)V \end{pmatrix}^T \begin{pmatrix} \sum_{j=0}^{\infty} \gamma_j (n+\mu)^{2j} & V \\ V & 1 \end{pmatrix} \begin{pmatrix} i(n+\mu) \\ \lambda - i(n+\mu)V \end{pmatrix} \\
&= \begin{pmatrix} -i(n+\mu) \\ i\omega(n+\mu) \end{pmatrix}^T \begin{pmatrix} c^2(n+\mu) & V \\ V & 1 \end{pmatrix} \begin{pmatrix} i(n+\mu) \\ -i\omega(n+\mu) \end{pmatrix} \\
&= 2\omega(n+\mu)\left(\omega - (n+\mu)V\right). \qquad (98)
\end{aligned}
$$

Let the signature associated with the first eigenvalue be the sign of $2\omega_{j_1}(\omega_{j_1} - (n_1 + \mu)V)$, where ω_{j_1} is a function of $n_1 + \mu$. Similarly, for the second eigenvalue, the signature is the sign of $2\omega_{j_2}(\omega_{j_2} - (n_2 + \mu)V)$. Using the collision condition $\lambda^{(\mu)}_{n_1,j_1} = \lambda^{(\mu)}_{n_2,j_2}$, the product of these two expressions is

$$
\begin{aligned}
\text{Product} &= 4\omega_{j_1}\omega_{j_2}(\omega_{j_1} - (n_1+\mu)V)(\omega_{j_2} - (n_2+\mu)V) \\
&= 4\omega_{j_1}\omega_{j_2}(\omega_{j_2} - (n_2+\mu)V)^2,
\end{aligned}
$$

which is less than zero since collisions can only occur for eigenvalues associated with opposite branches of the dispersion relation, see Fig. 5.11b. It follows that, as in the water wave case, the signatures of colliding eigenvalues are always opposite, and the necessary condition for spectral instability is met. Thus, unlike the Whitham equation (5.4), the Boussinesq-Whitham model (85) does not exclude the presence of high-frequency instabilities of small-amplitude solutions.

We verify the result numerically by using the cosine collocation method as in [76], but with a modification for the BW equation, taking into account the second order time deriva-

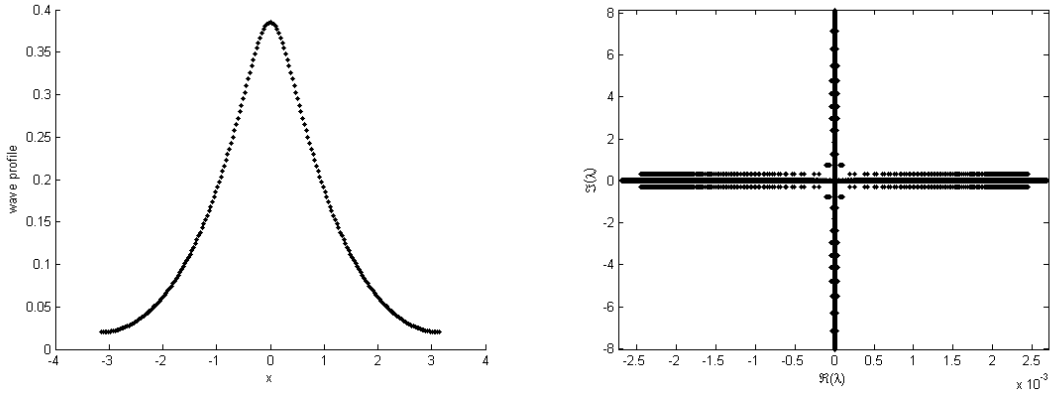

Figure 5.12: A small amplitude wave profile (left) and the corresponding complex eigenvalue plane (right) for the Boussinesq-Whitham equation showing a lot of high frequency instabilities.

tive. A small amplitude wave profile is seen on the left panel in Figure 5.12. In this wave profile, it is seen that the average wave amplitude is not zero. Numerically, it is difficult to compute a solution for the BW equation starting with a zero average solution, but there is a symmetry that can be applied to scale to a zero average solution. On the right panel in Figure 5.12, we have the plot of the complex eigenvalue plane, showing the Benjamin-Feir as well as high frequency instabilities.In order to refine these bubble instabilities, we used 2000 Floquet parameters. Figure 5.13 shows two different areas of the complex eigenvalue plane, mainly the largest instability due to Benjamin-Feir shown on the left, as well as the largest high frequency instability shown on the right. These numerical results confirm that the Boussinesq-Whitham equation is a model equation that does exhibit the presence of the instabilities also seen in the full water wave equations.

5.7 Conclusion

In this chapter, we showed how to extend the stability analysis to other Hamiltonian PDEs describing periodic systems. We presented a criteria for predicting for which small amplitude solutions in a moving frame of reference, can be unstable. This is determined by a 6 step process for both scalar and two-component Hamiltonian systems. This was illustrated by

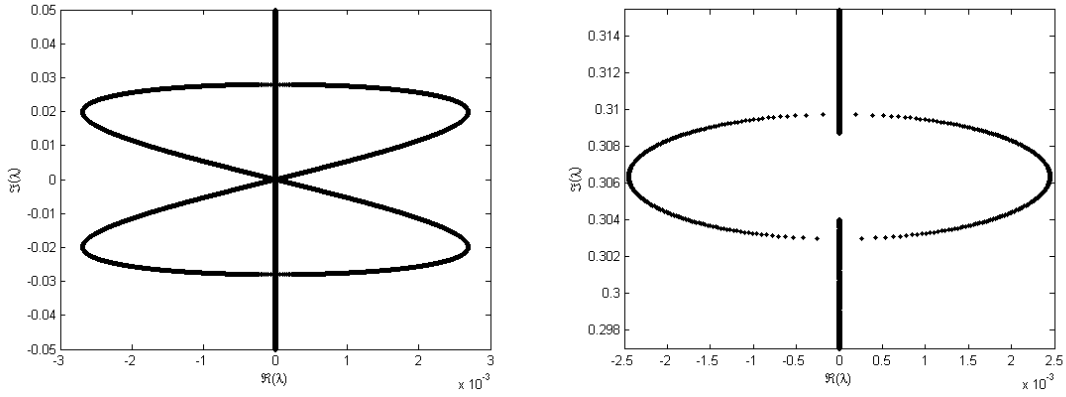

Figure 5.13: A zoom into the center region of the complex eigenvalue plane for the Boussinesq-Whitham equation (left) and a zoom into one of the bubbles representing the largest high frequency instability (right).

examining stability of the generalized KdV equation, the Whitham equation, Sine-Gordon and the water wave problem. Knowing that in the water wave model, we have high frequency instabilities as shown in [25] as well as the previous chapters, a model equation for water waves should include the presence of these instabilities. The Boussinesq-Whitham equation was shown to capture the high frequency instabilities, proving to be a more accurate model for water waves than the Whitham equation that did not include these instabilities.

Previously, we mentioned the possibility of a "Bad Boussinesq-Whitham" equation. When numerically solving for the BW equation, we are free to choose a conserved quantity such as the average of the solution. This quantity shows up when we compute the essential spectrum of the problem. This spectrum will grow to infinity unless we choose the average of the solution to be 0 such that the eigenvalues lie on the imaginary axis. This needs to be explored further. Mainly, it is hard to solve the zero average problem numerically. However, this is the solution we need to use for stability analysis. Currently, we introduce a shift to go between these two regimes. This shift takes advantage of the symmetries of the problem, but these have not been explored in great detail. More work has to be done to finalize the Boussinesq-Whitham example.

Chapter 6

CONCLUSION AND FUTURE WORK

The main goal of this thesis was to analyze the stability of solutions to Euler's equations in the presence of surface tension. In the first chapter, we started by reviewing existing results and describing how this work adds to this literature. It was seen that for pure gravity waves as in [25], there are instabilities in both deep and shallow water. In shallow water, these instabilities are due to high frequency perturbations and they are present even in deep water along with the Benjamin-Feir instability. At first, we showed what happens when we treat the addition of surface tension as a perturbation to the gravity wave case. We used the AFM formulation [1] to solve Euler's equations and the Fourier-Floquet-Hill method [23] to analyze the spectral stability of solutions. In Chapter 3, we saw that these instabilities are still present even with a small coefficient of surface tension. In Chapter 4, we increased the value of the coefficient of surface tension, which led to the presence of resonances. We used a boundary integral formulation to solve Euler's equations [91] to increase speed and accuracy of the computation. Once again, looking at the spectral stability of these solutions, we see the high frequency instabilities. In fact, there are more interesting instabilities for gravity-capillary waves. These are the double bubbles as well as the interesting patterns around the origin of the complex eigenvalue plane as seen in Chapter 4. In the last chapter of the thesis, we showed that using similar methods, we can analyze more than just Euler's equations. By looking at small amplitude solutions of Hamiltonian systems, we can follow a simple 6 step procedure to check if high frequency instabilities can occur. If the eigenvalues for the spectral stability problem collide for a particular Floquet parameter and these eigenvalues have opposite Krein signature, then the solution can become unstable as amplitude is increased. This is illustrated with several example equations including ones that are used to model water waves such as the Whitham equation. Since Euler's equations exhibit these types of instabilities, models for water waves should too. This is why we propose to use a modified Boussinesq-Whitham equation that exhibits these properties.

There are still a few questions that arise from our work that need further analysis.

- We want to analyze how the high frequency instabilities change as we vary wave amplitude. It can be seen from the numerical results that these instabilities may

decrease and the solution may become more stable at some wave amplitudes. However, examining their stability more carefully requires significant numerical accuracy and a large sample space of Floquet parameters. At the moment this is easy to implement, although time consuming.

- The numerical scheme for computing solutions has been set up, but it has not been pushed to its limits. An interesting question to answer is how high of an amplitude solution exists in the case of gravity-capillary waves? Do the resonant modes just oscillate with larger and larger amplitudes as we go up the bifurcation branch?

- We have only begun to examine the stability of waves where the surface tension is the dominant force. It would be interesting to compare and contrast the stability of waves where the trough gets shallower and the solutions resemble gravity waves as compared to those where the trough gets elongated and the solutions more resemble those for pure capillary waves.

- Interesting phenomena arise when we look near the origin of the complex eigenvalue plane of the stability spectra. We can track and analyze how some of these patterns arise.

- In looking at other Hamiltonian systems, we have come up with examples for where the Krein signature condition is either satisfied or not satisfied for the whole problem. However, there is a case where the Krein condition is only satisfied for some collisions and that is for the Kawahara equation. We have numerically analyzed this case, but saw that even in the case where the Krein condition was not satisfied, we still see instabilities numerically. Resolving this discrepancy remains ongoing work.

- Numerical computation of the stability for the Boussinesq-Whitham equation is still problematic. At the moment, we cannot compute solutions of zero average, however it is near those that we have to analyze stability. Otherwise, we can see growing modes in the essential spectrum. At the moment, we invoke the symmetries of the equations

to analyze the spectrum in the correct regime, but this statement needs to be more precise. We need to write down the exact regime for which the Boussinesq-Whitham equation is a good equation to use to model water waves.

BIBLIOGRAPHY

[1] M. J. Ablowitz, A.S. Fokas, and Z.H. Musslimani. On a new non-local formation of water waves. *J. Fluid Mech.*, 562:313–343, 2006.

[2] M. J Ablowitz and H. Segur. *Solitons and the inverse scattering transform*, volume 4. SIAM, 1981.

[3] B. Akers and D. P. Nicholls. Traveling waves in deep water with gravity and surface tension. *SIAM J. Appl. Math.*, 70:2373–2389, 2010.

[4] V. I. Arnol'd. *Mathematical methods of classical mechanics*, volume 60 of *Graduate Texts in Mathematics*. Springer-Verlag, New York, 1992. Translated from the 1974 Russian original by K. Vogtmann and A. Weinstein, Corrected reprint of the second (1989) edition.

[5] G. K. Batchelor. *An introduction to fluid dynamics*. Cambridge Mathematical Library. Cambridge University Press, Cambridge, paperback edition, 1999.

[6] T. B. Benjamin. Instability of periodic wavetrains in nonlinear dispersive systems. *Proc. Roy. Soc. (London) Ser. A*, 299:59–76, 1967.

[7] T. Brooke Benjamin and J. E. Feir. The disintegration of wave trains on deep water. *J. Fluid Mech.*, 27:417–430, 1967.

[8] H. Bohr. *Almost Periodic Functions*. Chelsea Publishing Company, New York, N.Y., 1947.

[9] N. Bottman and B. Deconinck. KdV cnoidal waves are spectrally stable. *Discrete Contin. Dyn. Syst.*, 25:1163–1180, 2009.

[10] N. Bottman, B. Deconinck, and M. Nivala. Elliptic solutions of the defocusing nls equation are stable. *J. Phys. A*, 44:285201, 2011.

[11] J. C. Bronski and M. A. Johnson. The modulational instability for a generalized Korteweg-de Vries equation. *Arch. Ration. Mech. Anal.*, 197(2):357–400, 2010.

[12] J. C. Bronski, M. A. Johnson, and T. Kapitula. An index theorem for the stability of periodic travelling waves of Korteweg-de Vries type. *Proc. Roy. Soc. Edinburgh Sect. A*, 141(6):1141–1173, 2011.

[13] O.P. Bruno and F. Reitich. Solution of a boundary value problem for the Helmholtz equation via variation of the boundary into the complex domain. *Proc. Royal Soc. Edinburgh*, 122A:317–340, 1992.

[14] D. C. Calvo, T.-S. Yang, and T. R. Akylas. On the stability of solitary waves with decaying oscillatory tails. *R. Soc. Lond. Proc. Ser. A Math. Phys. Eng. Sci.*, 456(1995):469–487, 2000.

[15] E. A. Coddington and N. Levinson. *Theory of ordinary differential equations*. McGraw-Hill Book Company, Inc., New York-Toronto-London, 1955.

[16] A. Constantin and W. Strauss. Pressure beneath a Stokes wave. *Comm. Pure Appl. Math.*, 63:533–557, 2010.

[17] W. Craig and C. Sulem. Numerical simulation of gravity waves. *J. Comput. Phys.*, 108:73–83, 1993.

[18] A. D. D. Craik. The origins of water wave theory. *Annu. Rev. Fluid Mech.*, 36:1–28, 2004.

[19] G. D. Crapper. An exact solution for progressive capillary waves of arbitrary amplitude. *J. Fluid Mech.*, 2:532–540, 1957.

[20] C. W. Curtis and B. Deconinck. On the convergence of Hill's method. *Maths. of Computation*, 79:169–187, 2010.

[21] B. Deconinck and T. Kapitula. The orbital stability of the cnoidal waves of the Korteweg-de Vries equation. *Phys. Lett. A*, 374(39):4018–4022, 2010.

[22] B. Deconinck and T. Kapitula. On the orbital (in)stability of spatially periodic stationary solutions of generalized Korteweg-de Vries equations. *Submitted for Publication*, pages 1–24, 2013.

[23] B. Deconinck and J. N. Kutz. Computing spectra of linear operators using the Floquet-Fourier-Hill method. *Journal of Comp. Physics*, 219:296–321, 2006.

[24] B. Deconinck and M. Nivala. The stability analysis of the periodic traveling wave solutions of the mKdV equation. *Stud. Appl. Math.*, 126(1):17–48, 2011.

[25] B. Deconinck and K. Oliveras. The instability of periodic surface gravity waves. *J. Fluid Mech.*, 675:141–167, 2011.

[26] B. Deconinck and O. Trichtchenko. Stability of periodic gravity waves in the presence of surface tension. *Eur. J. Mech. B Fluids*, 46, 2014.

[27] NIST Digital Library of Mathematical Functions. http://dlmf.nist.gov/, Release 1.0.8 of 2014-04-25. Online companion to [73].

[28] E.J. Doedel, R.C. Paffenroth, A.R. Champneys, T.F. Fairgrieve, Yu.A. Kuznetsov, B. Sandstede, and X. Wang. AUTO 2000: Continuation and bifurcation software for ordinary differential equations (with HomCont), 2001. http://indy.cs.concordia.ca/auto/.

[29] A.I. Dyachenko, E.A. Kuznetsov, M.D. Spector, and V.E. Zakharov. Analytical description of the free surface dynamics of an ideal fluid (canonical formalism and conformal mapping). *Phys. Letters A*, 221:73–79, 1996.

[30] *Dynamical systems. IV*, volume 4 of *Encyclopaedia of Mathematical Sciences*. Springer-Verlag, Berlin, 1990.

[31] M. Ehrnström, M. D. Groves, and E. Wahlén. On the existence and stability of solitary-wave solutions to a class of evolution equations of Whitham type. *Nonlinearity*, 25:2903–2936, 2012.

[32] M. Ehrnström and H. Kalisch. Traveling waves for the Whitham equation. *Differential and Integral Equations*, 22:1193–1210, 2009.

[33] L. D. Faddeev and L. A. Takhtajan. *Hamiltonian methods in the theory of solitons*. Classics in Mathematics. Springer, Berlin, english edition, 2007.

[34] M. Francius and C. Kharif. Three-dimensional instabilities of periodic gravity waves in shallow water. *J. Fluid Mech.*, 561:417–437, 2006.

[35] C.S. Gardner. The Korteweg-deVries equation and generalizations. IV the Korteweg-deVries equation as a Hamiltonian system. *J. Math. Phys.*, 12:1548–1551, 1971.

[36] W. Govaerts and Y. A. Kuznetsov. MatCont, 2007. http://matcont.sourceforge.net/.

[37] J. L. Hammack and D. M. Henderson. Resonant interactions among surface water waves. *Annual review of fluid mechanics*, 25:55–97, 1993.

[38] M. Hărăguş and T. Kapitula. On the spectra of periodic waves for infinite-dimensional Hamiltonian systems. *Phys. D*, 237(20):2649–2671, 2008.

[39] S. E. Haupt and J. P. Boyd. Modeling nonlinear resonance: a modification to the Stokes' perturbation expansion. *Wave Motion*, 10(1):83–98, 1988.

[40] D. M. Henderson and J. L. Hammack. Experiments on ripple instabilities. part 1. resonant triads. *J. Fluid Mech*, 184:15–41, 1987.

[41] P. D. Hislop and I. M. Sigal. *Introduction to spectral theory*, volume 113 of *Applied Mathematical Sciences*. Springer-Verlag, New York, 1996. With applications to Schrödinger operators.

[42] J.K. Hunter and J.-M. Vanden-Broeck. Solitary and periodic gravitycapillary waves of finite amplitude. *Journal of Fluid Mechanics*, 134:205–219, 1983.

[43] V. M. Hur and M. Johnson. Modulational instability in the Whitham equation of water waves. *Submitted for publication*, 2013.

[44] E. L. Ince. *Ordinary Differential Equations*. Dover Publications, New York, 1944.

[45] M. A. Johnson and K. Zumbrun. Convergence of Hill's method for nonselfadjoint operators. *SIAM J. Numer. Anal.*, 50(1):64–78, 2012.

[46] M. A. Johnson, K. Zumbrun, and J. C. Bronski. On the modulation equations and stability of periodic generalized Korteweg-de Vries waves via Bloch decompositions. *Phys. D*, 239(23-24):2057–2065, 2010.

[47] C. K. R. T. Jones, R. Marangell, P. D. Miller, and R. G. Plaza. On the stability analysis of periodic sine-Gordon traveling waves. *Phys. D*, 251:63–74, 2013.

[48] C. K. R. T. Jones, R. Marangell, P. D. Miller, and R. G. Plaza. Spectral and modulational stability of periodic wavetrains for the nonlinear klein-gordon equation. *arXiv:1312.1132 [math.AP]*, pages 1–62, 2014.

[49] M.C.W. Jones. Nonlinear stability of resonant capillary-gravity waves. *Wave Motion*, 15:267–283, 1992.

[50] M.C.W. Jones. Evolution equations and stability results for finite-depth Wilton ripples. *International Journal of Non-Linear Mechanics*, 31:41–57, 1996.

[51] T. Kapitula and K. Promislow. *Spectral and dynamical stability of nonlinear waves*, volume 185 of *Applied Mathematical Sciences*. Springer, New York, 2013.

[52] B. Kim and T. R. Akylas. Transverse instability of gravity-capillary solitary waves. *J. Engrg. Math.*, 58(1-4):167–175, 2007.

[53] R. Kollar and P. D. Miller. Graphical krein signature theory and evans-krein functions. 56:73–123, 2014.

[54] M. G. Kreĭn. A generalization of some investigations of A. M. Lyapunov on linear differential equations with periodic coefficients. *Doklady Akad. Nauk SSSR (N.S.)*, 73:445–448, 1950.

[55] M. G. Kreĭn. On the application of an algebraic proposition in the theory of matrices of monodromy. *Uspehi Matem. Nauk (N.S.)*, 6(1(41)):171–177, 1951.

[56] H. Lamb. *Hydrodynamics*. Dover.

[57] T. Levi-Civita. Détermination rigoreuse des ondes permanentes d'ampleur finie. *Math. Ann.*, 93:264, 1925.

[58] X. Liu and J. Duncan. The effects of surfactants on spilling breaking waves. *Nature*, 421:520–523, 2003.

[59] M. S. Longuet-Higgins. Capillary-gravity waves of solitary type and envelope solitons on deep water. *J. Fluid Mech.*, 252:703–711, 1993.

[60] M. S. Longuet-Higgins and E. D. Cokelet. The deformation of steep surface waves on water. I. A numerical method of computation. *Proc. Roy. Soc. London Ser. A*, 350:1–26, 1976.

[61] R. S. MacKay. Stability of equilibria of Hamiltonian systems. In *Nonlinear phenomena and chaos (Malvern, 1985)*, Malvern Phys. Ser., pages 254–270. Hilger, Bristol, 1986.

[62] R. S. MacKay and P.G. Saffman. Stability of water waves. *Proc. R. Soc. London A*, 406:115–125, 1986.

[63] L. F. McGoldrick. An experiment on second-order capillary gravity resonant wave interactions. *Journal of Fluid Mechanics*, 40:251–271, 1970.

[64] L. F. McGoldrick. On Wilton's ripples: a special case of resonant interactions. *Journal of Fluid Mechanics*, 42:193–200, 1970.

[65] L. F. McGoldrick. On the rippling of small waves: a harmonic nonlinear nearly resonant interaction. *Journal of Fluid Mechanics*, 52:725–751, 1971.

[66] H. P. McKean. Boussinesq's equation on the circle. *Comm. Pure Appl. Math.*, 34:599–691, 1981.

[67] J. W McLean. Instabilities of finite-amplitude gravity waves on water of finite depth. *Journal of Fluid Mechanics*, 114:331–341, 1982.

[68] J. W. McLean. Instabilities of finite-amplitude water waves. *J. Fluid Mech.*, 114:315–330, 1982.

[69] J. D. Meiss. *Differential dynamical systems*, volume 14 of *Mathematical Modeling and Computation*. Society for Industrial and Applied Mathematics (SIAM), Philadelphia, PA, 2007.

[70] P. A. Milewski, J.-M. Vanden-Broeck, and Z. Wang. Dynamics of steep two-dimensional gravity–capillary solitary waves. *J. Fluid Mech.*, 664:466–477, 2010.

[71] A. I. Nekrasov. *Točnaya teoriya voln ustanovivšegocya vida na poverhnosti tyaželoĭ židkosti*. Izdat. Akad. Nauk SSSR, Moscow, 1951.

[72] K. Oliveras. *Stability of periodic surface gravity water waves*. PhD thesis, University of Washington, Seattle, USA, 2009.

[73] F. W. J. Olver, D. W. Lozier, R. F. Boisvert, and C. W. Clark, editors. *NIST Handbook of Mathematical Functions*. Cambridge University Press, New York, NY, 2010. Print companion to [27].

[74] E. I. Părău, J.-M. Vanden-Broeck, and M. J. Cooker. Nonlinear three-dimensional gravity-capillary solitary waves. *J. Fluid Mech.*, 536:99–105, 2005.

[75] J. S. Russell. *The wave of translation in the oceans of water, air, and ether*. Trübner & Co., 1885.

[76] N. Sanford, K. Kodama, J. D. Carter, and H. Kalisch. Stability of traveling wave solutions to the Whitham equation. *Submitted for publication*, pages 1–11, 2013.

[77] A.H. Schooley. Double, triple, and higher-order dimples in the profiles of wind-generated water waves in the capillary-gravity transition region. *Journal of Geophysical Research*, 65:4075–4079, 1960.

[78] L. W. Schwartz and J.-M. Vanden-Broeck. Numerical solution of the exact equations for capillary–gravity waves. *Journal of Fluid Mechanics*, 95(01):119–139, 1979.

[79] A. C. Scott. A nonlinear klein-gordon equation. *Amer. J. Phys.*, 37:52–61, 1969.

[80] I. Stakgold. *Boundary value problems of mathematical physics. Vol. I, II*, volume 29 of *Classics in Applied Mathematics*. Society for Industrial and Applied Mathematics (SIAM), Philadelphia, PA, 2000.

[81] G. G. Stokes. On the theory of oscillatory waves. *Mathematical and Physical Papers*, 1:197–229, 1847.

[82] G. G. Stokes et al. *Mathematical and physical papers*, volume 1-5.

[83] D. J. Struik. Détermination rigoreuse des ondes irrotationnelles périodiques dans un canal à profondeur finie. *Math. Ann.*, 95:595, 1926.

[84] R. Tiron and W. Choi. Linear stability of finite-amplitude capillary waves on water of infinite depth. *J. Fluid Mech.*, 696:402–422, 2012.

[85] J-C van der Meer. *The Hamiltonian Hopf bifurcation*, volume 1160 of *Lecture Notes in Mathematics*. Springer-Verlag, Berlin, 1985.

[86] J.-M. Vanden-Broeck. *Gravity-Capillary Free-Surface Flows*. Cambridge University Press, Cambridge, 2010.

[87] G. B. Whitham. Non-linear dispersion of water waves. *J. Fluid Mech.*, 27:399–412, 1967.

[88] G. B. Whitham. Variational methods and applications to water waves. In *Hyperbolic equations and waves (Rencontres, Battelle Res. Inst., Seattle, Wash., 1968)*, pages 153–172. Springer, Berlin, 1970.

[89] G. B. Whitham. *Linear and nonlinear waves*. Wiley-Interscience, New York, NY, 1974. Pure and Applied Mathematics.

[90] J. Wilkening and V. Vasan. Comparison of five methods of computing the Dirichlet-Neumann operator for the water wave problem. *submitted for publication*, 2014.

[91] J. Wilkening and J. Yu. Overdetermined shooting methods for computing standing water waves with spectral accuracy. *Computational Science & Discovery*, 5(1):014017, 2012.

[92] J.R. Wilton. On ripples. *Philosophical Magazine Series 6*, 29(173):688–700, 1915.

[93] J. Wu. Laboratory studies of wind-wave interactions. *Journal of Fluid Mechanics*, 34:91–111, 1968.

[94] V. E. Zakharov. Stability of periodic waves of finite amplitude on the surface of a deep fluid. *J. Appl. Mech. Tech. Phys.*, 9:190–194, 1968.

[95] V. E. Zakharov and L. D. Faddeev. Korteweg - de Vries equation, a completely integrable hamiltonian system. *Funct. Anal. Appl.*, 5:280–287, 1971.

[96] V. E. Zakharov and L. A. Ostrovsky. Modulation instability: the beginning. *Phys. D*, 238(5):540–548, 2009.